OPTIMIZATION OF THE CLEANING SYSTEM OF GRAPE HARVESTERS USING THE DISCRETE-ELEMENT METHOD

A Thesis Submitted to the College of Graduate Studies and Research
in Partial Fulfillment of the Requirements for the Degree of
Master of Science
in the Department of Chemical and Biological Engineering
University of Saskatchewan
Saskatoon

By

Samuel Emard-Ferré

PERMISSION TO USE

In presenting this thesis in partial fulfilment of the requirements for a Postgraduate degree from the University of Saskatchewan, I agree that the Libraries of this University may make it freely available for inspection. I further agree that permission for copying of this thesis in any manner, in whole or in part, for scholarly purposes may be granted by the professor or professors who supervised my thesis work or, in their absence, by the Head of the Department or the Dean of the College in which my thesis work was done. It is understood that any copying or publication or use of this thesis or parts thereof for financial gain shall not be allowed without my written permission. It is also understood that due recognition shall be given to me and to the University of Saskatchewan in any scholarly use which may be made of any material in my thesis.

Requests for permission to copy or to make other use of material in this thesis in whole or part should be addressed to:

Head of the Department of Chemical and Biological Engineering
University of Saskatchewan
57 Campus Drive
Saskatoon, Saskatchewan, S7N 5A9

ABSTRACT

Grape harvesters are mechanized machines designed to remove grapes from vine trees, process them in a cleaning system, and then store them in onboard bins. These bins are later unloaded into a transport wagon and taken to a vinification facility. Cleaning systems can sometimes fail to completely remove the foreign materials (i.e. leaves, petioles, stems, etc.), which may compromise the vinification process. For this reason, the project focused on the cleaning system by minimizing the presence of foreign materials while maintaining an adequate harvesting throughput.

The project main objective was to optimize the cleaning system in grape harvesters by using the Discrete-Element Method (DEM). Individual DEM simulations were validated and used to develop a main crop flow simulation for the optimization of the cleaning system. This optimization included reducing the presence of foreign materials (petioles and leaves) while increasing the crop throughput for the specific grape variety of Cabernet Sauvignon. The physical characteristics and properties of the biological materials (grapes, petioles, leaves) were measured during the 2014 grape harvesting season at three different locations (Aigues-Mortes, Saint-Gervais, and Pauillac) in France. Time constraints limited the number of measured properties at the locations. The results from each location were compared using an ANOVA and a Tukey HSD post-hoc test. Given the natural variability of the biological materials, the three populations were found to be significantly different in most cases. The physical characteristics and properties from the Aigues-Mortes and Pauillac locations were used for the validation process. This was done because these locations had the most complete data sets. During the summer of 2015, a second testing phase took place to validate both the DEM leaf deflection and

cleaning system models. The additional experiments consisted of testing the leaf samples in controlled deflections and testing the efficiency of the cleaning system. These experiments used Cabernet Sauvignon leaves shipped from the Vineland Research and Innovation Centre (VRIC) in Ontario.

The individual simulations included the inclined plane, rebound surface, leaf deflection, and grape trajectory tests on an inclined conveyor. The inclined plane and rebound simulations were adjusted until the results were within 5% of the experimental test results. The leaf deflection simulations used optimized crop material properties until the simulated leaf behavior matched the actual leaf. Some discrepancies in the DEM simulated leaf shape were identified due to the limitations of the particle creation method. The grape trajectory test results coincided with the DEM simulations at greater conveyor speeds. A moderate difference between the simulations and the experimental tests was present at lower conveyor speeds. A possible cause for this difference may have been the effect of gravity and belt friction on the generation and acceleration of the grapes on the conveyor. A main crop flow simulation that included a conveyor and aspirator was developed using the previously validated simulations. Nine conveyor configurations, which included three belt angles from horizontal (10°, 15°, and 20°) and three speeds (350 rev/min (1.4 m/s), 420 rev/min (1.7 m/s), and 500 rev/min (2.0 m/s)), were tested to optimize the cleaning system performance. Based on the DEM simulations, the 420 rev/min-20° configuration was recommended as the optimal crop conveyor setting. This particular configuration minimized product damage and had an increased aspiration success rate of 9.6% compared to the conventional conveyor settings (420 rev/min-15°).

ACKNOWLEDGMENTS

This project would not have been possible without the help of numerous individuals. Their support, guidance, and expertise were essential in the completion of this project and I would like to recognize them.

I would like to acknowledge CNH Industrial for their continued support throughout the entire project. Special thanks to the entire crop flow simulation team (Canada, United States, and Belgium) for their endless support. Access to the CNH Industrial facilities and resources was much appreciated during testing preparations. In particular, I would like to thank the research and development shop employees in Saskatoon for helping me with the fabrication of several test stands.

Je remercie également l'équipe CNH Industriel à Coëx pour leurs contributions au projet. L'accueil chaleureux en France fut très apprécié. Je souligne la contribution des employées de l'atelier lors des montages de plusieurs bancs d'essais. Je souligne aussi la contribution généreuse de Vincent Rico et Daniel Le Nevé au cours du projet. Un grand merci également à Jordan Boissinot pour son aide avec les tests de feuilles.

My sincere gratitude to the University of Saskatchewan, the College of Engineering, and the Department of Chemical and Biological Engineering for their support throughout my entire university career. The dedication and efforts of countless professors have allowed me to develop useful skills and become very passionate about the field of engineering.

I would like to thank my two co-supervisors, Dr. Venkatesh Meda and Dr. Martin Roberge. Acknowledgements are also extended to my committee members: Dr. Oon-Doo Baik, Dr. Lope Tabil, and Dr. Akindele Odeshi. The support and guidance from my supervisors and committee members was essential throughout the many stages of the project. Un grand merci en particulier à Dr. Martin Roberge pour sa contribution et son aide tout au long du projet. Ce fut un plaisir de travailler ensemble.

Et finalement, j'aimerais remercier ma famille et mes amis qui mon enduré et supporté pendant plusieurs années éprouvantes à l'université. Merci à mes parents pour leur confiance et leur amour inconditionnel pendant mon parcours académique. Merci à Jean-Michel et Sophie qui m'ont gardé humble en partageant leurs opinions au sujet de l'ingénierie. Merci à Jo-Ann pour sa sagesse et son encouragement.

Merci Amélie pour tout ce que tu fais pour moi. Ta patience, ton sens de l'humour, ta gentillesse et surtout ta ténacité fut primordiale pour ma réussite cette dernière année. J'ai hâte de pouvoir commencer un autre chapitre avec toi.

DEDICATION

À mes grand-parents Emard et Ferré qui m'ont transmis leur amour pour la langue, la culture, l'éducation, l'agriculture et la foi.

TABLE OF CONTENTS

LIST OF TABLES

LIST OF FIGURES

1.0 INTRODUCTION

1.1. Grape Harvesters

The mechanization of agriculture continues to be a priority in order to minimize extensive manual labour, increase the scale of operations, and improve the quality of the product. Grape harvesting is not an exception as it requires a substantial work force (picking by hand) and time period to complete. Grape harvesting capacity and quality were identified as areas of interest for further study in this project.

"Functionally, grape harvesting is a machine operation in which the fruit is shaken from the vines and caught as it falls; conveyors transport the collected fruit from the catching surfaces to the air-blast cleaners and then into the field transport and storage bins" (Srivastava *et al*, 2006). Researchers started experimenting with harvester prototypes in the early 1950s (Studer, 2000). Numerous configurations were tested in order to find the most suitable design to accommodate the different trellis installations to hold the vines. As a result, grape harvesters became commercially available in California by the end of the 1960s (Johnson, 1977).

As mechanized grape harvesters were being introduced in Europe and North America, a part of the viticulture community remained reluctant towards this new technology in terms of the economic feasibility and performance. In the early 1970's, grape harvesters were only affordable for vineyards that were larger than 90 hectares (220 acres) when compared to harvesting by hand (Johnson, 1977). Given the increasing labour rates, the purchase of a harvester became more justified with time. In addition, these emerging harvesters were approximately five times faster than a typical harvesting crew at the time (Johnson, 1977). Nonetheless, the performance of the

machine was still questioned with respect to the quality of product being delivered for wine production. It was found that harvesters were prone to expelling juice from grapes. By exposing pressed juice to the ambient environment, oxidation and fermentation of the product could occur, consequently causing defects in wine quality (Pezzi, 2008). Also, the detachment of the grape clusters from the vine would often introduce foreign material (leaves, petioles, vine shoots, etc.) into the cleaning system of the harvesters. The material other than grapes (MOG) would transfer unwanted aromas to the expelled juice, thus affecting the wine flavours (Wildenradt, 1974). Some current solutions without modifying the grape harvesters include correctly setting the machine and adapting better vineyards practices during the growth and harvesting seasons (Morris, 1983). More specifically, the speed and frequency of the shaking system at which the harvester operates requires optimized adjustments to minimize juicing and MOG accumulation (Catania, 2009). To further reduce the presence of MOG, vineyards were required to extensively modify their vine growing practices: trellis design, pruning, and trimming operations (Christensen *et al*., 1973). Despite the attempts to improve the quality of the harvested product, these issues are recurrent and will need to be addressed in the next generation of harvesters as shown in Figure 1.1.

Figure 1.1. Grape harvester in Cabernet Sauvignon parcels near Bordeaux, France region.

1.2. Discrete-Element Method

Cundall and Strack (1979) defined the Discrete-Element Method (DEM) as a numerical model that describes the mechanical behaviour of discs and spheres assemblies. The DEM is used to understand and predict particulate and fluid flows for a multitude of applications. The DEM was initially developed by Cundall in 1971 to simulate the behavior of rock mechanics and eventually soil mechanics with Strack in 1979 (ICG, 1999a). The DEM executes a continuous loop between the force-displacement law and Newton's second law of motion (Figure 1.2). This iterative loop essentially calculates contact forces and updates the motions of particles at a set time interval. A variety of contact models specific for particular applications can be applied within the DEM coding. Certain physical properties and parameters need to be defined in order to replicate the actual behavior of the particle material. In most cases, a validation process is required to adjust the DEM simulation in order to increase the accuracy. This encompasses calibrating the simulation behavior with actual tests; certain adjustments may be required until both behaviours coincide. A detailed explanation of the theory behind the DEM can be found in the 3.0 Literature Review section.

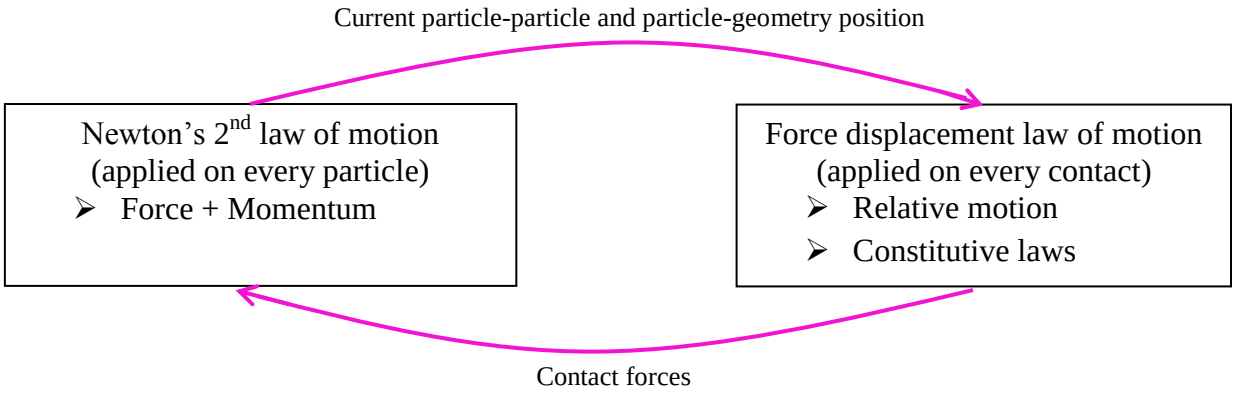

Figure 1.2. DEM continuous loop for every time step (Boerner, 2011).

Since the initial development of the DEM, simulations are now capable of replicating processes in 3-dimensions with both spherical and non-spherical particles (also known as clusters). Advancements in computational capabilities has caused for a rapid progression in DEM modeling. Numerous DEM software packages are available and can be configured for specific applications; some packages may be more suited than others for certain applications. A collection of different coupling interfaces are also available with these DEM packages, which can extend the capabilities of the simulations (i.e. Finite-Element Analysis (FEA), Multi-Body Dynamics (MBD), Computational Fluid Dynamics (CFD), etc.). Industrial fields that use DEM modeling can include: agriculture, construction, mining, natural resource extraction, pharmaceuticals, bio-medical, geology, thermodynamics, manufacturing, military, etc. The specific DEM software package used in this project is EDEM® Version 2.7 (DEM Solutions®, Edinburgh, UK).

1.3. Problem Statement

Crop flow behavior in grape harvesters has been identified as an area of interest for further research. Such interests include the ability to accurately predict the behavior of biological materials in grape harvesters in order to improve the performance of current designs. In high-yielding environments, grape harvesters have increasing difficulties minimizing foreign materials in the final product while trying to increase crop product throughput.

1.4. Organization of the Thesis

The main and specific objectives of the project are outlined in section 2.0 OBJECTIVES. General information pertaining to grape harvesters and their components are described in section 3.0 LITERATURE REVIEW. Information on the development and theories of DEM are also discussed in the 3.0 LITERATURE REVIEW section. The methods and equipment used to measure the physical properties of the biological materials are included in the 4.0 MATERIALS AND METHODS section. The simulation parameters and validation steps are also described for the individual and main crop flow simulations in the section 4.0 MATERIALS AND METHODS. The results for the physical property tests and the simulations are outlined and discussed in detail in the 5.0 RESULTS AND DISCUSSION section. A summary of the project and concluding remarks are included in the section 6.0 SUMMARY AND CONCLUSIONS. A list of recommendations based on the project challenges and results is also outlined in the 7.0 RECOMMENDATIONS section.

2.0 OBJECTIVES

2.1. Main Objective

The primary objective of this project was to develop a main crop flow simulation that optimized the cleaning system of grape harvesters using the Discrete-Element Method (DEM). This was done in terms of crop throughput and product quality for the Cabernet Sauvignon (*Vitis vinifera*) grape variety. Results from field tests were used to validate the simulations of virtual test benches, which were then applied to develop the main crop flow simulation.

2.1.1. Specific Objectives

The initial field tests evaluated the physical characteristics and properties of the biological materials at three locations in France. These results were analyzed and used to create a complete property database for the simulation inputs. The optimization of the cleaning system included the following objectives:

1. To develop and validate individual crop flow simulations (inclined plane, rebound surface, leaf deflections, and crop conveyor trajectory) that replicate the physical characteristics and properties of the biological materials (grapes, leaves, and petioles).

2. To develop and validate a main crop flow simulation for the cleaning process, which is comprised of a conveyor and aspirator. The simulation should combine the simulated parameters of the biological materials previously determined in specific objective 1.
    a. To determine the effects of three cleaning conveyor angles (10°, 15°, and 20°) and three belt rotational speeds (350 rev/min (1.4 m/s), 420 rev/min (1.7 m/s), and 500

rev/min (2.0 m/s)) on the minimization of leaves present after the cleaning process.

b. To maximize the product quality by increasing the leaf aspiration success rate by at least 10% when compared to the conventional conveyor settings for the same crop throughput.

3.0 LITERATURE REVIEW

This section provides general background information on viticulture practices, the general functionality of grape harvesters, and the evolution of cleaning technology. The Discrete-Element Method (DEM) is also described with information related to the initial development, theories, models, and current applications.

3.1. Terroir Influences on Grape Cultivation

Viticulture is a specialized form of horticulture that is limited to a single annual crop, which requires specific growing conditions. By their very nature, grape quality and wine characteristics are dependent of several terroir factors such as climate, grape variety, soil type, and cultural practices (Van Leeuwen *et al.*, 2004). Only select regions possess the climatic conditions required for growing and maturing grapes. A minimal growing season of approximately 180 days is needed for grapes to grow and mature sufficiently for wine making (Mullins *et al.*, 1992). Figure 3.1 displays the world wine producing regions, which are situated between 10^0C and 20^0C isotherms with respect to the ideal latitude locations (30^0N-50^0N and 30^0S-50^0S) (Sallis *et al.*, 2009). Typically, throughout the year the mean temperature extremes should remain within 18.9^0C and -1.1^0C (Prescott, 1965; Jones, 2006). Temperature ranges after the growing season are equally important as they can affect the grapevine health and future production.

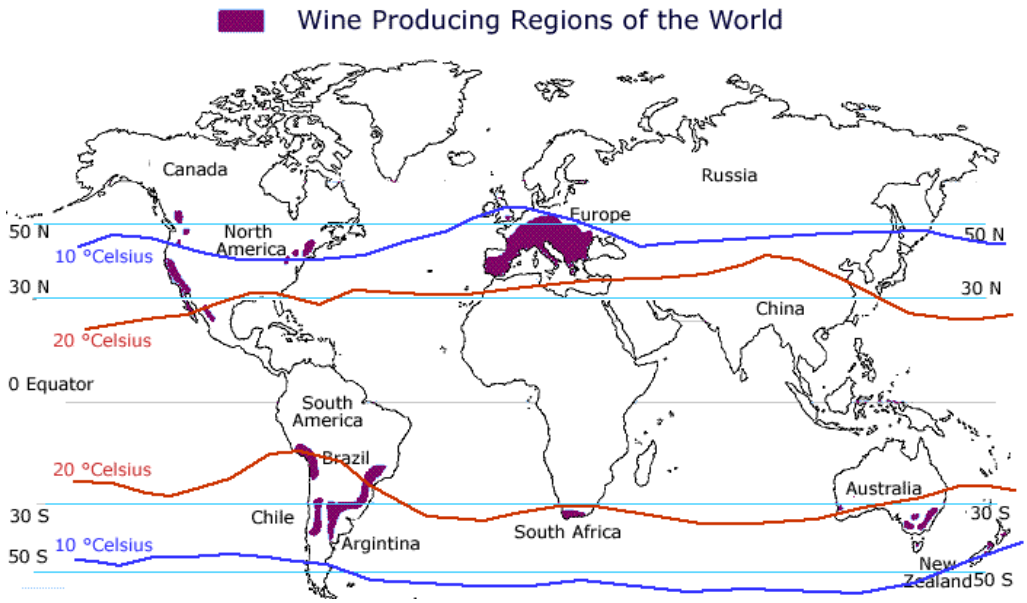

Figure 3.1. Wine producing regions of the world with temperature isotherms (Sallis *et al*., 2009) (courtesy of ThirtyFifty. http://www.thirtyfifty.co.uk/spotlight-climate-change.asp).

The manner in which the soil interacts with the other terroir factors influences the distinctive characteristics of the wine. The mineralogy of the soil dictates the classification and physical properties as it interacts with moisture and the grapevine. As such, the vine and fruit development are influenced by the minerals and the water retention ability of the soil (Van Leeuwen *et al.*, 2004). For instance, the natural level of nitrogen supplied to the vines is dependent of the specific soil type, which directly influences the vine vigour (Van Leeuwen *et al.*, 2000). With respect to precipitation, the soil should maintain a relatively low water retention level (Van Leeuwen *et al.*, 2004). In fact, a water deficient soil will allow for a rapid grape growth, thus keeping the grapes small in size and high in sugar content (Van Leeuwen *et al.*, 2004). For that reason, poor soils will produce better wine despite the ability of deep and rich soils to yield healthy and productive vines (Van Leeuwen *et al.*, 2006). As research continues to

determine the exact correlation between soil and vine growing, certain soil practices could be employed to increase crop yield and quality.

Viticulture regions will select grape varieties based on the regional climate (Jones, 2006). The sensitivity of grapes results in the inability of certain varieties to thrive in multiple regions due to small yet significant climatic differences. Factors such as temperature, precipitation, light, and crop heat units (CHU) can influence the location of different grape varieties (Urhausen *et al.*, 2011). The time required to fully ripen grapes is a principle determining factor in selecting the region. Varieties that include Pinot Noir, Chardonnay, and Gewürztraminer prefer cool climates in higher altitudes as they tend to ripen earlier during the season (Van Leeuwen *et al.*, 2006). Contrarily, regions with warmer climates and lower altitudes are more suitable for late-ripening varieties like Cabernet Sauvignon (Van Leeuwen *et al.*, 2006). The combination of the grape variety and the terroir factors ultimately characterizes the flavours of the wine.

3.2. Grape Harvesters

3.2.1. Historical Context

Like in most agricultural practices, the era of mechanization was preceded by intensive manual labour. Grape harvesting was not an exception as it was done by hand with large groups of peoples. In some circumstances, it is still currently being done by hand. For instance, the region of Champagne in France stipulates that mechanical harvesters cannot be used under any circumstances; harvesting standards have remained the same since the seventeenth century (CIVC, 2012). Although most wine producing regions allow for grape harvesters, select vineyards and wineries pride themselves by manually harvesting. These vineyards believe

manual harvesting may offer prestige, marketing advantages, or even a superior wine. Initial prototyping showed that by correctly setting a grape harvester, the fruit quality was comparable to a hand-harvested fruit; the tests also showed that vine damage was more apparent with the harvesters (Olmo, 1961; Morris, 2000).

A gathering and loading machine as depicted in Figure 3.2 could be considered as one of the initial stages of mechanized grape harvesting. This machine straddles the vines and has a horizontal conveyor perpendicular to the rows. People would then be positioned along the width of the conveyor in each row where they would manually pick the grape clusters. Progressively as the machine advanced, the clusters were placed on the conveyor and transported to a central storage tank. Although this machine still required a substantial workforce, the effort required to transport the harvested crop was greatly diminished. Other iterations of this machine emerged prior to the fully mechanized harvesters.

Figure 3.2. Gathering and loading machine for grape harvesting (with permission of Vagny and Agulhon, 1984).

Researchers started experimenting with harvester prototypes in the early 1950s (Studer, 2000). Numerous configurations were tested in order to find the most suitable design to accommodate the different vine trellis installations. As a result, grape harvesters (Figure 3.3) became commercially available by the end of the 1960s (Johnson, 1977). The trellis system, row spacing, and pruning methods were eventually adapted to accommodate the general configuration of the available harvesters (Gaviglio and Vinsonneau, 2007).

Figure 3.3. Early Chisholm-Ryder Co. grape harvester with flat paddles (Studer, 1969).

3.2.2. Overall Configuration and Functionality

Grape harvesting includes the processes of separating the grapes from the vine, conveying them to a cleaning system, and then placing them into storage bins (Srivastava *et al*., 2006). Since their initial appearance in the 1950's, grape harvesters remain functionally similar. The differences in harvesters can be attributed to the manufacturers who have developed unique strategies and technologies in their machines. Like other agricultural equipment (i.e. harvesters, sprayers, and swathers), grape harvesters are available for purchase in both a pull-type and self-propelled unit.

Pull-type models (Figure 3.4) are designed to trail offset with respect to the pulling tractor in order to fit between the vine rows. Power is supplied hydraulically via the tractor integrated system or by the power take-off (PTO) coupling. The pull-types are generally less expensive and require less powertrain maintenance. The setbacks for these units were the speed of operation and limitation in storage capacity, which required more frequent emptying. Some manufacturers included a dynamically unloading conveyor instead of storage bins. This allows the grapes to be unloaded into a tractor-trailer unit in an adjacent row while harvesting. The general cleaning configuration resembles that of a self-propelled unit.

Figure 3.4. Pull-type grape harvester while harvesting in vines (courtesy of Pellenc Group. http://www.pellenc.com/agriculture/).

Self-propelled models (Figure 3.5) directly straddle individual rows as the grapes are harvested; some harvesters can straddle two rows at a time. Similarly to the pull-type models, the self-propelled harvesters can be equipped with dynamically unloading conveyors. A fully integrated hydraulic or electrical system is coupled to an engine, which supplies the power. A hydrostatic drive system is commonly used as it is the easiest way to supply power to the independent wheels. This type of harvester is generally more manoeuvrable (laterally and vertically with extendable actuators) and versatile because it can be configured to operate on steep hills and rough terrain. The high location of the cabin also facilitates general operations because a greater view is obtained.

Figure 3.5. Self-propelled grape harvester while harvesting in vines (courtesy of CNH Industrial. http://agriculture1.newholland.com/eu/fr-fr).

All grape harvesters are equipped with a harvesting head, which is comprised of three systems: shaking, conveying, and cleaning (Figure 3.6). Since most harvesters straddle individual vines while harvesting, two symmetrical conveying and cleaning systems on each side of the vine are required. Each system requires an elaborate and complex design in order to provide an undamaged crop product at a rapid harvesting rate.

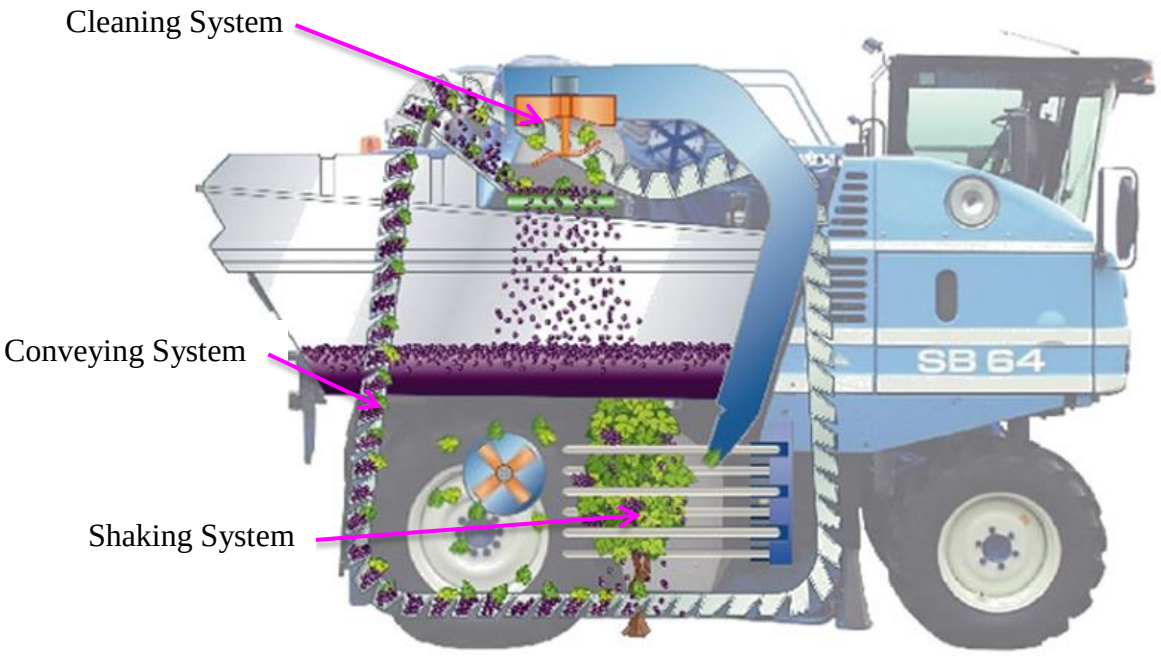

Figure 3.6. General grape harvester component diagram - New Holland SB 64 (courtesy of CNH Industrial. http://agriculture1.newholland.com/eu/fr-fr).

The shaking system (Figure 3.7) is used to detach the grape clusters from the vines on to the conveyor system that ultimately leads them to a cleaning system. Generally, two shaker assemblies face each other and are comprised of individual shaking members. These members can take several different shapes depending on the manufacturer objectives and design. As such, an oscillation of each assembly creates the shaking movement of the shaker members; the frequency and amplitude of the oscillation can be varied based on the operator preferences. This system is internally located within the grape harvester where each assembly is on opposing sides of the vine. The distance separating the two shaking assemblies can be adjusted in order to accommodate a wider vine canopy.

The circular conveying system (Figure 3.8) follows a direct path from underneath the shaking system to the cleaning system (Figure 3.9). The conveyors are usually made up of small buckets linked to a chain that follows the conveying path. The individual buckets are shaped in a manner which allows them to surround the vine stumps. This reduces product and expelled juice losses that may result from the shaking process. The conveying speed of the buckets is proportioned to the ground speed of the harvester to prevent vine damage.

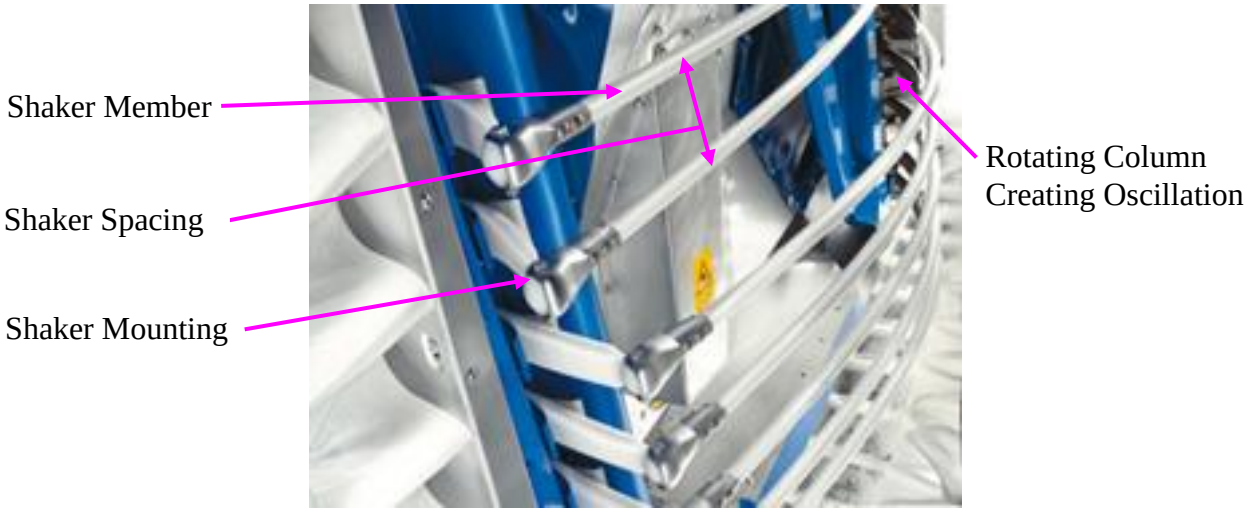

Figure 3.7. Shaking system with horizontal shaker members (courtesy of CNH Industrial. http://agriculture1.newholland.com/eu/fr-fr).

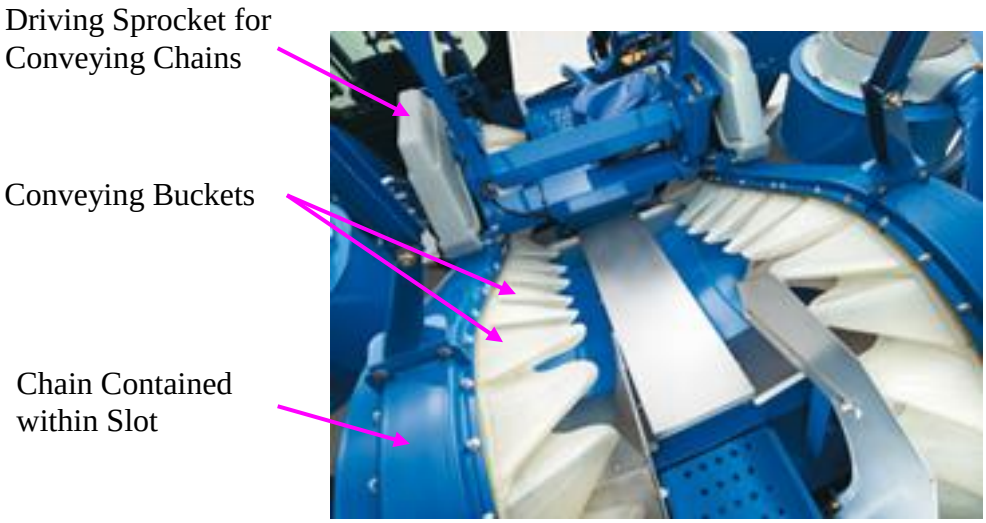

Figure 3.8. Conveying cleaning system equipped with conveying buckets (courtesy of CNH Industrial. http://agriculture1.newholland.com/eu/fr-fr).

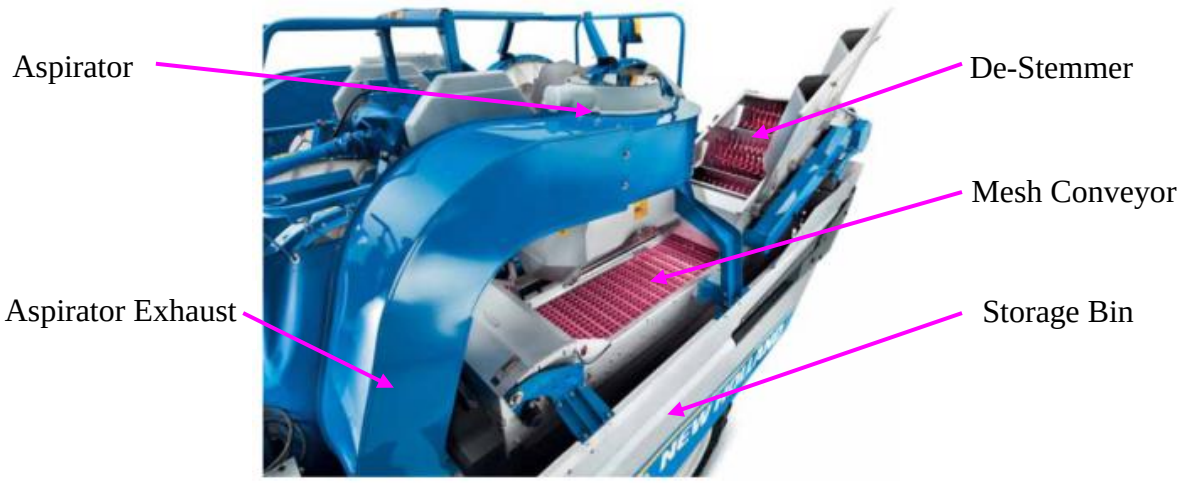

Figure 3.9. Cleaning system equipped with aspirator, mesh conveyor, and de-stemmer (courtesy of CNH Industrial. http://agriculture1.newholland.com/eu/fr-fr).

As the harvester moves forward, all three systems synchronously operate until the storage bins are filled to total capacity. Judging the harvesting yield and storage space becomes crucial in order to prevent reaching full capacity in the middle of a row. Ideally, the harvester would have the storage bins filled once out of a row in order to avoid the presence of a tractor running in between the adjacent rows. At this point, the operator would position the machine where the bins would lie perpendicularly to the transport trailer. The bins could then be emptied by actuating a hydraulic cylinder, which causes the bins to pivot as depicted in Figure 3.10.

Figure 3.10. Grape harvester emptying storage bins (courtesy of CNH Industrial. http://agriculture1.newholland.com/eu/fr-fr).

3.2.3. Grape Harvesting Cleaning Technology

Mechanical grape harvesters have been commercially available since the end of the 1960's (Johnson, 1977). From the very beginning, grape harvester manufacturers have been striving to perfect their products by continually improving their designs. One of the main objectives has been to maximize the quality of the harvested product by minimizing foreign material and juicing. The presence of MOG can transfer undesirable aromas to the wine (Wildenradt, 1974). Additionally, the exposed juice to the ambient environment can result in premature oxidization and fermentation, which can compromise the quality of the wine (Pezzi, 2008). For this reason, competing companies on the market have taken complex approaches in their respective designs to mitigate these recurrent issues. Despite this, most cleaning system designs include a variation of a conveying system, de-stemmer, aspirator, sorter, and storage bin. The order and configuration of these elements are entirely dependent of the specific designs.

3.2.3.1. Air/Product Separation

In agricultural handling processes, air is often used for transporting or separating foreign material from the desired material (Mohsenin, 1984). Grape harvesters have employed this technique given the separation efficiency while harvesting. Generally, the unseparated product stream is subjected to an airflow by means of a blower or aspirator (vacuum flow) depending on the cleaning configuration. Some harvesters are equipped with several stages of aspirators and blowers; all three components of the harvester head may be equipped: shaking, conveying, and cleaning.

The aspirators and blowers are usually a centrifugal type given the high pressure and low air flow required for expelling foreign material. This type prevents damage to the driving mechanism, which is located externally and axially to the impeller. In some cases, a shredding attachment is coupled to the impeller in order to reduce blade damage and prevent excessively large pieces of crop material from being expelled. The fan exhaust is positioned in a manner that directs the undesired crop material away from the harvester. The exhaust typically ejects the material on either side or at the rear of the machine. The fan speed for each unit must be variable in order to suit the particular grape variety and harvesting conditions (i.e. moisture content, juicing, crop density, etc.). When juicing is more prominent, grape juice can be expelled along with the MOG so the fan speed must be carefully adjusted by the operator.

3.2.3.2. Sorting and Separating

The sorting and separating stages of the cleaning system are integrated with the fans to maximize the removal of MOG. Some harvesters use a mesh conveyor (Figure 3.11) with holes large enough to allow the grapes to pass through to the next cleaning stage. Ideally, the foreign material would remain on this conveyor momentarily until evacuated by an aspirator. The mesh conveyor usually transitions the intact grape clusters to the grape de-stemmer. In some cases, a sorting table (U.S. Patent No. 2012/0131894, 2012) is included in the cleaning system; this can be the following stage after the mesh conveyor (Figure 3.12). The table is comprised of numerous rollers placed in-line on the same level. Typically, the single level is made of two series of rollers. The first series evenly spreads the crop material and the second allows the grapes to fall through to the storage bin while the foreign material is ejected over the side. The

first series has the rollers closer together to keep the material on top whereas the second series has small gaps between the rollers to allow grapes through.

Figure 3.11. Mesh conveyor (courtesy of Gregoire Group. http://www.gregoire.fr/fr-fr/).

Figure 3.12. Sorting table with sorting rollers (courtesy of Pellenc Group. http://www.pellenc.com/agriculture/).

3.2.3.3. Grape De-Stemming

Grape separation from the stems (de-stemming) is imperative in wine creation as the remaining stems can cause unwanted flavour characteristics in a wine (Coetzee, 2013). This process requires a specialized apparatus that can either be directly integrated within a grape harvester or within a separate machine that processes the grape clusters after harvesting. It is important to note that in some instances, grape clusters are purposely kept intact as the stems can complement the wine aromas during the fermentation process; this is especially the case for the Pinot Noir and Syrah grape varieties (Goode, 2014). The stems can also provide a greater porosity during the pressing process, which can facilitate draining.

Most grape de-stemmers have a spinning cylindrical rotor configuration (Figure 3.13). The rotor is made up of a cylindrical core with numerous rubber tines, which surround the entire circumference. The spacing of the fingers is sufficiently wide to allow the passage of grapes once separated from the stem. Grape clusters can either be loaded axially or perpendicularly to the rotor, which depends entirely on the grape de-stemmer configuration. The rotor is generally enclosed within a container (rectangular or cylindrical) to prevent material from being projected in all directions. The bottom or tangential sides of the container is perforated to let the grapes pass. Ideally, the stems would be ejected tangentially or laterally (based on the configuration) following the separation of grapes.

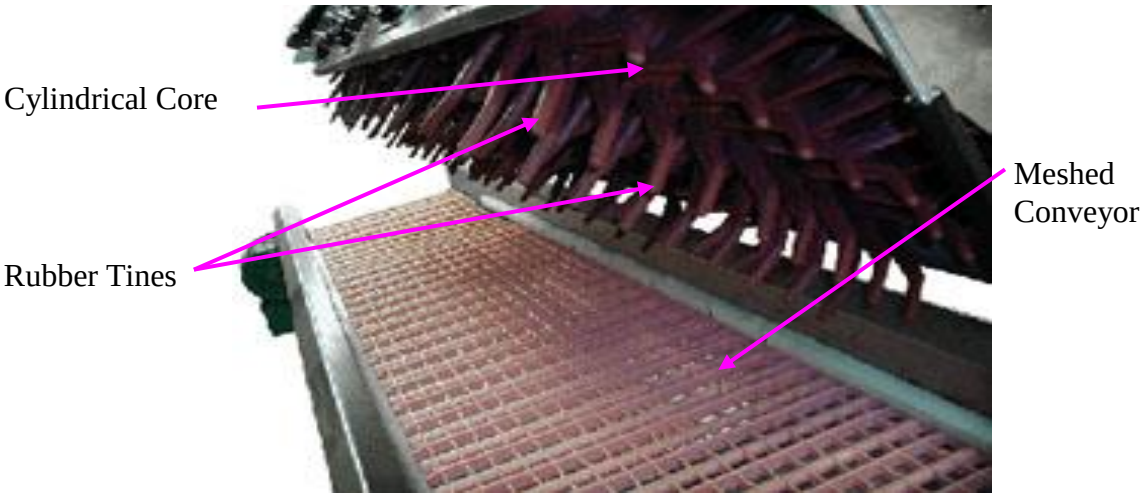

Figure 3.13. Rotary de-stemmer equipped with several rotors and meshed conveyor (courtesy of SOCMA. http://www.socma.info/fr/egreneur-plan).

Due to patent infringement constraints of other apparatuses (E.U. Patent No. 1002467, 1999), some companies have been forced to develop an entirely different way of de-stemming grapes. A linear de-stemming device (U.S. Patent No. 2009/0056297, 2009) was the result of this new development (Figure 3.14). The device is located over a perforated conveyor which propels the grape cluster into the de-stemmer. Similar to a shaking system, the linear separator uses oscillating shaker members to de-stem the clusters of grapes. Two sets of shaker assemblies are located one after another, which provides a sustained separation process. In addition, a raking device utilizes a belt and push arms to force the product between the shaker members. The grapes are progressively passed through the meshed conveyor until the stems are fully separated and ejected.

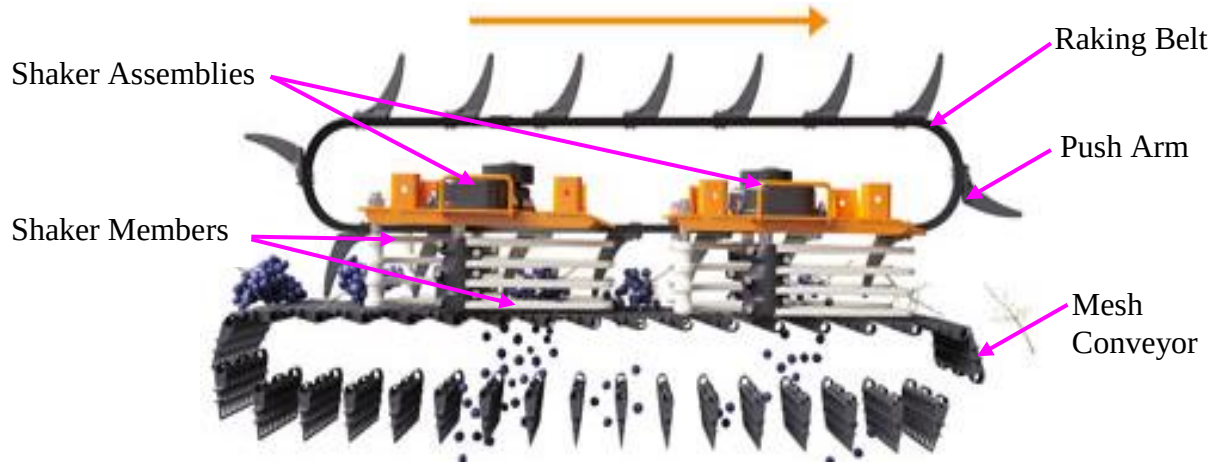

Figure 3.14. Linear de-stemmer with shaker members, raking belt, and mesh conveyor (courtesy of Pellenc Group. http://www.pellenc.com/agriculture/).

3.2.4. Current Technology: Combined Cleaning Systems

Grape harvesters can have a combination of different apparatuses within the cleaning systems. The contents of a system can depend on several factors such as: vine row spacing, grape variety, crop yield, harvesting speed, cost, and even client preference. This following section highlights several manufacturers and some of the current cleaning systems available in harvesters.

3.2.4.1. Combined Linear Separator and Sorting Table Cleaning System (used by Pellenc Group, Pertuis, France):

This cleaning process encompasses three main cleaning instruments (Figure 3.15): aspirator, linear separator (U.S. Patent No. 2009/0056297, 2009), and sorting table (E.U. Patent No. 2030498, 2009), (U.S. Patent No. 2012/0131894, 2012), (E.U. Patent No. 2188067, 2008). The entire cleaning system is stacked over the storage bins in order to capture any juice that may be expelled from the grapes. A vertical conveying system supplies the linear separator mesh conveyor with the collected product from the vine. This effectively removes the individual grapes from the stems and allows them to pass through to the sorting table at the end of the mesh conveyor. The sorting table has two series of rollers that are positioned underneath the linear separator and above the storage bin. The first series evenly distributes the product axially and the second series allows the individual grapes to pass through to the bin. The debris (leaves, petioles, vine shoots) continues on top of the rollers and exits on the sides of the harvester.

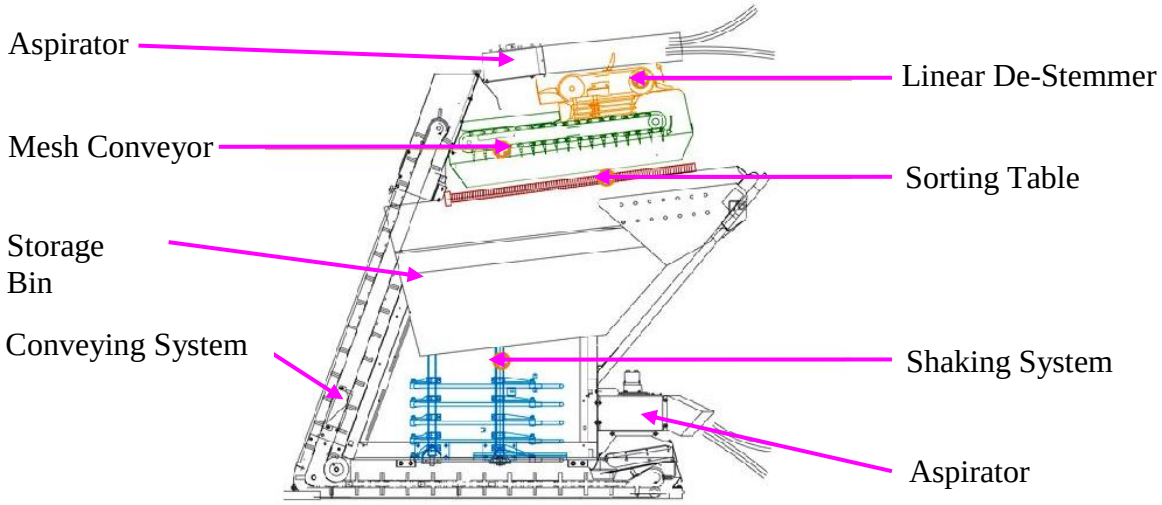

Figure 3.15. Picking head equipped with shaking system, conveying system, and cleaning (courtesy of Pellenc Group. http://www.pellenc.com/agriculture/).

3.2.4.2. Combined Mesh Conveyor and Rotary De-Stemmer Cleaning System (used by Gregoire Group, Treviglio, Italy)

This system uses a mesh conveyor, grape de-stemmer, sorting rollers, and aspirator. All these systems are superimposed over the storage bin (Figure 3.16). This allows the passive collection of any juice that may have inadvertently become separated from the grapes. The mesh conveyor is equipped with a small screw auger in order to evenly spread the incoming product from the initial bucket conveyor. After this step, the product is metered into the rotary grape de-stemmer to remove the stems from the clusters of grapes. The rotor has a solid core with sets of tines that completely surround it tangentially. As it rotates, the product enters radially where the stems are later ejected axially. The individual grapes continue downwards to the sorting rollers. The rollers are helically ribbed, which enables them to effectively spread the product and convey the foreign material on top of the roller as the individual grapes fall through to the bin. During this process, the aspirator induces a negative pressure (suction) over the rollers, which captures the lighter undesirable material. The heavier foreign material that is not

aspirated continues to be conveyed on top of the rollers until it is ejected by a screw auger at the rear of the harvester.

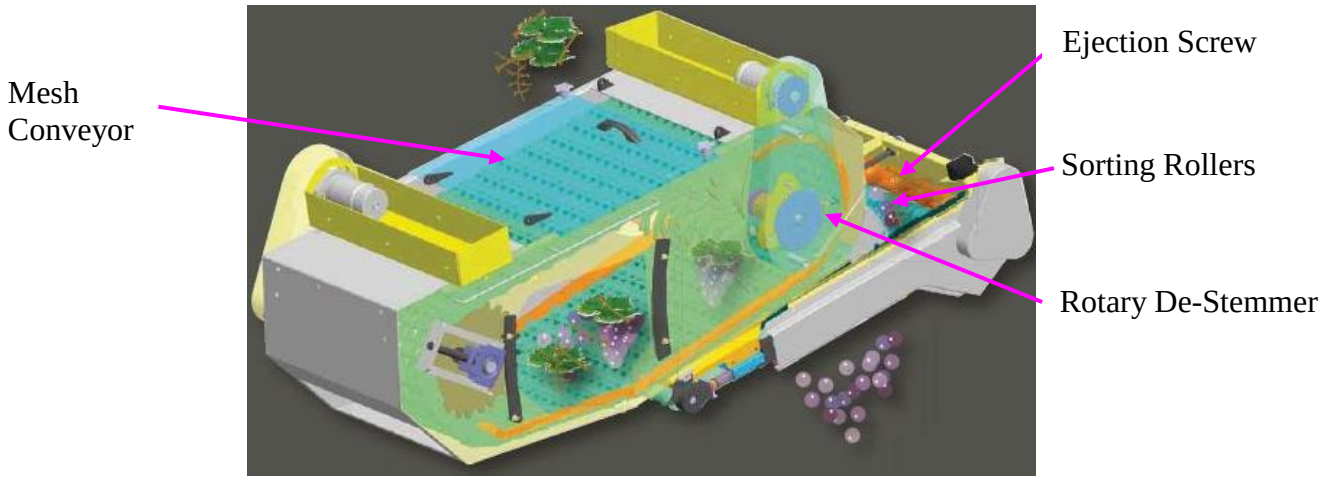

Figure 3.16. Sorting system equipped with mesh conveyor, ejection screw, de-stemmer, and sorting rollers (courtesy of Gregoire Group. http://www.gregoire.fr/fr-fr/).

3.2.4.3. Serpentine Mesh Conveyor Cleaning System (used by Oxbo Int. Corp., Byron, USA)

This system is a multistage cleaning process that incorporates a three-fan system, grape de-stemmer, mesh conveyor, and ejection screw (Figure 3.17). The initial bucket conveyor moves the product from the shakers to the cleaning drop zone. At this transition point, the crop material is subjected to the fan system, which removes the lighter particles such as leaves. After this, the material enters the rotary de-stemmer radially and ejects the stems axially. From there, the crop material continues on the mesh conveyor; the grapes are able to pass through while other particles (i.e. petioles) are kept on the conveyor. These grapes will either fall into a storage bin or on an over-the-row conveyor that unloads them into a separate transport unit (tractor unit with

cart). Meanwhile, the particles that remain on the mesh conveyor will be brought to the ejection screw and eliminated over the sides of the harvesters.

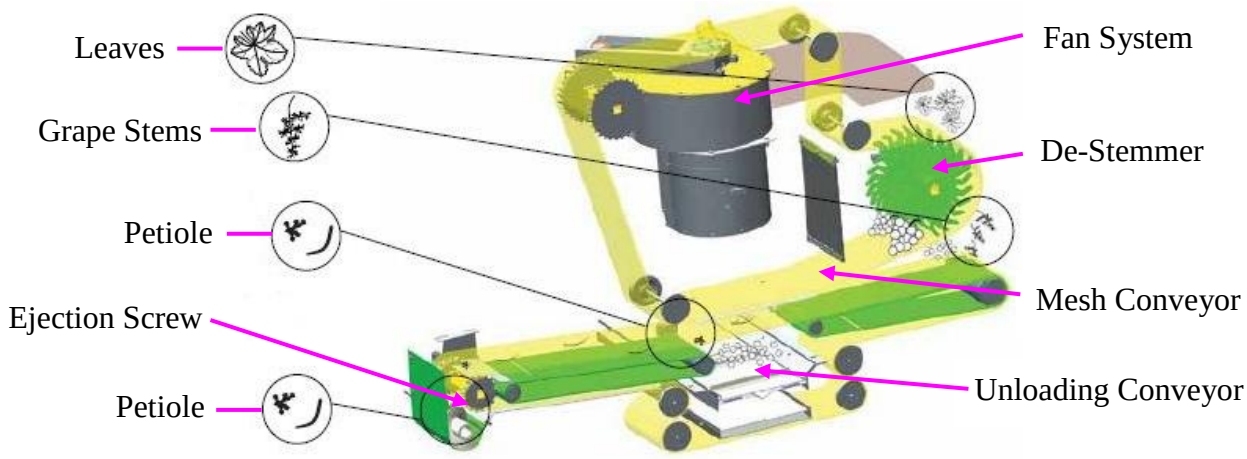

Figure 3.17. Serpentine cleaning system with fan system, de-stemmer, conveyors, and ejection screw (courtesy of Oxbo Int. Corp. http://www.oxbocorp.com/Products/Vineyard/Grape-Harvesters.aspx).

3.2.4.4. Lateral Conveyor Cleaning System (used by CNH Industrial, Coëx, France)

The conveying system is positioned directly over the storage bin and includes a lateral conveyor (Figure 3.18) (E.U. Patent No. 0893049, 1997), aspirator (U.S. Patent No. 2010/0132326, 2010), mesh conveyor (E.U. Patent No. 1336333, 2002), and de-stemmer (E.U. Patent No. 1002467, 1999), (E.U. Patent No. 1002467, 1999). Once the crop material is shaken off the vine, it is brought to the cleaning system (Figure 3.19) using a bucket conveyor. Each bucket empties the crop material on a lateral conveyor, which propels the particles in a continuous trajectory onto a mesh conveyor. An aspirator is located directly over the transition area between these two conveyors. By redirecting the material in a suspended trajectory, it becomes easier for the aspirator to eliminate lighter foreign material. At this point, the already individual grapes can pass through the mesh conveyor to the storage bin. The grape clusters that

are still intact are conveyed into a rotary de-stemmer. The separated stems are evacuated radially from the de-stemmer behind the harvester. Throughout the cleaning process, the juice that is expelled from the grapes falls through the cleaning devices directly to the storage bins.

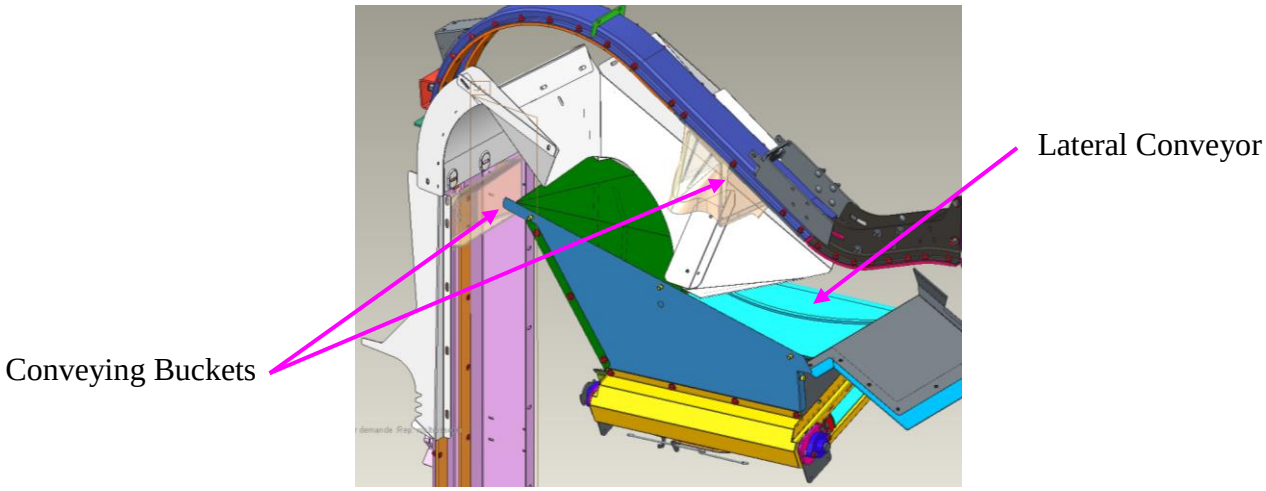

Figure 3.18. Lateral conveyor for cleaning system with conveying buckets (courtesy of CNH Industrial. http://agriculture1.newholland.com/eu/fr-fr).

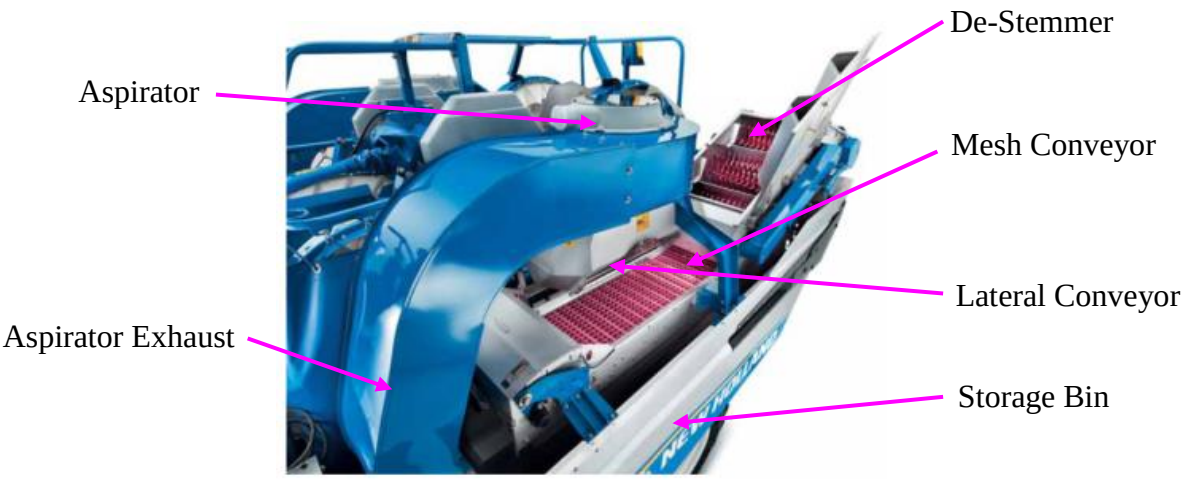

Figure 3.19. Cleaning system equipped with lateral, aspirator, mesh conveyor, de-stemmer, and storage bin (courtesy of CNH Industrial. http://agriculture1.newholland.com/eu/fr-fr).

3.2.4.5. Combined Air Screen and Sorting Rollers Cleaning System (used by CNH Industrial, Coëx, France)

This cleaning system is an add-on option to the conventional lateral conveyor cleaning system. It is comprised of two cleaning processes: pre-sorter (E.U. Patent No. 2348808, 2009) and separator (U.S. Patent No. 2014/0221060, 2014). The pre-sorter (Figure 3.20), which uses two series of rollers, replaces the mesh conveyor. The first helical series ensure an even spread of the individual grapes and the clusters. The second series of rollers are helically ribbed with spacing that allows the individual grapes to pass through to the separator. The clusters of grapes continue on top of the rollers to the de-stemmer. The separator has a series of rollers (Figure 3.21) and a perforated air screen (Figure 3.22). As the individual grapes enter the separator, the rollers evenly spread the grapes before going over the screen. The perforated screen is angled downwards and has forced air (supplied by independent centrifugal fan) that creates an air cushion. As the grapes pass over, they fall into the storage bin whereas the foreign materials (petiole, leaves, twigs, damaged grapes, etc.) are ejected off the sides of the harvester.

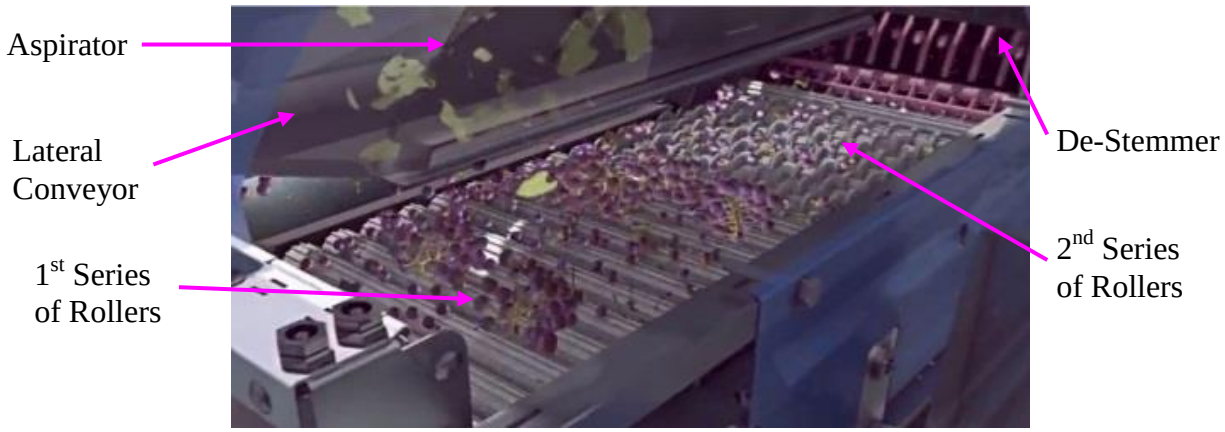

Figure 3.20. Pre-sorter cleaning system with two additional of rollers leading into the de-stemmer (courtesy of CNH Industrial. http://agriculture1.newholland.com/eu/fr-fr).

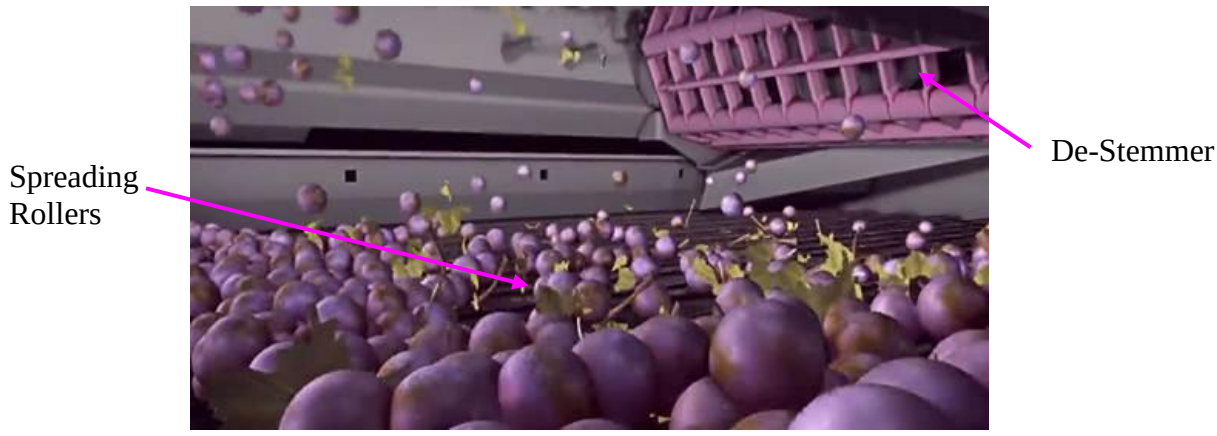

Figure 3.21. Roller separator cleaning system conveying crop material to air screen (courtesy of CNH Industrial. http://agriculture1.newholland.com/eu/fr-fr).

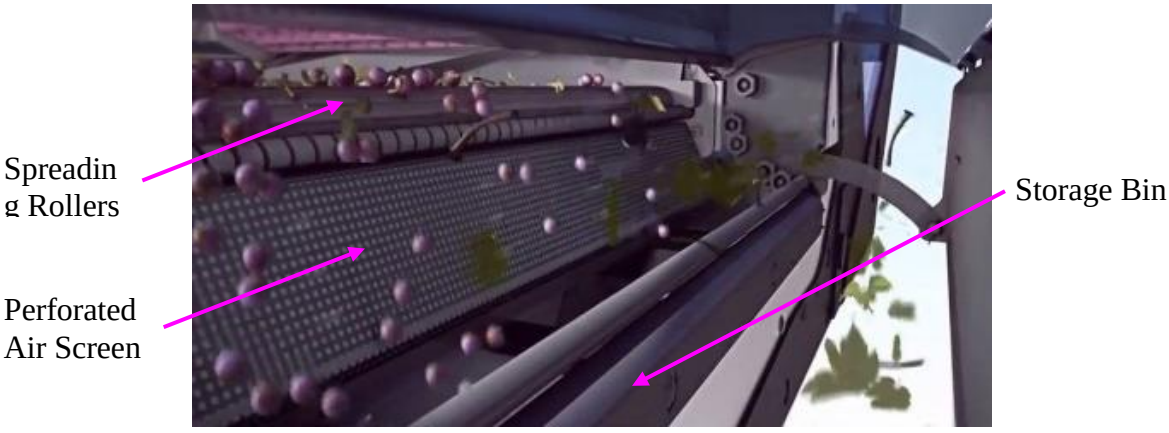

Figure 3.22. Air screen cleaning system removing foreign materials while allowing grapes to pass to storage bin (courtesy of CNH Industrial. http://agriculture1.newholland.com/eu/fr-fr).

3.3. Discrete-Element Method

3.3.1. Development of DEM

Since the initial development of DEM by Cundall and Strack in 1979, industrial applications of the DEM have been expanded to numerous sectors (i.e. geological, mineralogical, pharmaceutical, agricultural, etc.). These sectors are looking to predict material behaviour without having to conduct physical experiments. This minimizes time and cost associated with prototyping.

Table 3.1 shows the development of the DEM modeling scale in simulation software. Initial simulations were limited to 2-dimensions (2D) with very simple geometrical contacts. The development in computer hardware has allowed for a rapid progression in the DEM modeling scale, which can now support millions of particles in both 2D and 3-dimensions (3D) (Munjiza *et al*., 2008). The number of particles used in modelling is entirely dependent of the available computational power. Therefore, the computational efficiency is subject to the modeling parameters (i.e. time step, domain, contact force models, bond models, etc.).

Table 3.1. Evolution of DEM modeling scale (Cleary, 2009)

Year	Number of Particles
1995	1,000 Circular Particles (2D)
2001	250,000 Spheres (3D)
2005	1 Million Non-Spherical Particles (3D)
2007	15 Million Non-Spherical Particles (3D)

3.3.2. General Theory

DEM utilizes the force-displacement law (eqs. 3.1 and 3.2) and Newton's second law of motion (eqs. 3.3 and 3.4); the force displacement law detects the contact forces based on the displacements and Newton's law accounts for the forces acting on a particle and assigns it a corresponding motion (Cundall and Strack, 1979). Every time step begins by updating the contacts based on particle and geometry positions; the force-displacement and motion laws are applied after this step (ICG, 1999a). The force-displacement law is applied first to update the contact forces. Subsequently, Newton's second law is applied to each particle in order to update the respective velocities and positions based on the previously updated contact forces.

During collision between particle 1 and particle 2:

$$\Delta F_n = k_n(\Delta n) = k_n\left[(\dot{x}_{P1} - \dot{x}_{P2})\left(\frac{x_{P2} - x_{P1}}{D}\right)\right]\Delta t \tag{3.1}$$

$$\Delta F_s = k_s(\Delta s) = k_s\left[(\dot{x}_{P1} - \dot{x}_{P2})t - \left(\dot{\theta}_{P1}R_{P1} - \dot{\theta}_{P2}R_{P2}\right)\right]\Delta t \tag{3.2}$$

where,

ΔF_n = Increment in normal force (N)
ΔF_s = Increment in shear force (N)
k_n = Normal stiffness (N/m)
k_s = Shear stiffness (N/m)
Δn = Normal displacement increment/overlap (m)
Δs = Tangential displacement increment/overlap (m)
x_{P1} = Centre position of particle 1 (m)
x_{P2} = Centre position of particle 2 (m)
$\dot{x}_{P1}$ = Linear velocity of particle 1 (m/s)
$\dot{x}_{P2}$ = Linear velocity of particle 2 (m/s)
D = Distance between centres of particles (m)
$\dot{\theta_{P1}}$ = Angular velocity of particle 1 (rad/s)
$\dot{\theta_{P2}}$ = Angular velocity of particle 2 (rad/s)

R_{P1} = Radius of particle 1 (m)
R_{P2} = Radius of particle 2 (m)
t = Time (s)
Δt = Time increment (s)

In the force-displacement equations, the relative contact displacement in the normal (Δn) and tangential (Δs) directions can be defined as overlap (ICG, 1999a). Overlapping occurs since the particles are characterized as rigid. The overlaps are used to account for particle deformation with respect to other particles and geometries; the overlap magnitude is proportional to the contact forces (Cundall and Strack, 1979). Although overlapping is used to replicate particle deformation, the overlap magnitude with respect to the particle size is relatively small.

$$F_n = m_n \ddot{x}_n \tag{3.3}$$

$$M_n = I_n \ddot{\theta}_n \tag{3.4}$$

(see nomenclature below)

Velocity equation 3.5 and equation 3.6 are derived from Newton's second law of motion (eqs. 3.3 and 3.4 respectively). An additional derivation of these equations produces the particle position (eq. 3.7) and rotation (eq. 3.8) equations. The DEM cycle uses these velocity equations in the force-displacement equations (eqs. 3.1 and 3.2) while updating the position and rotations of the particles (eqs. 3.7 and 3.8); this cycle is repeated for each new time increment (Cundall and Strack, 1979).

During time interval $t_{N-1/2}$ to $t_{N+1/2}$

$$\dot{x}_{N+1/2} = \dot{x}_{N-1/2} + \left[\frac{F}{m}\right]_N \Delta t \tag{3.5}$$

$$\dot{\theta}_{N+1/2} = \dot{\theta}_{N-1/2} + \left[\frac{M}{I}\right]_N \Delta t \tag{3.6}$$

$$x_{N+1} = x_N + \dot{x}_{N+1/2}\Delta t \tag{3.7}$$

$$\theta_{N+1} = \theta_N + \dot{\theta}_{N+1/2}\Delta t \tag{3.8}$$

where,

F_n = Normal or shear force (N)
M_n = Moment (N·m)
m_n = Mass (kg)
$\ddot{x}_n$ = Linear acceleration (m/s^2)
$\dot{x}$ = Linear velocity (m/s)
x = Particle position (m)
$\ddot{\theta}_n$ = Angular acceleration (rad/s^2)
$\dot{\theta}_n$ = Angular velocity (rad/s)
θ_n = Particle rotation (rad)
Δt = Time increment (s)
I_n = Moment of inertia (kg·m^2)

3.3.2.1. DEM Time Steps

Time Steps are the time intervals where the interaction calculations (motion, force, contact, etc.) of the particles take place. The selected time steps are typically short enough that during a single time step, disturbances may only be transferred from a particle to the immediate neighbours; both velocities and accelerations are assumed to be constant for a single time step (Cundall and Strack, 1979). Cundall and Stack describe the key feature of DEM as the resultant forces of a given particle being solely caused by the interactions with other contacting particles, which in turn enable the determination of a non-linear interaction of numerous particles without the need for large memory capabilities or an iterative procedure (1979).

A lower time step is often required to accurately account for higher forces with particles (DEM Solutions®, 2015). These shorter time steps make the simulation even more computationally expensive; this becomes the compromise since a longer time step could result in less accurate interactions. For instance, fast-moving particles could potentially skip over several others before a contact would finally occur between them.

The selected time step can be displayed in seconds and as a percentage of the Rayleigh time step (eq. 3.9); the Rayleigh time refers to the time required for a shear wave to propagate through a solid particle (DEM Solutions®, 2015). As the number of potential contacts between particles increases, a smaller percentage of the Rayleigh time step is optimal for a sufficient accuracy in the simulation. A 20% time step is recommended if the total number of contacts per particle is 4 or more; 40% can be suitable for a lower number of contacts (DEM Solutions®, 2015).

$$T_R = \frac{\pi R \left(\frac{\rho}{G}\right)^{1/2}}{(0.1631v + 0.8766)} \quad (3.9)$$

where,

T_R = Rayleigh time step (s)
R = Particle radius (m)
ρ = Particle density (kg/m^3)
G = Shear modulus (Pa)
v = Poisson's ratio (dimensionless)

3.3.2.2. Physical Properties

The first column of Table 3.2 outlines the required inputs in the DEM software for both the geometry and particle materials (Boerner, 2011). The interaction properties between the biological materials themselves and the geometry materials are also displayed. Every possible interaction needs to be defined in order to perform the simulation calculations. The second column of Table 3.2 shows the calculated values based on the entered properties, particles, and geometries (Boerner, 2011). The selected contact models will dictate the calculation method by using the appropriate equations and iterative loops; these values may differ from one contact model to another. Additional material properties may be required depending on the selected contact model (i.e. yield strength, cohesion energy, particle velocity, etc.). Model validation may be required in order to obtain realistic and accurate results.

Table 3.2. DEM simulation input properties and output values for particles and geometries (Boerner, 2011).

Required Material Properties	Calculated Values from Simulation

• General
  ○ Density (kg/m^3)
  ○ Shear modulus (Pa)
  ○ Poisson's ratio (dimensionless)
  ○ Particle diameter (m)
• Interaction
  ○ Coefficient of restitution (dimensionless)
  ○ Coefficient of static friction (dimensionless)
  ○ Coefficient of rolling friction (dimensionless)
	• Position
	  ○ x, y, z coordinates (m)
	• Temporal dependence
	  ○ Velocity (V_x, V_y, V_z) (m/s)
	  ○ Angular velocity (rad/s)
	  ○ Mass (kg)
	  ○ Volume (m^3)
	• Force/Energy
	  ○ Total energy (J)
	  ○ Potential energy (J)
	  ○ Kinetic energy (J)
	  ○ Rotational energy (J)
	  ○ Total force (N)
	  ○ Compression force (N)
	  ○ Momentum (N·s)
	• Inter-Particle
	  ○ Collision frequency (Hz)
	  ○ Force in bonds (N)

3.3.3. Contact Models

Contact models are used to represent the contact force behaviour between two objects (particle-particle or particle-geometry) due to the displacements in the normal and tangential directions. When the relative motion of two particles generates a force between them, the particles are considered to be in contact (ICG, 1999c). Contacts are not limited to particles that are in physical contact; bonded particles can have small spaces between them while still being considered in contact (ICG, 1999c). The selected contact model dictates the behavior of particles when contacts occur with geometries and other particles. The following contact models are available with the currently used EDEM® software (version 2.7).

3.3.3.1. Hertz-Mindlin (no slip)

The Hertz-Mindlin contact model is a non-linear contact approximation for particles, which models the impacts as interconnecting spring and dash pots in series (Boerner, 2011). The model uses normal (eq. 3.10) and tangential (shear) (eq. 3.11) force components that are based on the Hertzian contact theory (1882) and on the Mindlin-Deresiewicz (1952) work respectively. Cundall and Strack (1979) used the Coulomb friction law with the tangential force within this contact model. Both the normal and tangential forces are used in the force displacement-law cycle, which occurs at every time step.

$$F_N = \frac{4}{3} E_{eq} \sqrt{R_{eq}} \Delta n^{3/2} \tag{3.10}$$

$$F_s = -k_s \Delta s \tag{3.11}$$

where,

$$E_{eq} = \frac{E_{P1}E_{P2}}{[E_{P1}(1-v_{P2}^2)] + [E_{P2}(1-v_{P1}^2)]} \tag{3.12}$$

$$R_{eq} = \frac{R_{P1}R_{P2}}{R_{P1}+R_{P2}} \tag{3.13}$$

$$k_N = 2E_{eq}\sqrt{R_{eq}\Delta n} \tag{3.14}$$

$$k_s = 8G_{eq}\sqrt{R_{eq}\Delta n} \tag{3.15}$$

$$G_{eq} = \frac{G_{P1}G_{P2}}{[G_{P1}(2-v_{P2})] + [G_{P2}(2-v_{P1})]} \tag{3.16}$$

(see nomenclature below)

DEM solutions® has included the Tsuji *et al*. (1992) damping components for both the normal (eq. 3.17) and tangential (eq. 3.18) forces, which incorporate the coefficient of restitution (2014). These forces also account for the material stiffness, mass, and relative velocity with respect to the normal and tangential directions. Including the damping forces within the model recreates the effects of energy dissipation during particle impacts.

$$F_{ND} = -2\sqrt{\frac{5}{6}}\beta\sqrt{k_N m_{eq}}v_{Nrel} \tag{3.17}$$

$$F_{SD} = -2\sqrt{\frac{5}{6}}\beta\sqrt{k_s \cdot m_{eq}} \cdot v_{Trel} \tag{3.18}$$

(see nomenclature below)

where,

$$m_{eq} = \frac{m_{P1} m_{P2}}{m_{P1} + m_{P2}} \tag{3.19}$$

$$\beta = \frac{\ln e}{\sqrt{(\ln e)^2 \pi^2}} \tag{3.20}$$

DEM Solutions® accounts for the rolling friction by using the Sakaguchi *et al*. (1993) contact independent directional constant torque model (2014). Equation 3.21 calculates the rolling friction torque and applies it to contacting surfaces (DEM Solutions®, 2014); the calculated value is applied in the velocity (eq. 3.6) and position (eq. 3.8) equations.

$$\tau = -\mu_r F_N R \omega \tag{3.21}$$

where,

F_N = Normal force (N)
F_S = Tangential (shear) force (N)
F_{ND} = Normal damping force (N)
F_{SD} = Tangential (shear) damping force (N)
E_{P1} = Modulus of elasticity of particle 1 (Pa)
E_{P2} = Modulus of elasticity of particle 2 (Pa)
v_{P1} = Poisson's ratio of particle 1 (dimensionless)
v_{P2} = Poisson's ratio of particle 2 (dimensionless)
R_{P1} = Radius of particle 1 (m)
R_{P2} = Radius of particle 2 (m)
k_n = Normal stiffness (N/m)
k_s = Shear stiffness (N/m)
Δn = Normal displacement/overlap increment (m)
Δs = Tangential displacement/overlap increment (m)
G_{P1} = Shear modulus of particle 1 (Pa)
G_{P2} = Shear modulus of particle 2 (Pa)
v_{Nrel} = Relative normal velocity (m/s)
v_{Trel} = Relative tangential velocity (m/s)

m_{P1} = Mass of particle 1 (kg)
m_{P2} = Mass of particle 2 (kg)
e = Coefficient of restitution (dimensionless)
τ = Rolling friction torque (N·m)
μ_r = Coefficient of static friction (dimensionless)
R = Distance between contact point and centre of mass (m)
ω = Angular velocity vector at contact point (dimensionless)

The Hertz-Mindlin model is also used in conjunction with the relative wear model for the particle-geometry interaction. The relative wear model records areas of geometries that are subjected to high impacts (normal) and abrasive (tangential) wear by the particles (DEM Solutions®, 2015). The particle velocity and forces acting on the geometries are accounted within the model (DEM Solutions®, 2015). The analyst tool is able to extract cumulative wear on specific geometries, which allows the user to identify any potential wear points. The geometry designs can be refined by using this particle contact model. Despite this, the relative wear model is limited by the inability to predict the material removal rate (DEM Solutions®, 2014).

3.3.3.2. Hertz-Mindlin (no slip) with RVD Rolling Friction

Hertz-Mindlin contact model that uses Relative Velocity Dependent (RVD) rolling friction in an alternate implementation of rolling friction based on velocity and deformation at the contacts (DEM Solutions®, 2015). Contrarily to the conventional Hertz-Mindlin rolling friction, the relative angular velocity unit vector (ω_{rel}) of two contacting particles is used instead in the applied torque calculation (eq. 3.22). This model can also be configured to include the relative wear model.

$$\tau = -\mu_r F_N R \omega_{rel} \tag{3.22}$$

where,

τ = Rolling friction torque (N·m)
μ_r = Coefficient of static friction (dimensionless)
F_N = Normal force (N)
R = Distance between contact point and centre of mass (m)
ω_{rel} = Relative angular velocity (dimensionless)

3.3.3.3. Hertz-Mindlin with Archard Wear

Same functionality as the default Hertz Mindlin model, but offers more features for wear analysis on geometry and includes the relative wear model. This function is capable of measuring the removed material from specific geometries caused by sliding and abrasive wear from excessive particle contact, which is based on a calibrated constant from material testing (DEM Solutions®, 2015). The removed volume of material is determined by using the Archard equation (1953) (eq. 3.23). DEM solution uses the calculated volume from the equation to predict the wear of the geometry (2014).

$$Q = \frac{KF_N d_t}{H} \tag{3.23}$$

where,

Q = Removed material volume (m^3)
K = Wear constant (dimensionless)
F_N = Normal force (N)
d_t = Travelled distance (m)
H = Hardness of softest surface (Pa)

3.3.3.4. Hertz-Mindlin with Heat Conduction

Model that uses the Hertz-Mindlin contact model and the update temperature function model from the particle body force to calculate the heat flux between contacting particles and external heat sources (DEM Solutions®, 2015). The model accounts for the diffusion of the heat flux through particle overlap and the user-defined particle thermal conductivity (DEM Solutions®, 2015). This model is particularly useful in simulating the convective heat transfer in higher-numbered particle applications. Equation 3.24 is a linear model used to simulate the heat flux transfer between two contacting particles (Chaudhuri *et al*., 2006). DEM Solutions® also uses the update temperature model (eq. 3.26) after calculating all the heat fluxes; the temperature gradient between the particles and the environment adjusts the temperatures of the individual particles (2014).

$$Q = h_c \Delta T \tag{3.24}$$

$$h_c = \frac{4k_{P1}k_{P2}}{k_{P1} + k_{P2}} \left[\frac{3F_N r_{eq}}{4E_{eq}}\right]^{1/3} \tag{3.25}$$

$$mC_p \Delta T = \sum Q_{heat} \tag{3.26}$$

where,

Q = Heat flux between particle 1 and 2 (W)
Q_{heat} = Specific heat capacity (J)
h_c = Heat transfer coefficient (W/K)
ΔT = Temperature gradient between particle 1 and 2 (K)
k_{P1} = Thermal conductivity of particle 1 (W/m·K)
k_{P2} = Thermal conductivity of particle 2 (W/m·K)
F_N = Normal force (N)
m = Mass of particle material (kg)
C_p = Specific heat capacity (J/kg·K)

3.3.3.5. Hertz-Mindlin with Bonding

The model applies the Hertz-Mindlin contact model while allowing particles to bond with one another (cannot bond to geometries); the relative wear model can also be used with this contact model. The bond between two particles is created with a virtual cylinder, which overlaps the two spheres and acts as cementing glue. The bonded disk radius (R_B) refers to the virtual cylinder radius. The bond uses the following parameters for the bond formation, which are customizable by the user: normal stiffness, shear stiffness, critical normal stress, critical shear stress, and bonded disk radius (DEM Solutions®, 2015). The normal and shear stiffness characterize the particle assembly rigidity. The Cundall and Potyondy (2004) equations, which describe the elastic force (eqs. 3.27 and 3.28) and moment (eqs. 3.29 and 3.30) increments, are updated at each time step. The force and moment equations are used to verify the critical normal and shear stress conditions (eqs. 3.33 and 3.34 respectively). The critical normal and shear stress refers to the maximum normal and shear stress that the bond can withstand before failure (DEM Solutions®, 2015).

$$\Delta F_N = -v_N k_N A \Delta n \tag{3.27}$$

$$\Delta F_S = -v_T k_S A \Delta s \Delta t \tag{3.28}$$

$$\Delta M_N = -\omega_N k_S J \Delta t \tag{3.29}$$

$$\Delta M_S = -\omega_T k_N \frac{J}{2} \Delta t \tag{3.30}$$

(see nomenclature below)

where,

$$A = \pi R_B^2 \tag{3.31}$$

$$J = \frac{1}{2}\pi R_B^4 \tag{3.32}$$

$$\sigma_{max} < \frac{-F_N}{A} + \frac{2M_S}{J} R_B \tag{3.33}$$

$$\tau_{max} < \frac{-F_S}{A} + \frac{M_N}{J} R_B \tag{3.34}$$

where,

ΔF_N = Normal force increment (N)
ΔF_S = Tangential (shear) force increment (N)
ΔM_N = Normal moment increment (N·m)
ΔM_S = Tangential (shear) moment increment (N·m)
v_N = Normal velocity (m/s)
v_T = Tangential velocity (m/s)
ω_N = Normal angular velocity (rad/s)
ω_T = Tangential angular velocity (rad/s)
k_n = Normal stiffness (N/m)
k_s = Shear stiffness (N/m)
Δn = Normal displacement/overlap increment (m)
Δs = Tangential displacement/overlap increment (m)
Δt = Time step increment (s)
σ_{max} = Critical normal stress (Pa)
τ_{max} = Critical shear stress (Pa)
R_B = Bonded disk radius (m)

The parallel-bond model and the contact-bond model are two types of models that can be used with the DEM simulation software. The contact-bond model acts only at the contact point between particles, whereas the parallel-bond model acts over the virtual cylinder cross section (ICG, 1999b). Both the forces and moments can be transferred through the parallel-bond, while

only the forces are transferred with a contact-bond; some DEM software packages can support both bond models at the same time (ICG, 1999b). Although the EDEM® Hertz-Mindlin contact model could be considered a parallel bond, the torque feedback is only implemented when the critical shear stress is exceeded and the bond brakes. The torque feedback does not allow a moment transfer through the bond as would a typical parallel bond.

It is important to note that the bonds will only form at the specified bond time and will only be broken if the maximum bond strength is surpassed. Higher bond strengths may require a lower than normal time step to accurately capture the forces between particles (DEM Solutions®, 2015).

3.3.3.6. Hertz-Mindlin with JKR Cohesion

The Hertz-Mindlin Johnson-Kendall-Roberts (JKR) cohesion contact model is capable of replicating the cohesion between particles and adhesion to geometry. This model was initially intended to simulate the Van der Waals interaction forces involved in the fine dry powder flows (DEM Solutions®, 2015). Currently, this model is used to account for the cohesion effects of moisture in large bulk flows (DEM Solutions®, 2015). The cohesion or adhesion effect for particles is user-defined by specifying the surface energy for a particular interaction (particle-particle or particle-geometry).

The separation of two contacting bodies requires mechanical work to be expended to create a new surface and overcome the adhesive forces (Johnson *et al*., 1971). The free surface energy is

also defined by Johnson *et al*. (1971) as "the required energy to create a unit area of a new surface". Hertz original equation (eq. 3.35) for the contact radius did not take into account the surface energy effect. Johnson *et al*. (1971) developed another equation (eq. 3.36) based on Hertz's original equation, which accounted for the surface energy effect. This equation can be derived into equation 3.37, which yields the required force to separate the two contacting spheres (Johnson *et al*., 1971). DEM Solutions® calculates this maximum cohesion force when the particle is not in physical contact with the surface, but within the maximum acceptable gap calculated from equation 3.38 (2014).

$$a = \left[\frac{R_{eq}F_C}{K_{eq}}\right]^{1/3} \tag{3.35}$$

$$a = \left[\frac{R_{eq}}{K_{eq}}\left(F_C + 3\gamma\pi R_{eq} + \sqrt{\left\{6\gamma\pi R_{eq}F_C + \left(3\gamma\pi R_{eq}\right)^2\right\}}\right)\right]^{1/3} \tag{3.36}$$

$$F_{Cmax} = -\frac{3}{2}\gamma\pi R_{eq} \tag{3.37}$$

$$\delta_{gap} = -\sqrt{\frac{4\pi\gamma a_c}{E_{eq}}} + \frac{a_c^2}{R_{eq}} \tag{3.38}$$

(see nomenclature below)

where,

$$K_{eq} = \frac{4}{3\pi(k_1+k_2)} \tag{3.39}$$

$$k_1 = \frac{1-v_1^2}{\pi E_1} \tag{3.40}$$

$$k_2 = \frac{1-v_2^2}{\pi E_2} \tag{3.41}$$

$$a_c = \left[\frac{9\pi\gamma R_{eq}^2}{2E_{eq}}\left(\frac{3}{4} - \frac{1}{\sqrt{2}}\right)\right]^{1/3} \tag{3.42}$$

(see nomenclature below

In EDEM®, the tangential elastic force, normal dissipation force, and tangential dissipation force are calculated in the same way as the default Hertz-Mindlin contact model (2014). The cohesion and adhesion behavior are simulated by applying a normal force (JKR force) on a particle, which opposes the separation from the surface. The JKR cohesion force is added to the Hertz-Mindlin force, which equates to the total normal force acting on a particle. In an instance when a particle is in physical contact with this surface, the JKR normal force magnitude (eq. 3.43) is a function of the particle overlap (eq. 3.44) and the user defined surface energy (DEM Solutions®, 2014).

$$F_C = -4\sqrt{\pi\gamma E_{eq}}a^{3/2} + \frac{4E_{eq}}{3R_{eq}}a^3 \tag{3.43}$$

$$\delta_{overlap} = \frac{a^2}{R_{eq}} - \sqrt{\frac{4\pi\gamma a}{E_{eq}}} \tag{3.44}$$

where,

a = Contact radius (m)
R_1 = Radius of sphere 1 (m)
R_2 = Radius of sphere 2 (m)
v_1 = Poisson's ratio of sphere 1 (dimensionless)
v_2 = Poisson's ratio of sphere 2 (dimensionless)
E_1 =Young's modulus of sphere 1 (Pa)
E_2 =Young's modulus of sphere 2 (Pa)
F_C = Cohesion force (N)
F_{Cmax} = Maximum cohesion force (N)
γ = Energy per unit contact area (J/m^2)
δ_{gap} = Maximum gap between particle and surface (m)
$\delta_{overlap}$ = Particle overlap with contacting surface (m)

3.3.3.7. Linear Cohesion

The linear cohesion contact model alters the Hertz-Mindlin contact model by incorporating a normal cohesion and adhesion force for the particle and geometry interactions respectively (DEM Solutions®, 2015). Both contact models need to be selected in order to implement the calculations. The cohesion between particles and the adhesion to geometries can be adjusted by the user-defined cohesive energy density. This density is a function of the particle contact radius and cohesion force. The contact area radius (eq. 3.45) is based on Hertz's theory of elastic contact and can be substituted in the normal repulsive force equation (eq. 3.46) (Grima and Wypych, 2011). The Hertz-Mindlin model is only applied once the linear cohesion model has calculated the cohesion forces. The Hertz-Mindlin then begins calculating the overall normal force acting on the particle by adding the linear cohesion forces.

$$r^2 = R\Delta n \tag{3.45}$$

$$F_N = \pi r^2 C_e \tag{3.46}$$

where,

r = Contact area radius (m)
F_N = Normal repulsive force (N)
R = Particle radius (m)
Δn = Normal displacement/overlap increment (m)
C_e = Cohesive energy density (J/m^3)

3.3.3.8. Linear Spring

The linear spring contact force model can be substituted for the default Hertz-Mindlin contact model entirely. The model uses the Cundall and Strack (1979) normal force equation for two contacting particles (eq. 3.47); a similar approach can be used for the tangential force. Both the spring stiffness (eq. 3.48) and dashpot coefficient (eq. 3.49) are indirectly defined by the user; the specified physical characteristics are used for this calculation (DEM Solutions®, 2014). The user-defined characteristic velocity is generally recommended to be set at the maximum velocity in the simulation (DEM Solutions®, 2014).

The simulation time step can have an effect on the resulting force since it is usually calculated based on the spring stiffness; the time step should not allow for an excessive particle overlap (DEM Solutions®, 2014). This contact model is partly based on non-physical models and may not obtain an accurate simulation behavior (Boerner, 2011). The spring stiffness and time step values has to be adjusted until reasonable results are observed.

$$F_N = k_{LS}\Delta n + cv_{\Delta n} \tag{3.47}$$

$$k_{LS} = \frac{16}{15} R_{eq}^{1/2} E_{eq} \left(\frac{15 m_{eq} V^2}{16 R_{eq}^{1/2} E_{eq}} \right)^{1/5} \tag{3.48}$$

$$c = \sqrt{\frac{4 m_{eq} k_{LS}}{1 + \left(\frac{\pi}{\ln e} \right)^2}} \tag{3.49}$$

where,

F_N = Normal force (N)
k_{LS} = Linear spring stiffness (N/m)
Δn = Normal displacement/overlap increment (m)
$v_{\Delta n}$ = Overlap velocity (m/s)
c = Dashpot coefficient (N·s/m)
V = Typical impact/characteristic velocity (m/s)
e = Coefficient of restitution (dimensionless)

3.3.3.9. Hysteretic Spring

Opposite to the Hertz-Mindlin and linear spring models, which are elastic contact models, the hysteretic spring model replicates the plastic deformation behaviors for the particles (DEM Solutions®, 2015). In addition to the standard material properties, three parameters need to be set for particle and geometry interactions: damping factor, stiffness factor, and material yield strength. The damping factor accounts for the velocity-dependent damping, which prevents particle vibration from persisting (DEM Solutions®, 2015). The stiffness factor is used in the tangential force calculation and represents the ratio of tangential-to-normal loading stiffness (DEM Solutions®, 2015). The normal and tangential dampening forces are determined using equations 3.50 and 3.51 respectively (DEM Solutions®, 2014). In addition, the hysteretic spring contact model uses the coefficient of restitution differently from the Hertz-Mindlin contact model. The coefficient of restitution uses a different energy dissipation and recovery method during loading and unloading scenarios respectively (DEM Solutions®, 2015).

$$F_{ND} = -b_N \sqrt{\frac{4m_{eq}(K_1 \; or \; K_2)}{1 + \left(\frac{\pi}{\ln e}\right)^2}} v_{Nrel} \tag{3.50}$$

$$F_{SD} = \sqrt{\frac{4m_{eq}\gamma_t(K_1 \; or \; K_2)}{1 + \left(\frac{\pi}{\ln e}\right)^2}} v_{Trel} \tag{3.51}$$

where,

e = Coefficient of restitution (dimensionless)
K_1 = Spring stiffness before plastic deformation (N/m)
K_2 = Spring stiffness after plastic deformation (N/m)
F_{ND} = Normal damping force (N)
F_{SD} = Tangential (shear) damping Force (N)
b_N = Damping factor (dimensionless)
γ_t = Stiffness factor (dimensionless)
v_{Nrel} = Relative normal velocity (m/s)
v_{Trel} = Relative tangential velocity (m/s)

3.3.3.10. Moving Plane

The moving plane model is used to assign an in-plane linear velocity in any direction to a geometry surface (DEM Solutions®, 2014). The physical geometry is not required to physically move within the simulation. For instance, the resulting velocity of particles coming into contact with a horizontal plane (assigned with the moving plane model) will be calculated using the plane velocity. This model is particularly useful when simulating the conveying movement of particles.

3.3.3.11. Particle Body Force

The particle body force interaction option can be used to couple user-defined external forces, external heat sources, and particle factories. This includes coupling options such as velocity fields, heat conduction models, particle substitution factories, and any customized properties that can be combined with the contact models. The plug-ins can be configured to only interact with the particles when certain conditions are met such as specific positions, velocities, forces, etc. (DEM Solutions®, 2014). The particle body force allows the user to incorporate unconventional parameters in the DEM general theory.

3.3.4. Current Application

Since the initial development of the DEM by Cundall in 1971, the application of the DEM has grown exponentially. Cundall's initial purpose with the DEM was to replicate the behavior of rock mechanics, which was then applied to soil mechanics with Strack in 1979 (ICG, 1999a). Given the technological limitation at that time, simulations were limited to 2-dimensions with simple geometries. General advancements in technology and computational power since the 1970's have expanded the application of the DEM to numerous industrial fields. Simulations can now run in 3-dimensions with even larger amounts of particles (over 15 million); the particles can be non-spherical or clusters (Cleary, 2009). Specific industrial fields that utilize these processes can include: agriculture, construction, mining, natural resource extraction, pharmaceuticals, bio-medical, geology, thermodynamics, manufacturing, military, etc.

The future of DEM can anticipate simulations with larger amounts of particles at greater computational speeds while improving the model accuracy. Aoki shows a glimpse of the future by conducting simulations with over 72 million particles on a GPU-based supercomputer using 84 GPUs (2014). This particular simulation was capable of modeling liquid water as a rogue wave colliding with a statue (6 m in height) as seen in Figure 3.23 (Aoki, 2014). The DEM has become an effective tool in technology development and refinement. A validated model can be used to optimize a particular design without having to physically build a testing apparatus. The benefits of simulating industrial processes can result in lower prototyping costs while minimizing time. Ability of understanding and predicting particulate and fluid flows will continue to be an applicable tool in many industries (Cleary, 2009).

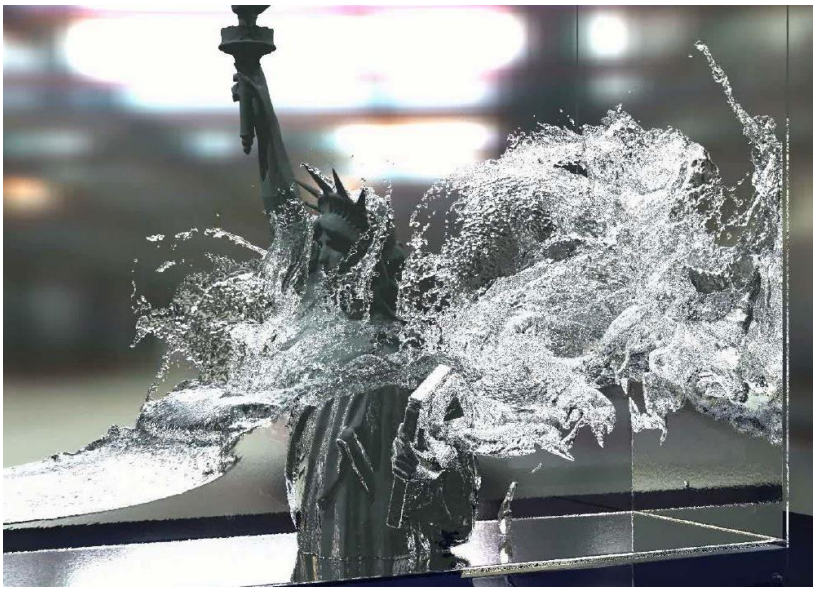

Figure 3.23. DEM simulation of a rogue wave colliding with a statue- 72 million particles with 80 GPUs (Aoki, 2014).

3.4. Summary

The effects of terroir factors such as climate, grape variety, soil type, and cultural practices on viticulture were discussed. This included presenting the specific regions with the optimal conditions for grape growth.

The introduction and evolution of mechanized grape harvesting in viticulture was presented. A description of the general configuration and functionality of grape harvesters followed. In addition, the cleaning methods and technologies that are commonly integrated in grape harvesters were discussed. Information on current cleaning systems that combine multiple methods of cleaning and sorting was included; specific patents and manufacturers that use these systems were highlighted.

The development of the DEM modeling scale in simulation software was presented. An extensive description of the DEM general theory discusses the application of the force-displacement law and Newton's second law of motion. The required physical properties of the geometry and particle materials for the DEM calculations were also outlined. The contact models that are specifically used with the project's DEM software package (EDEM® version 2.7) were explained in detail with general equations. Examples of current industrial applications of the DEM were also provided.

Research information pertaining to the application of the DEM for the optimizing agricultural practices was found. In particular, the de-stemming process of grape clusters was modeled using the DEM (Coetzee and Lombard, 2013). Despite this, no research related to the DEM modeling of the pneumatic cleaning process (removal of foreign materials with aspirator) in grape harvesters was found.

4.0 MATERIALS AND METHODS

Property testing for the biological materials was required for the development of the main crop flow simulation. This material initially consisted of grapes, grape stems, leaves, petioles, and vine shoots. Although these tests included the five biological materials, the DEM simulations concentrated on only three: grapes, leaves, and petioles. The grape stems and vine shoots were omitted given the high complexity of the geometrical shapes; the computational efficiency would have been significantly reduced by including the five materials. In general, the cleaning quality of grape harvesters is compromised by the presence of petioles and leaves rather than the grape stems and vine shoots. For this reason, the inclusion of grape stems and vine shoots was deemed outside the scope of the project. Similarly, the contacting surfaces between the biological materials and the cleaning system (conveyor and aspirator) only included stainless steel and rubber; the simulations only required these two materials. The additional materials were incorporated in the crop property tests for potential future developments.

The obtained results from the crop property testing were used in validation simulations for the coefficient of static friction, coefficient of restitution, leaf material flexibility, and conveyor trajectory. Leaf development and validation for the DEM simulations were emphasized in particular. The main crop flow simulation, which incorporated the aspirator and conveyor, was developed using the physical properties and parameters from the previously validated simulations. This final simulation was validated with the grape harvester test bench results. The next section outlines the procedures and equipment used for each physical property test. It also explains the development and validation of the DEM simulations.

4.1. Physical Property Testing

The physical properties outlined in Table 4.1 were necessary in the characterization of biological materials for the DEM simulations. The testing period took place during the 2014 grape harvest season (September-November) in France at three locations: Aigues-Mortes, Saint-Gervais, and Pauillac. The testing procedures followed the applicable ASTM standards mentioned in the respective sections below. Some procedures were adapted from peer-reviewed articles that conducted similar experiments and others were based on CNH Industrial internal standards. Sample collection was fully randomized within different vine research parcels at the respective locations. This was imperative in reducing the potential bias in the collected data. The number of trials was maximized in accordance with the available time and resources; approximately 30 to 90 trials were conducted for each test. The testing procedures for the porosity, separation force, and static angle of repose can also be found in section B.1 of APPENDIX B. These tests were not imperative for the development of the main crop flow simulation, but were conducted for potential future developments based on the project.

Table 4.1. Pertinent physical properties of the cleaning system.

Measured Properties	Calculated Properties
▪ Geometric mean diameter ▪ Thickness ▪ Length ▪ Mass ▪ Static angle of repose ▪ Angle of static friction (ASTM G115-10, 2013) ▪ Bounce height (Hastie, 2013) ▪ Terminal velocity (ASTM D3464-96, 2014) ▪ Separation force and energy (Internal CNH Industrial standard) ▪ Porosity	▪ Sphericity ▪ Particle density ▪ Bulk density ▪ Coefficient of restitution ▪ Coefficient of static friction ▪ Drag coefficient

The experimental design consisted of determining the DEM input properties for the Cabernet Sauvignon grape variety in France. The obtained values were used to create representative averages in ideal harvesting conditions. The R® Version 3.1.2 (Foundation for Statistical Computing, Vienna, AUT) statistical software was used for the project statistical analysis. An analysis of variance (ANOVA) at a 95% confidence interval was used to determine if the locations had a significant effect on the measured property. The Tukey Honest Significant Difference (HSD) post-hoc test was then used to find which location was significantly different from the other. This was done to see if the three populations could be combined as a single dataset for the DEM input properties; a higher number of data points would increase the statistical power and improve the accuracy of the simulations. The Tukey HSD test is essentially used as a multi-level (minimum of three levels) ANOVA t-test, which provides an alternative to running multiple ANOVA tests for each level. Running multiple t-tests with the ANOVA function would increase the probability of a type I error, thus wrongfully stating a significant difference (Crawley, 2013).

Prior to the 2014 grape harvesting season, a test bench for physical property testing was developed and built (Figure 4.1). This bench was designed to be portable and durable while testing in several different locations in France. Before the construction of the test bench, an initial research was conducted to identify the most effective methods of determining the physical properties of the biological materials. These methods were based on ASTM standards and peer reviewed experiments (referenced in the respective sections below). The test bench incorporated an accumulation bin (angle of repose), a rebound surface with a high-speed camera (coefficient of restitution), a conical wind column (drag coefficient), and a tilting platform (coefficient of

friction). Portable measuring devices (caliper, scale, force gauge, etc.) were also used to determine the remaining properties (average diameter, mass, separation force, etc.).

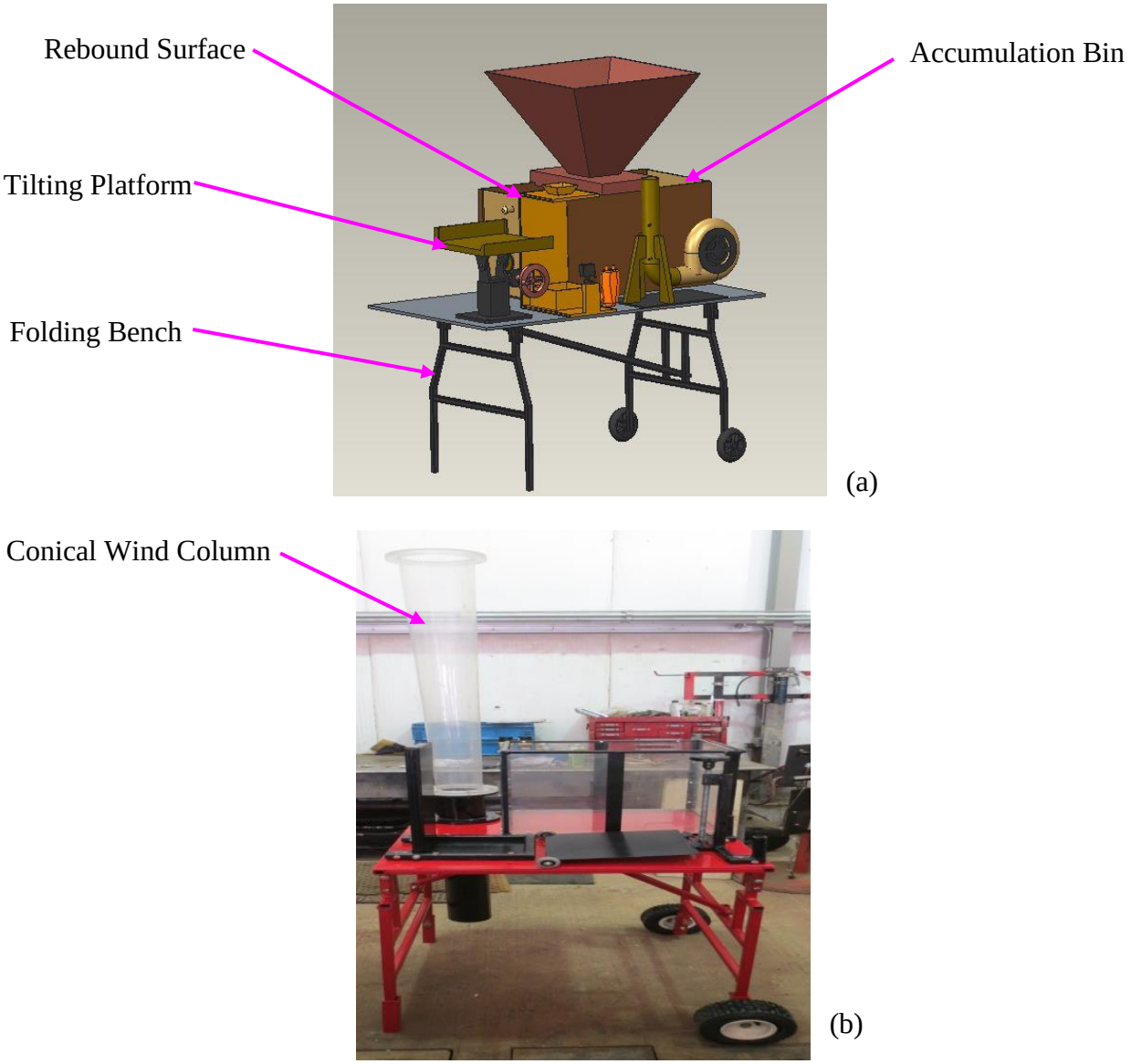

Figure 4.1.Test bench used to determine the physical properties of the biological materials. (a) Designed 3D CAD model. (b) Fabricated test bench.

4.1.1. Geometrical and Mass Measurements

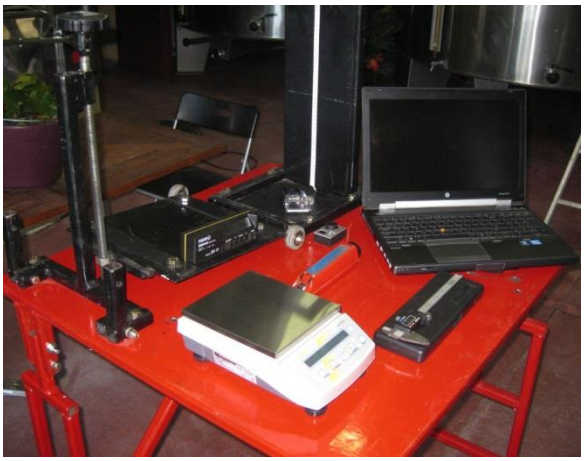

Figure 4.2. Test bench equipped with instruments used for measuring the physical properties.

The geometrical and mass measurements were necessary for determining the physical shapes and densities of the biological materials. Mass measurements were taken using a digital scale (KERN CKE 2000-2, Balingen, Germany). A digital caliper (Fischer Darex, Chambon-Feugerolles, France) was also used to measure diameters, lengths, and thicknesses. The small, medium, and large diameters of grapes were measured in order to calculate the average diameter, sphericity, and volume. By using the grape mass and the calculated volume, true density (wet matter) was calculated. Leaf mass was measured along with three thickness points. Each leaf was then placed on a grid pattern and photographed (Figure 4.3). The pictures were then uploaded to a 3D CAD software (SolidWorks® Version 2013, Massachusetts, USA) to trace out the leaf contour (Figure 4.4), which allowed for the determination of the leaf area. This was used to calculate the true density (wet matter) of the leaf. After being individually weighed, the diameters and lengths of the petioles were measured, thus enabling the calculation of the true density (wet matter). Vine shoot samples were measured the same way as the petioles to

calculate the true density (wet matter). A list of equations used to calculate the different properties can be found in the section A.1 of APPENDIX A.

Figure 4.3. Photographed Cabernet Sauvignon leaf on grid pattern with reference ruler.

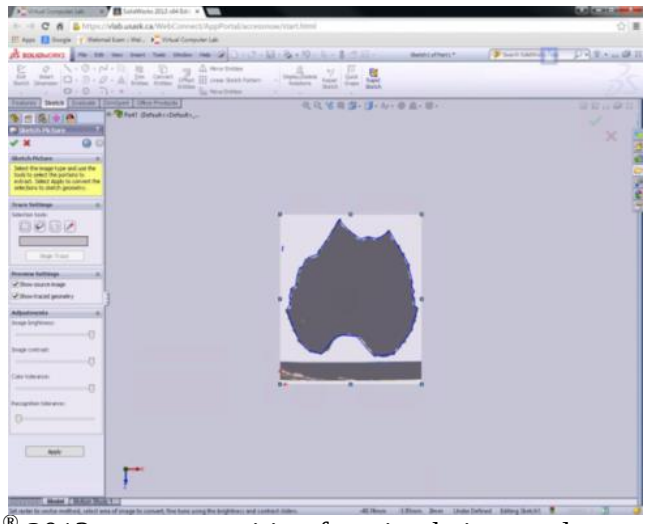

Figure 4.4. SolidWorks® 2013 auto-recognition function being used to approximate photographed leaf perimeter and area.

4.1.2. Coefficient of Static Friction

The coefficient of static friction measurement was used as a physical property and a validation test for the DEM simulations. The experimental procedure to find the coefficient of static friction was based on the G115-10 ASTM standard (ASTM, 2013). Each biological material was individually placed on a variable inclined plane. This plane initiated the rotational motion from a horizontal position and was gradually tilted to increase the angle. The material on the plane would begin to slide at a specific angle, which corresponded to the coefficient of static friction between the two contacting surfaces. Figure 4.5 depicts the free-body diagram of the experimental procedure. By summing the forces along the inclined plane direction, the coefficient of static friction equates to the tangent of the plane angle (eq. 4.1).

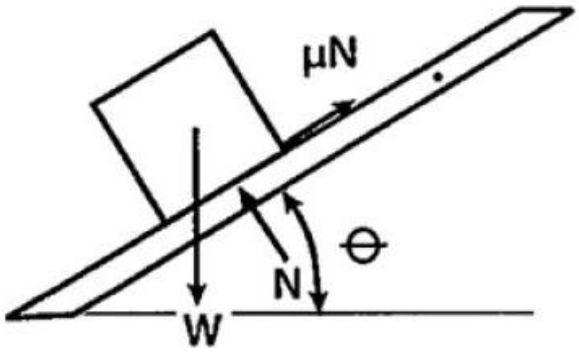

Figure 4.5. Free-body diagram of experimental procedure (ASTM G115-10, 2013).

$$\mu_{static} = \tan \emptyset \tag{4.1}$$

where,

μ_{static} = Coefficient of Static Friction (dimensionless)
ϕ = Angle of Internal Friction (degrees)

The portable test bench used during the 2014 grape harvest season was equipped with a screw-type inclined plane as seen in Figure 4.6. The angle of the plane could be adjusted by turning the screw in either direction. A set of wheels were installed at the end of the plane to provide a smooth support as the angle changed. A digital inclinometer (FISCO Solatronic® EN 17, Rayleigh, UK) provided the angle measurements.

Figure 4.6. Grape bunch and stainless steel surface on inclined plane with digital inclinometer.

The coefficient of static friction was determined for any two contacting surfaces that would normally occur within a grape harvester cleaning system. Depending on the available time, approximately 30 to 60 trials were conducted for each combination. The interactions included contact between the biological materials themselves and with the cleaning system surfaces such as stainless steel (guarding), rubber (conveyor and buckets), and plastic (mesh conveyor). In order to increase the sampling rate, multiple samples were placed on a surface as seen in Figure 4.7. When an individual samples began to slip, the test would momentarily pause

to record the angle measurement on the inclinometer. The test continued until all the samples had slipped.

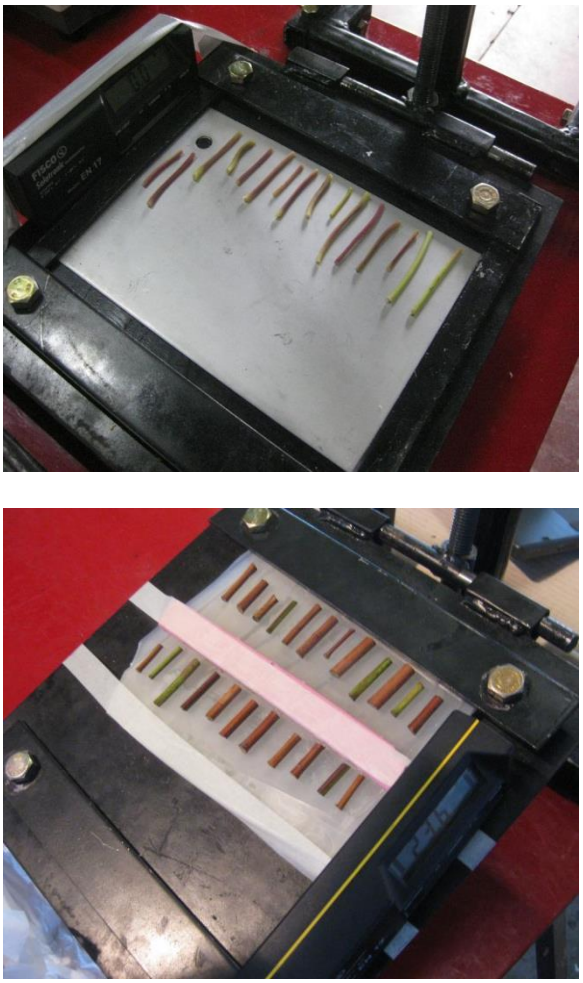

(a)

(b)

Figure 4.7.Coefficient of static friction testing. (a) Petioles on a stainless steel surface. (b) Vine shoots on bucket surface.

4.1.3. Coefficient of Restitution

Similarly to the coefficient of static friction, the coefficient of restitution measurement was also used as a physical property and a method of validation for the DEM simulations. The procedure used to determine the coefficient of restitution was based on the Hastie (2013) experimental method. Figure 4.8 is a schematic of the apparatus used to measure the coefficient of restitution. Individual samples for each biological material were dropped from the release platform and allowed to free-fall until contact occurred with the bounce surface. The bounce height would then be determined using a high–speed camera (GoPro HERO3^{+} BLACK EDITION®, California, USA), which would record the material movement on the grid pattern background at a rate of 240 frames per second (fps). The coefficient of restitution was calculated by means of the drop and bounce height ratio (eq. 4.2).

$$C_R = \sqrt{\frac{h}{H}} \tag{4.2}$$

where,

C_R = Coefficient of restitution (dimensionless)
h = Bounce height (mm)
H = Drop height (mm)

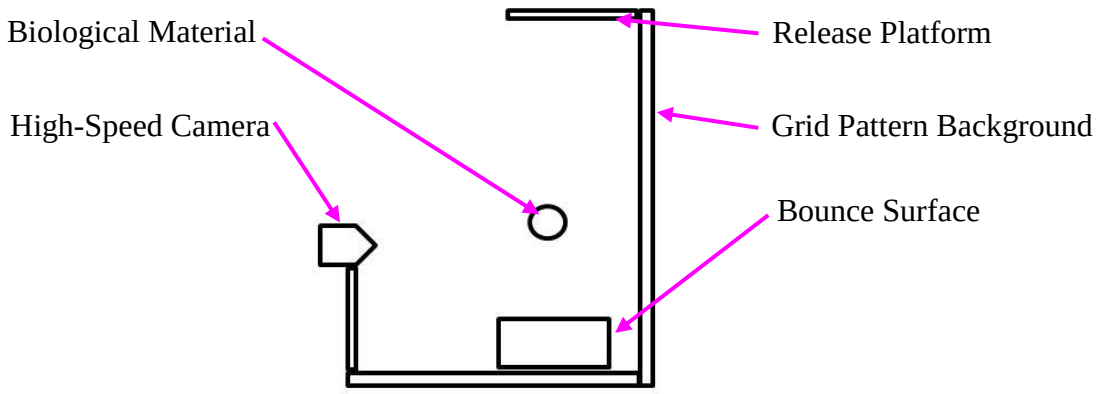

Figure 4.8. Schematic of the apparatus used for the coefficient of restitution.

Approximately 30 to 60 trials for each biological material and surface combination were conducted; the number of trials was limited by the available time at each location. Similar to the coefficient of static friction, the combinations included any two contacting surfaces that would normally interact within a grape harvester cleaning system. Once recorded, the trials would be uploaded and analyzed on the video editing software (GoPro Studio® Version 2.0.1, California, USA). The video speed would be significantly reduced in order to determine the corresponding bounce height of every trial (Figure 4.9). To compensate for the parallax effect (line of sight error) of the camera, distances between the camera, bouncing material (stainless steel, rubber, and plastic), and grid pattern background were measured before each set of trials. The parallax compensation calculations can be found in section A.2 of APPENDIX A.

Figure 4.9. Analysis of bounce height for grapes in high-speed video with stainless steel bounce surface.

4.1.4. Aerodynamic Characteristics

The terminal velocity and drag coefficient of the biological materials were required for the aspirator airflow adjustment process in the main crop flow simulation. These properties were determined by designing and fabricating a separate test bench in France (Figure 4.10). Initially, a centrifugal fan was coupled to a conical wind column, which was installed on the original test bench (Figure 4.1). The airflow was very turbulent and could not provide a steady flow to determine the terminal velocity of the biological materials. A new test bench was therefore developed to minimize the turbulent flow; this incorporated a stabilization box and a valve system. A centrifugal fan provided an airflow (~1900 $m^3 \cdot hr^{-1}$ /1100 CFM) that passed through a hopper and into the stabilization box. The air was then redirected through the directional tube and guided into the linear flow straightener, which was comprised of numerous smaller tubes parallel to the flow. After this, the air could be uniformly diffused into the wind column.

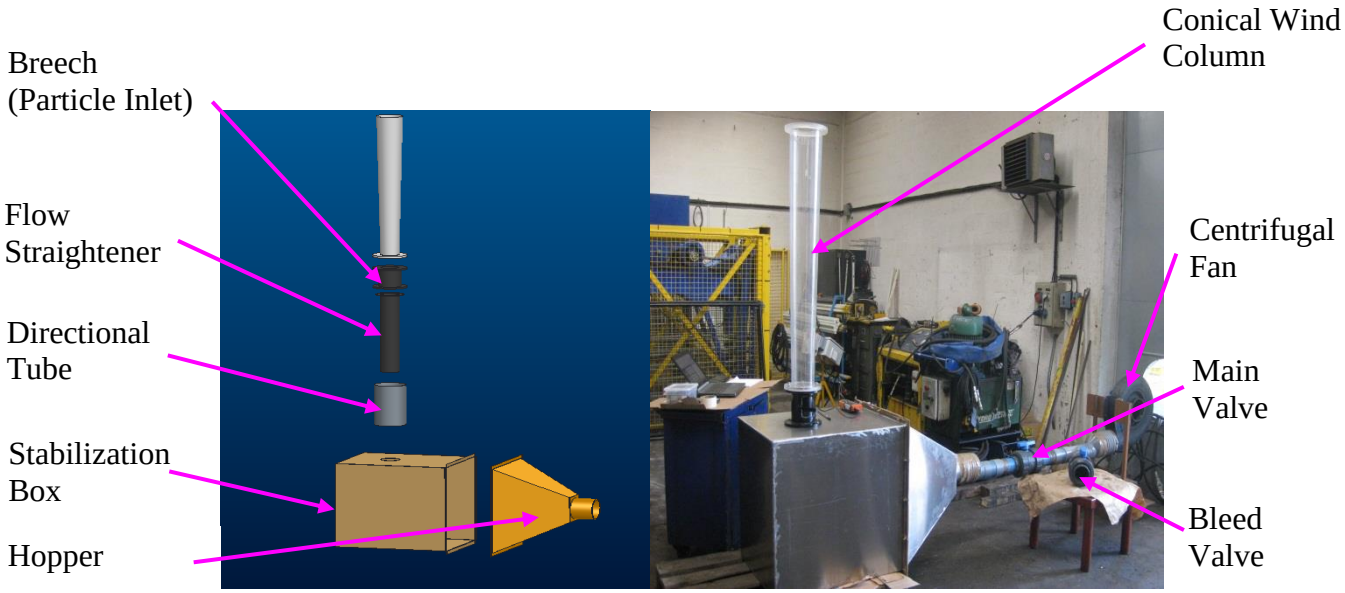

Figure 4.10. Terminal velocity test bench (3D CAD model and actual test bench).

4.1.4.1. Terminal Velocity

Samples were randomly selected from numerous Cabernet Sauvignon parcels at the testing locations. Only two of the testing locations (Aigues-Mortes and Pauillac) could be tested because of labor and time constraints. Given the large size of the terminal velocity test bench, samples were transported to the test bench location (CNH Industrial Plant in Coëx, France). During transport, the samples were sealed and refrigerated until taken out for terminal velocity testing. Afterward, each biological material was manually prepared in a manner that allowed consistent experimental parameters. The petioles were separated from the vine shoots and leaves (

Figure 4.11). Small samples of vine shoots were cut into small cylinders (Figure 4.12). The grapes were also individual picked from random grape bunches to reduce bias. Due to the small diameter of the wind column, small disks (diameter~50 mm) were cut out from individual leaves as displayed in Figure 4.14. The grape stems were omitted from the tests given the geometrical shape complexity. Prior to each individual test, the physical characteristics (mass, diameter, length, etc.) of the samples were recorded to later determine their respective drag coefficients.

Figure 4.11. Petioles used in terminal velocity testing

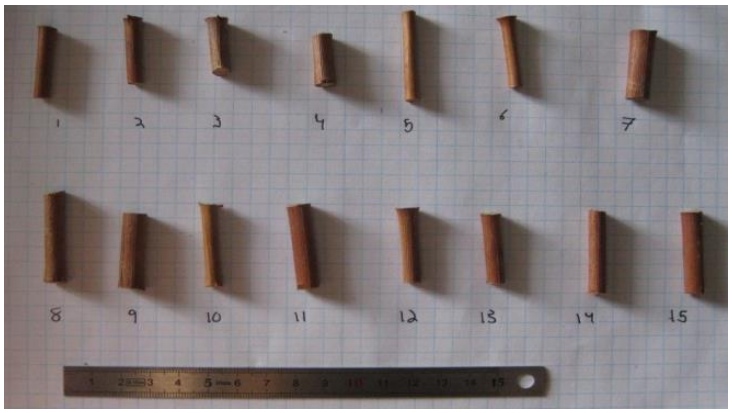

Figure 4.12. Vine shoots used in terminal velocity testing.

Figure 4.13. Grapes used in terminal velocity testing.

Figure 4.14. Leaf disk cut out used in terminal velocity testing.

The conical wind column presents an advantage when testing for the terminal velocity of a particle. The conical nature of the column creates a varying velocity along the entire height. The air velocity decreases as the column height increases. Oppositely, the airflow volume increases as the column height increases. Figure 4.15 depicts a typically observed scenario when testing. By means of similar triangles, the velocity at the sample height was calculated (see section A.3. of APPENDIX A). The inlet velocity at the bottom of the column was measured with a

temperature compensated hot wire anemometer (Extech Instruments® SDL350, Waltham, MA, USA) as per the ASTM D3464-96 standard (ASTM, 2014). As shown in Figure 4.16, incremental measurements along two perpendicular axes were taken at the column inlet cross section. These measurement points were used to establish an average velocity of the cross section. This inlet velocity was then multiplied by the appropriate sample height ratio to obtain the final terminal velocity value of the suspended particle.

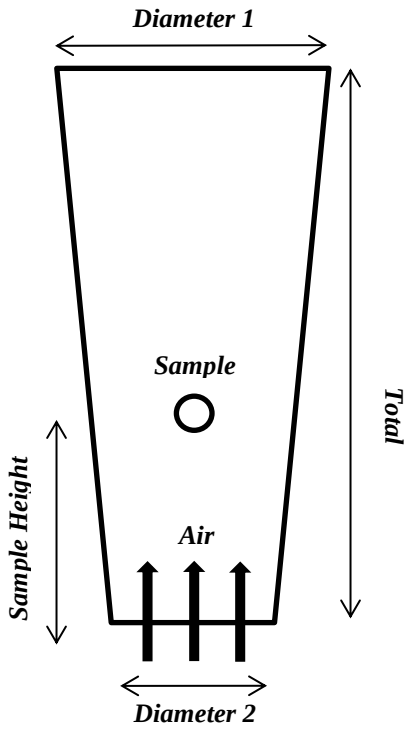

Figure 4.15. Conical wind column schematic for terminal velocity calculation.

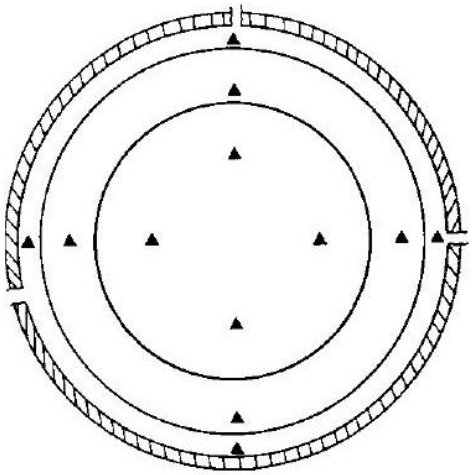

Figure 4.16. Measurement points across cross sectional area (ASTM D3464-96, 2014).

For testing, individual particles were placed into the column by using the breech equipped with a small hatch door. Both the main and air bleeding valves were adjusted until the particle stabilized within the air stream. At this moment, the height of the sample was recorded. In some instances where the air velocity was already set, consecutive samples were placed into the column and then measured with respect to the column height. 30 trials for every material and testing location were conducted.

4.1.4.2. Drag Coefficient Determination

Given the dependency of the terminal velocity on the particle density and projected area, the physical geometry (thickness, diameter, length, etc.) and mass of each sample were recorded. The Mohsenin (1987) drag coefficient analysis simplified the biological material into simpler geometrical shapes such as spheres (grapes), thin disks (leaves), and cylinders (petioles and vine shoots). The airflow direction with respect to the disks and cylinders varied since the samples would often change orientation (normal or parallel to face) and regain equilibrium at an alternate velocity. For the drag coefficient calculations, the airflow direction was assumed to be normal to the disk and cylinder bodies.

The corresponding drag coefficient (eq. 4.3) was determined with the general terminal velocity equation (eq. 4.4), which accounts for the flow regime, the particles projected area, and the meteorological conditions (temperature, humidity, atmospheric pressure, etc.). The meteorological readings were taken from local weather stations near the testing sites. The particle flow regime was also found by using the standard Reynolds number equation (eq. 4.5). Table 4.2 indicates the ranges of Reynolds number that correspond with the laminar, intermediate, and turbulent flow regimes (Mohsenin, 1984).

Table 4.2. Particle flow regime for with respect to Reynolds number (Mohsenin, 1984).

Flow Regime	Laminar Flow	Intermediate Flow	Turbulent Flow
Reynolds Number	$N_R<1$	$2< N_R<1{,}000$	$1{,}000< N_R<200{,}000$

$$C = \left[\frac{2W(\rho_p - \rho_f)}{V_t^2 \rho_p \rho_f A_p}\right] \quad (4.3)$$

$$V_t = \left[\frac{2W(\rho_p - \rho_f)}{\rho_p \rho_f A_p C}\right]^{1/2} \quad (4.4)$$

$$N_R = \frac{\rho_f V_t D}{\eta} \quad (4.5)$$

where,

C = Drag coefficient (dimensionless)
V_t = Terminal velocity (m/s)
N_R = Reynolds number (dimensionless)
D = Effective dimension (m)
η = Dynamic viscosity or absolute viscosity (kg/m·s or Pa·s)
W = Particle mass (kg)
A_p = Particle projected area (m^2)
d_p = Particle diameter (m)
ρ_f = Fluid density (kg/m^3)
ρ_p= Particle density (kg/m^3)
g = Gravitational acceleration (9.81 m/s^2)

4.2. Physical Property Simulation and Validation

To accurately replicate the behavior of the biological materials, the individual DEM simulations used the results from the experimental tests for the validations. For instance, the coefficients of static friction and restitution were adjusted in the simulations until they coincided with the measured results. A similar process also took place to mimic the leaf behavior. The geometrical shapes of the biological materials were based on the physical measurements taken during the physical property tests. These individual simulations were the precursor for the development of the main crop flow simulation, which combined all the validated properties and characteristics of the biological materials. As previously mentioned, the tests in the following sections have omitted the extra cleaning system materials (bucket rubber and mesh conveyor plastic) and biological materials (grape stem and vine shoot) since they were outside of the project scope.

4.2.1. Simulation Contact Models and Properties

Table 4.3 outlines the selected contact models and particle body forces for the DEM simulations. The default Hertz-Mindlin contact model was chosen based on the simplicity, accuracy, and efficiency in the calculation of forces. No additional parameters are required from the user (i.e. characteristic velocity, damping factor, stiffness factor, etc.) in comparison to other contact models (i.e. hysteretic spring and linear spring). It can also be compatible with other models, which provides more options and flexibility when simulating complex processes.

Table 4.3. Contact models and particle body forces used for the DEM simulations

Simulation Modeling Parameters

• Contact Models
  ○ Hertz-Mindlin (no slip)
  ○ Linear Cohesion
  ○ Moving Plane
• Particle Body Force
  ○ Custom Bendable Particle and Factory
  ○ Velocity Vector Field

To account for the adhesion and cohesion effects, the linear cohesion model was incorporated in addition to the Hertz-Mindlin model. An advantage for the linear cohesion model is that it can incorporate a multitude of other contact models such as the hysteretic spring or the Hertz-Mindlin. The linear cohesion model was selected over the JKR cohesion in the event that the Hertz-Mindlin model was substituted for another; the linear contact model offered more flexibility and compatibility with other models. In addition, the JKR model was also initially designed for fine and dry particles, whereas the linear cohesion was a more generalized model (EDEM, 2014). Although the cohesion models have slight variances with the frictional force calculations, both models can offer accurate results.

The moving plane model was implemented for the conveyor surface within the simulation. This model significantly reduced the complexity of the simulation by allowing the use of a stationary plane for the conveyor belt. Alternate conveyor speeds and angles were adjusted accordingly.

The particle body force coupling included a customizable factory capable of creating multiple leaves at any time interval. This coupling was specifically customized to capture the flexibility of a leaf. This approach was selected given the accuracy and automation in the simulation. It was also particularly useful when adjusting the flexibility and rigidity parameters in the validation phase of the simulations. In addition, a separate particle body force included a velocity vector field, which replicated the airflow from the aspirator. An equivalent force due to the airflow was applied to the particles in the simulation. This feature bridged the computational fluid dynamics (CFD) analysis of the aspirator (conducted by CNH Industrial) with the DEM simulations.

Table 4.4 displays the physical properties used in the DEM simulations that were not measured during the 2014 grape harvest season. The determination of these particular properties required specialized equipment that was not readily available or portable; this was outside of the project scope. For that reason, the remaining physical properties for the DEM simulations were found using peer reviewed sources as described in the table below. The stainless steel and conveyor rubber properties were made available by the grape harvester team in France (CNH Industrial).

Table 4.4. Physical properties used in the DEM simulations that were not measured.

Material	Input Physical Property			
	Poisson's Ratio (dimensionless)	Shear Modulus (MPa)	Density (kg/m^3)	Young's Modulus (MPa)
Stainless Steel	0.275	84000	8100	210000
Conveyor Rubber (Polyvinylchloride - tpPVC)	0.407	1490	1580	4140
Grape	0.35[a]	0.30[a]	[*]	0.81[b]
Leaf	0.34[c]	3.70[d]	[*]	9.92[d]
Petiole	0.30[e]	108.98[g]	[*]	283.34[f]

[*] Represents the values measured during the 2014 grape harvesting season in France. [a] Value taken from Coetzee and Lombard (2013). [b] Calculated using equation 4.7, v=0.35 (Coetzee and Lombard, 2013), and G=0.3 MPa (Coetzee and Lombard, 2013). [c] Taken from Farinas *et al*. (2013). [d] Calculated using equation 4.6, equation 4.7, v=0.34 (Farinas *et al*., 2013), and K=10.33 MPa (Alsina *et al*., 2007). [e] Taken from Faisal *et al*. (2010). [f] Taken from Caliaro *et al*. (2013). [g] Calculated using equation 4.7 and E= 283.34 MPa (Caliaro *et al*., 2013).

$$E = 3K(1 - 2v) \tag{4.6}$$

$$G = \frac{E}{2(1 + v)} \tag{4.7}$$

where,

G = Shear modulus (Pa)
K = Bulk modulus (Pa)
ν = Poisson's ratio (dimensionless)
E = Young's modulus (Pa)

4.2.2. Inclined Plane Simulation

The coefficient of static friction was determined between the selected biological materials (grapes, petioles, and leaves) themselves and with the equipment surfaces (stainless steel and rubber). The DEM simulations recreated the same experimental configurations as the tests. A plane with the corresponding material properties was used to find the maximum angle at which the biological materials began to slip. The slipping point for the biological material was extracted using the simulation analyst tool; the angle was determined using the particle and inclined plane positions with respect to the horizontal plane. This information was exported for each saved time interval (~0.01 s). As previously mentioned, the tangent of these friction angles corresponds to the coefficient of static friction (eq. 4.1), which is independent of mass and contact area.

The samples used in the DEM simulations were configured to resemble the ones from the actual experiments. Figure 4.17 displays the grape (a), petiole (b), and leaf (c) samples used in the simulation tests. The grapes were given the average diameter from the previous tests done in France and organized in a cluster of four. The cluster organization was used to prevent rolling on the tilting surface and to ensure a constant contact between the surfaces until reaching the friction angle. The petioles were created using multiple overlapping spheres with diameters equivalent to the measured average from the actual tests. The leaf sample was built into a rectangular grid pattern using single spheres with diameters equivalent to the leaf thickness. During the actual tests, small strips were cut out from the leaves to maximize space on the tilting surface.

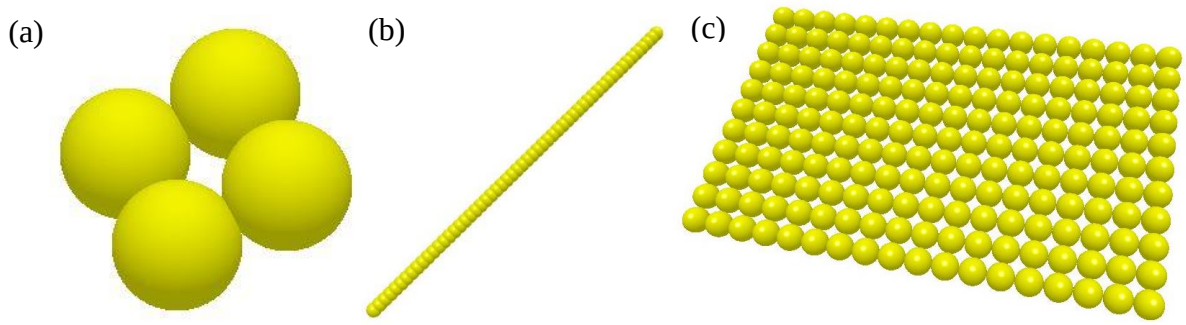

Figure 4.17. Particles generated for the DEM simulation tests. (a) Grape cluster. (b) Single petiole. (c) Leaf sample.

Once created, multiple samples were randomly placed along the rectangular tilting surface (Figure 4.18). After the particles had settled, a slow rotation was applied to the surface. The geometry protractor in the analysis tool was used to dynamically measure the surface angle when samples began slipping (Figure 4.19). This process was repeated for every surface combination until a minimum of 100 samples were measured. The simulation parameters were adjusted for each biological material until the angle was within at least 5% of the actual measured angle. The parameters included both the coefficient of static friction and the energy density for the linear cohesion model with respect to the biological material and surface.

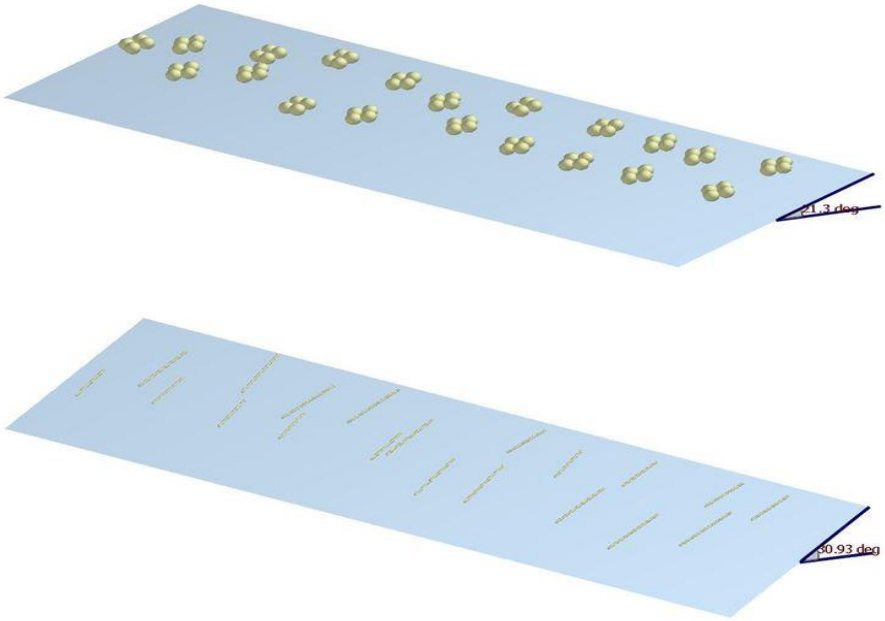

Figure 4.18. Samples positioned along tilting surface. (a) Grape clusters. (b) Individual petioles.

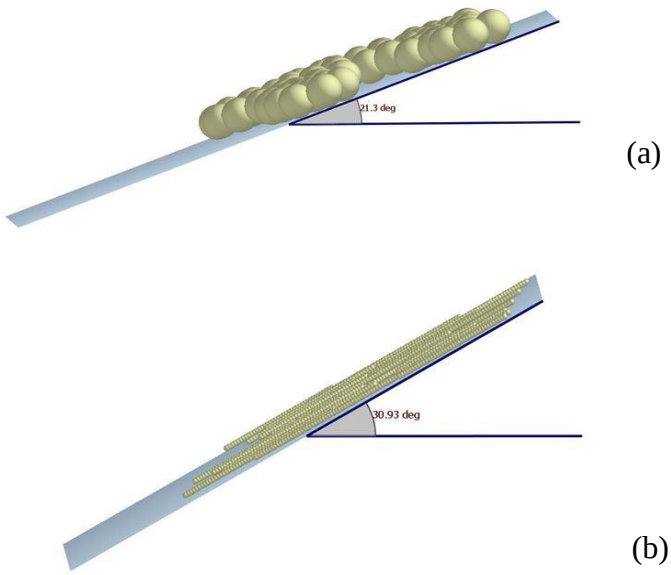

Figure 4.19. The geometry protractor tool used to measure the friction angle. (a) Grape clusters. (b) Individual petioles.

4.2.3. Rebound Surface Simulation

As previously mentioned, the coefficient of restitution is a function of the drop and bounce heights (eq. 4.2) of the particles. A similar testing configuration from the bounce tests conducted in France was recreated in the DEM simulation (Figure 4.20). A test for every biological material interaction (i.e. grape-petiole, grape-rubber, petiole-leaf, etc.) was simulated. Given the large surface area of the leaves, a parachute effect was present when the leaf samples were dropped. For that reason, the leaf bounce height was considered negligible and was not tested or simulated; a low value for the coefficient of restitution was assigned within the DEM simulation.

The grapes were simulated using a single factory with one hundred samples placed at a drop height of 0.5 m over the bounce surface. The surface properties (i.e. density, Poisson's ratio, shear modulus, etc.) were modified until they corresponded with the desired material. The bounce height following the first contact with the surface was measured with the analyst tool; the sample position was exported for every time interval (0.01 s). The coefficient of restitution parameter within the simulation was adjusted until the bounce height corresponded to the value obtained from the physical tests. This calibration was done following the friction calibration to account for the effect of the linear cohesion model.

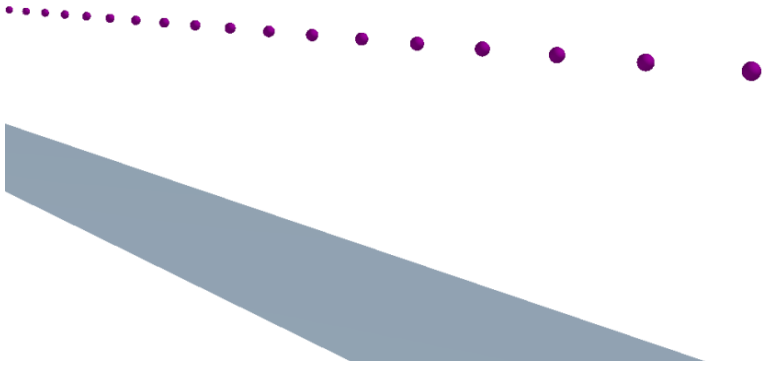

Figure 4.20. Grape particles being dropped from 0.5 m in DEM simulation.

The petioles were simulated using the same method as the grapes (Figure 4.21). However, two simulations for each surface material were required given the effect of the linear cohesion model. An adhesion force to the surface is assigned to each sphere that constitutes the petiole. For that reason, the bounce height of a petiole will vary when it contacts the surface horizontally and vertically. A horizontal impact will have a larger adhesion effect than a vertical impact because of the higher number of spheres contacting the surface. The two simulations included a horizontal and vertical petiole orientation with respect to the surface. The coefficient of restitution parameter was adjusted for both orientations until the bounce height was within 5% of the actual measured value. The final value of the coefficient was obtained by averaging the configuration parameter from both simulations. This method was the most logical solution for replicating the petiole behavior given the effect of the linear cohesion model.

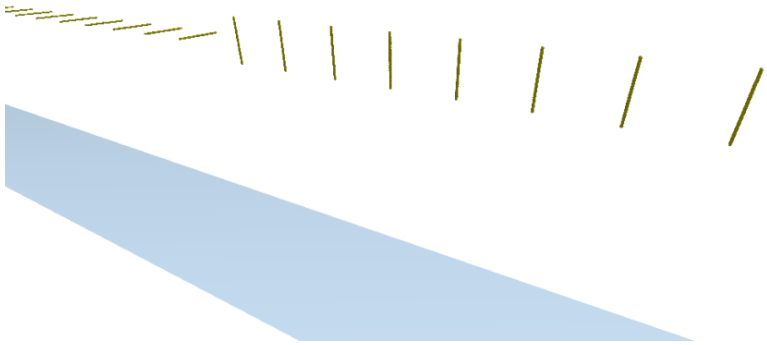

Figure 4.21. Horizontal and vertical petioles being dropped from 0.5 m in DEM simulation.

4.2.4. Leaf Development and Deflection Simulations

Among the biological materials that were incorporated within the main crop flow simulation, leaves were selected for additional testing. This was done to accurately replicate the physical characteristics and behaviour of the leaves during the cleaning process. The flexible nature of the material changes the physical shape and orientation of the leaves when interacting with the cleaning equipment and the other biological materials. The other materials have a greater rigidity than leaves, which allows them to maintain constant physical shape during the cleaning process. For this reason, leaf modeling needed to incorporate the elastic characteristics of the leaf material.

4.2.4.1. Leaf Physical Shape

Pictures taken of individual leaves during the initial testing in France were analyzed using SolidWorks® (2013 version). An auto-recognition function was able to trace the leaf contour as depicted in Figure 4.22. An additional measuring feature provided the exact area within the leaf contour. Using this area and the previously recorded mass and thickness from the tests, the density and centre and gravity were calculated.

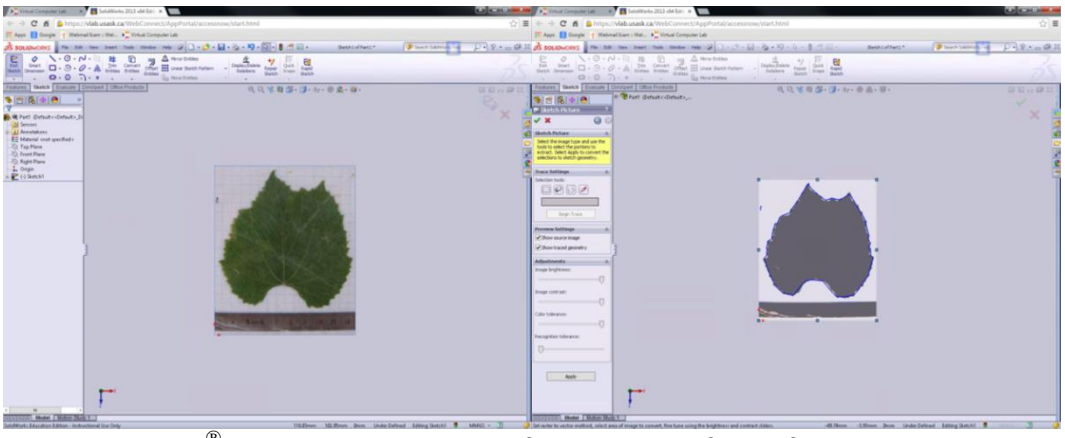

Figure 4.22. SolidWorks® 2013 auto-recognition function used for leaf contouring.

A first attempt at generating a leaf in the DEM simulations began by extruding the two-dimensional contour to the same thickness of the leaf. This provided a three-dimensional object, which could be converted into a stereolithography (.STL) file. This file type converts the object into a shell with the identical surface geometry. The leaf in the .STL file format was then imported into the DEM software and coupled with two particle factories (Figure 4.23). These factories generated particles with diameters equivalent to the leaf thickness. Particles continued to be introduced into the leaf template until it was completely filled. Afterwards, the solid template could be suppressed to allow the free movement of the leaf.

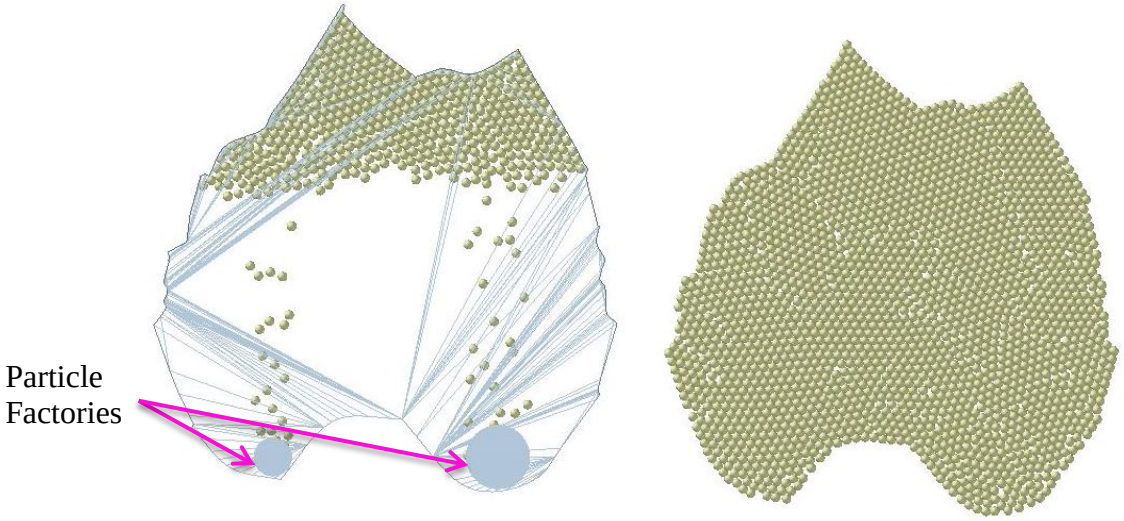

Figure 4.23. Imported STL leaf file in DEM simulation with particle factories dynamically generating particles to fill the leaf-top view.

After suppressing the solid leaf template, the linear cohesion and Hertz-Mindlin with bonding contact models were applied to the leaf particles. The Hertz-Mindlin with bonding was to keep the leaf particles connected while allowing the transfer of force between them. The flexibility of the leaf would be obtained from the bond settings. The linear cohesion was to provide an additional force keeping the particles connected, while adding rigidity to the leaf structure.

Figure 4.24 depicts the randomized positioning of the particles by the generators within the template. Irregularities among the bonds were present due to the non-uniform distances between the particles. Some areas of the leaf contained stronger bonds due to the contacts, which created an inconsistent rigidity throughout the leaf. Particles with insufficient number of bonds would also detach themselves from the rest of the particles. Ultimately, the computational efficiency was significantly reduced and the entire leaf failed to maintain the template leaf shape (Figure 4.25).

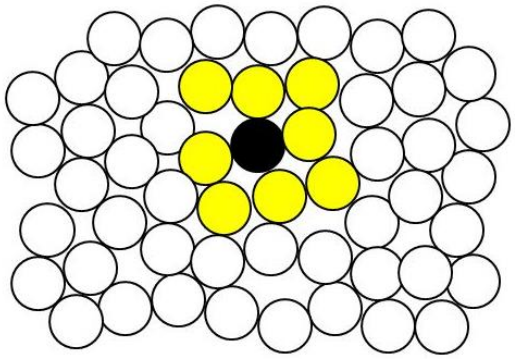

Figure 4.24. Non-uniform particle positioning due to randomized generation. The yellow particles represent all the non-uniform bonds with the black centre particle.

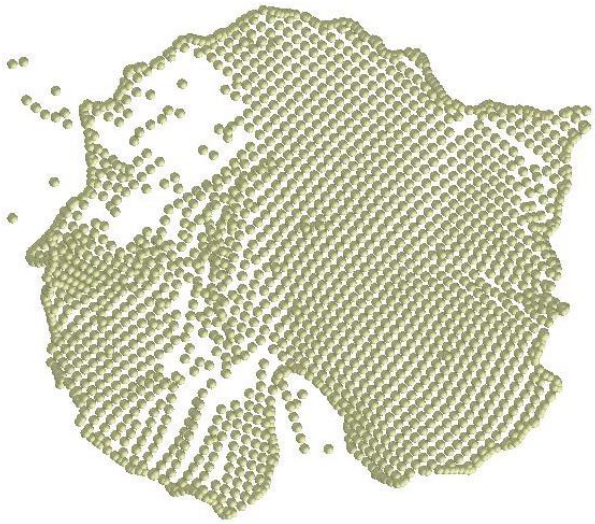

Figure 4.25. Particles placed in non-uniform grid-pattern using coordinates in DEM software.

With the inability to maintain the leaf shape and consistent rigidity, an alternative approach for the leaf generation was developed. Alternatively, particles organized in a uniform grid pattern (Figure 4.26) could provide more consistent bonds; the uniformity would result in identical bond strengths throughout the leaf. The randomized placement of particles created varying distances between particles causing inconsistent bonds.

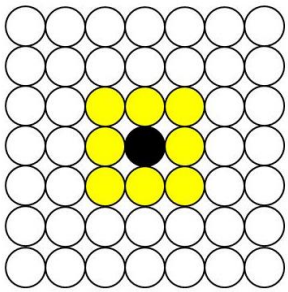

Figure 4.26. Particle positioning in a uniform grid pattern. The yellow particles represent all the uniform bonds with the black centre particle.

To create the uniform grid pattern, the auto-trace function (SolidWorks® 2013) was used to create a parasolid file with the leaf shape. This file was then imported into a second 3D-CAD software (Creo Parametric® 2.0) equipped with a point-filling feature. This was applied to the leaf contour as seen in Figure 4.27; all points were contained inside the contour boundary. The spacing between the points could be adjusted in accordance to the desired particle diameter. The coordinate location of each point was exported as a text file (.TXT). A customized leaf factory that used the exported text file was integrated as a particle body force. Having the coordinates for the particle placement allowed the custom factory to directly substitute a particle for every point (Figure 4.28). This method was advantageous because it allowed multiple consecutive leaves to be generated without any additional manual input. The particle body force also included a

custom bond model to keep the particles together while allowing the leaf to be flexible. The Hertz-Mindlin contact model was kept as the default model for the non-bonding interactions (i.e. leaf contact with geometries and other particles).

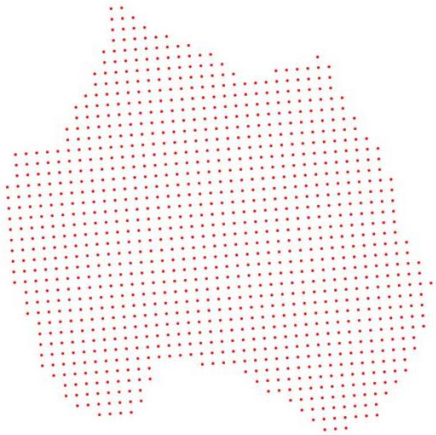

Figure 4.27. Uniform grid pattern positioning using the point filling feature.

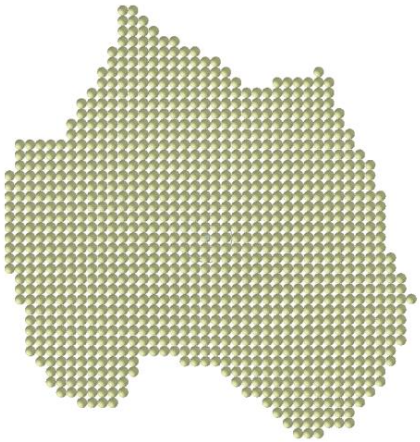

Figure 4.28. Particles placed in uniform grid pattern using coordinates in EDEM®.

4.2.4.2. Material Validation

Two validation tests were conducted to accurately and precisely replicate the leaf behavior in the main crop flow simulation. These included a single deflection test for a rectangular leaf sample and a multi-deflection test for an entire leaf. Both tests used a single sample in five different configurations. The leaves used for this phase of testing were from the Vineland Research and Innovation Centre (VRIC) in Ontario. To maintain consistency between the tests in France and Canada, the leaves were also selected from the Cabernet Sauvignon variety. Three alternate shipments of leaves were sent in boxes with styrofoam insulation and a dry ice pack

(Figure 4.29). Approximately one hundred leaves were picked from a vine parcel and placed in sealed plastic bags before the insulated box. An express courier was then used to ship the leaves the day before testing. These steps were taken to preserve the freshness and physical characteristics of the leaves.

Figure 4.29. Insulated box used to ship leaves.

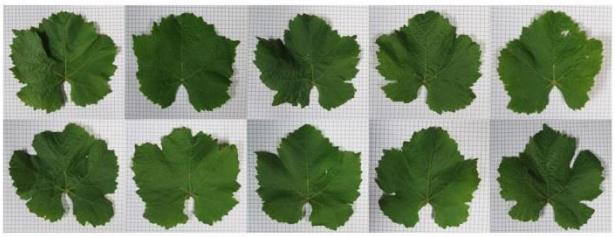

Figure 4.30. Leaves used for testing.

4.2.4.2.1. Single Deflection for Cantilevered Leaf Sample

Several small scale deflection tests were conducted to calibrate the leaf material with the DEM simulation. A sample was cut into a rectangular shape (~20 mm x 45 mm) that was then subjected to five cantilevered controlled deflections. The sample was secured on one the ends with a clamping device, which allowed the opposite end to move freely. The unsupported end was placed above an adjustable bolt (6.35 mm diameter) that created a controlled deflection at five increasing increments (Figure 4.31). These deflections were captured using a high-definition camera (Canon PowerShot® SX40 HS) and a grid background. The obtained pictures were then used to plot a two-dimensional deflection curve.

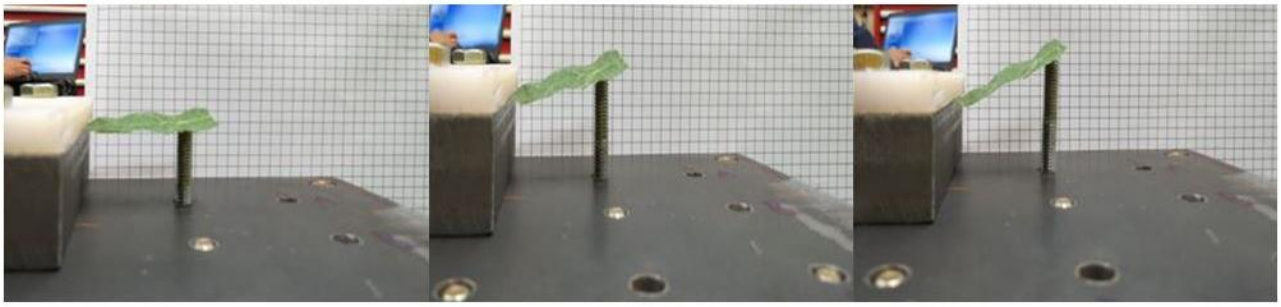

Figure 4.31. Rectangular leaf samples subjected to a controlled deflection.

Identical testing parameters were reproduced within the DEM software by using the particle body force to create the leaf samples (Figure 4.32). The exact placement of the bolt with respect to the sample and the clamping block was the most crucial aspect of the DEM simulation. The bond parameters of the particle body force were adjusted until the modeled samples coincided with the actual tests. The simulated deflection curves were obtained by plotting the particle coordinates of a single row.

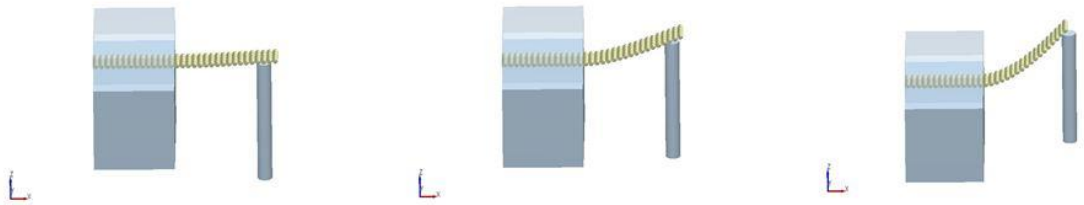

Figure 4.32. DEM leaf samples subjected to a controlled deflection.

The comparison between the simulations and the actual tests was done by plotting the deflection curves on the same graph. A second order polynomial regression was also used to approximate the deflection shape using the plotted points in Microsoft Excel® 2010 (Version 14.0.7015.1000). The basis of comparison between the DEM simulations and the actual tests

consisted of the deflection, angle of deflection, and physical shape of the regression lines. The deflection corresponded to the vertical displacement at the furthest horizontal point of the sample (IEEE CSS, 2005). The angle of deflection was determined by using the first derivative of the obtained regression equation and the vertical displacement at furthest horizontal point (IEEE CSS, 2005). The physical shapes of the deflection were also visually inspected using the plotted curves.

4.2.4.2.2. Multi-Deflections of Leaves

Given the flexible nature of leaves, multiple deflections can occur simultaneously. Accounting for this complex behavior presents challenges in calibrating the leaf model. For this reason, a small scale deflection plate was built. This plate incorporated nine evenly spaced (38 mm apart) adjustable bolts (6.35 mm diameter). Larger corner bolts were used to level the plate on a given surface. To create multiple deflections, a leaf was placed over the centre of the plate where its lower section was secured by a weighted block (Figure 4.33). The centre bolts were then adjusted to lift the leaf at different points to create a varying topography.

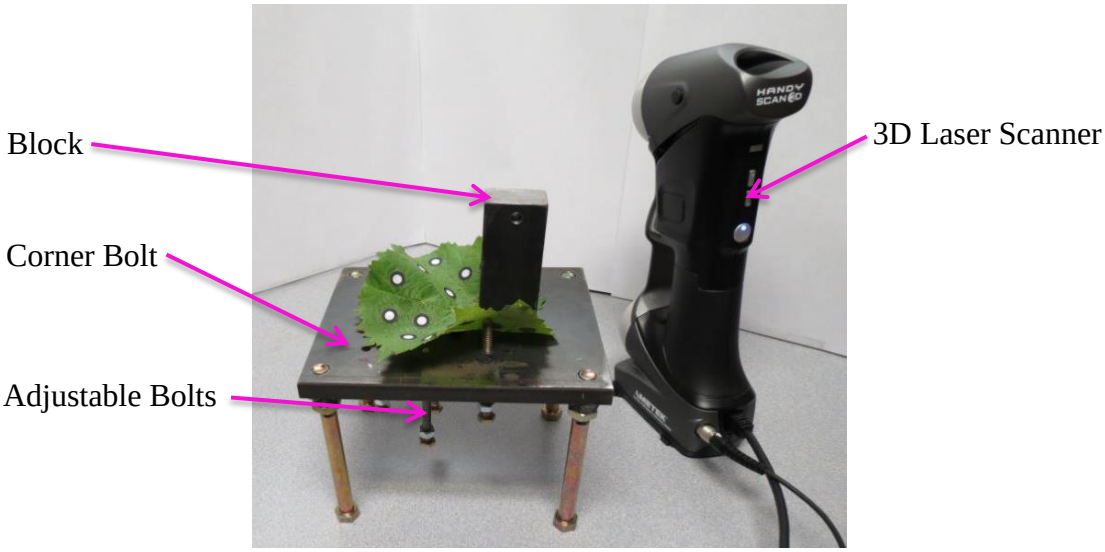

Figure 4.33. Leaf placed on multi-deflection plate next to the 3D scanner.

A total of ten leaves were subjected to five different configurations as described by Figure 4.34 and Table 4.5. Only one leaf was completely analyzed in detail and used in the DEM simulations. This was done to reduce the simulation complexity and to allow more time for the calibration process.

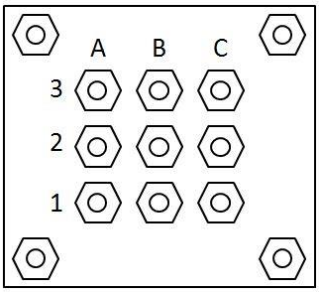

Figure 4.34. Deflection plate schematic-bottom view.

Table 4.5. Deflection plate configurations.

Deflection Plate	
Configuration	Elevated Bolt
1	A2
2	B3
3	B2
4	C1 + C3
5	A2 + B1 +B3

For each deflection configuration, a 3D laser scanner (Creaform® HandySCAN® 700, Québec, Canada) was used to capture the exact surface shape of the leaf (Figure 4.33). This particular 3D scanner was equipped with seven laser crosses and one single line laser resulting in an accuracy of 0.030 mm (0.0012 in) (Creaform®, 2015). Using the scanner editing software (VXelements® 4.0 SR2, Québec, Canada), the scans could be exported as either a point cloud or .STL file. The goal of the tests was to capture the multiple deflections of the leaves in a usable format for the validation process. The .STL file in particular, could be imported in the DEM software and used to compare the actual and modelled leaf deflections. The comparison was done visually by inspecting the general overlay of the .STL file on the simulated leaf (Figure 4.35); the large deviations between the two leaves were identified. In particular, close attention was paid to the leaf edges during the comparison since it was the most significant deviation indicator. The

particle body force parameters were refined in addition to the previous single deflection tests. These adjustments were necessary in finalizing the leaf model for the main crop flow simulation.

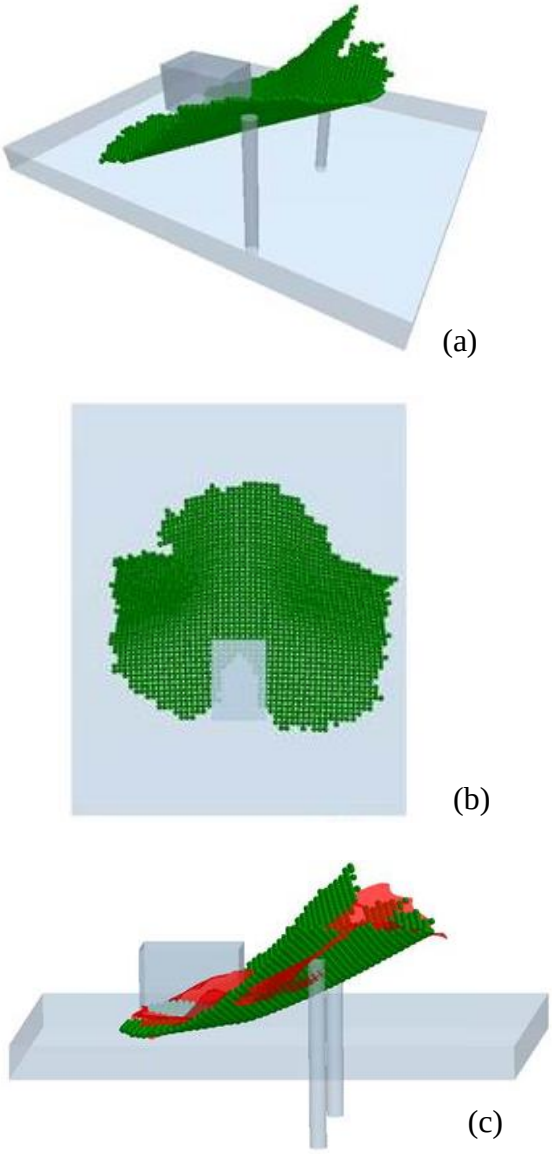

Figure 4.35. DEM Leaf placed on multi-deflection plate. (a) Orthogonal view. (b) Top view. (c) Side view- comparison with overlaying scanned STL leaf.

4.2.5. Grape Trajectory Simulation

This testing phase was conducted in order to compare and validate the behavior of grapes on the conveyor. The previously validated properties from the other simulations (i.e. coefficient of static friction, coefficient of restitution, linear cohesion, etc.) were incorporated. An experimental test was conducted with grape samples from the Aigues-Mortes location in France. An analytical model was also included as a general comparison between the experimental and simulated results. The grape trajectory from the end of the conveyor to the floor was measured for all three tests. The basis of comparison between the DEM simulations, analytical model, and actual tests were the horizontal distance travelled by the grapes (from the end of the conveyor to the landing point on the floor) and the general trajectory path.

4.2.5.1. Experimental Conveyor Test Bench

During the 2014 grape harvest season in France, a separate conveyor test bench was built for the trajectory tests (Figure 4.36). The conveyor was set at an angle of 15^0, which is the angle that is currently being used in the grape harvesters. Three conveyor rotational speeds (at the driving sprocket) were used for the tests: 300 rev/min (1.2 m/s), 400 rev/min (1.6 m/s), and 500 rev/min (2.0 m/s). These alternate speeds were achieved using a 5.5 kW (7.5 HP) alternating current (AC) motor with a variable frequency drive (VFD) (Siemens Sinamics® V20 Package, Munich, Germany). A total of 40 grapes were placed through the introduction gate for each trial. The gate was used to ensure a consistent point of entry for the grapes during the experimental and DEM simulation trials. A high-speed camera (Nikon Coolpix® P100, Tokyo, Japan) was placed just ahead of the conveyor with the lens facing the grid background for an optimized focus. The grape trajectory could be determined by reviewing the slow-motion footage and referencing the

grid background. To account for the camera parallax effect, distances between the camera, projected grapes, and grid background were measured before the trials. The parallax compensation calculations can be found in section A.2 of APPENDIX A.

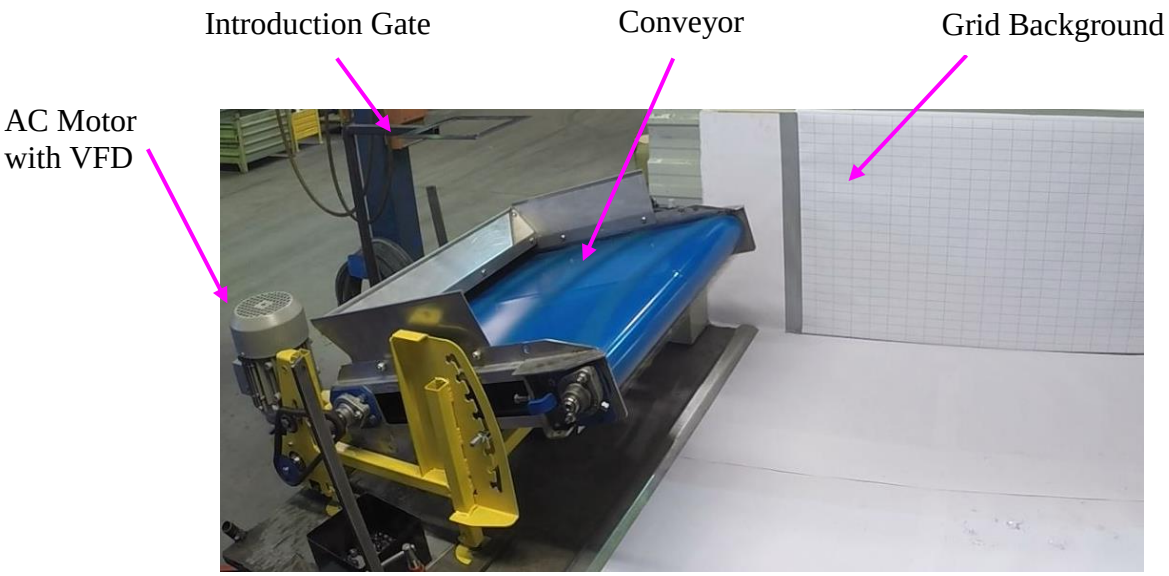

Figure 4.36. Conveyor test bench set at 15^0 for the trajectory tests.

4.2.5.2. DEM Simulation

The CAD model for the conveyor test bench was configured at 15^0 similar to the actual experiment configuration (Figure 4.37). This model could then be imported into the DEM software as a .STL file. Once the test bench was positioned, the conveyor belt was recreated with an angled plane and multiple curved ribs to concentrate the flow in the middle of the belt. By using the moving plane model, the plane was assigned a linear velocity at 15^0 that corresponded with the respective conveyor speeds (Table 4.6). The ribs were also imported from a CAD model and positioned at the bottom of the plane. These ribs were assigned the same linear velocity as the plane; the correct rib spacing was achieved by offsetting the start time for each rib. An

additional rotational movement was assigned to each rib when it reached the end of the conveyor; the rib would rotate about the roller axis. The introduction zone was recreated in the exact same location as the actual experiments. An identical number of grapes (40) were also simultaneously introduced on the conveyor.

Table 4.6. Conveyor test bench velocities.

Rotational Speed (rev/min)	Linear Speed (m/s)
300	1.2
400	1.6
500	2.0

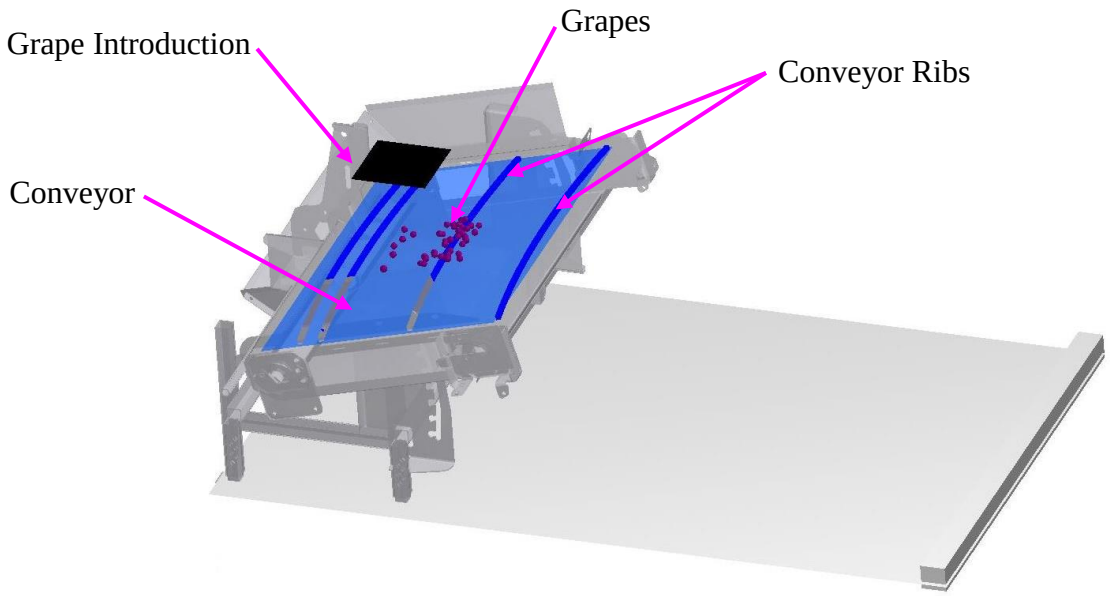

Figure 4.37. Conveyor test bench set at 15^0 in DEM simulation.

The analyst tool of the DEM software allows the user to select specific particles for a multitude of different analysis functions (i.e. velocity, position, contact forces, etc.). In order to capture the trajectory of the grapes from the conveyor, the vertical and horizontal positions were exported for the corresponding time intervals. These data points could then be plotted and compared to experimental and analytical results.

4.2.5.3. Analytical Model

The analytical model was based on the Sitkei (1986) conveying by throwing equations for fertilizer particles. These equations used the laws of inclined throw, which incorporated aerodynamic resistance, to predict the ballistic trajectory of particles. The initial velocity of the particles leaving the conveyor was simplified in the horizontal and vertical components. A force balance for both components accounted for the particle drag force (eq. 4.8); the final equations were integrated with respect to the elapsed time (eqs. 4.9 and 4.10). The trajectory for the three conveyor speeds was plotted using these equations. The complete derivation and simplification of the equations can be found in section A.4 of APPENDIX A.

$$W = \frac{c_w A_p v^2 \rho_a}{2} \tag{4.8}$$

where,

W = Object drag force (N)
c_w = Drag coefficient (dimensionless)
A_p = Particle projected area (m^2)
v = Initial velocity (m/s)
ρ_a = Air density (kg/m^3)

$$x(t) = \frac{m}{K} v \left(1 - e^{\frac{-K}{m}t}\right) \cos\alpha \tag{4.9}$$

$$y(t) = \frac{m}{K}\left(\frac{mg}{K} + v \sin\alpha\right)\left(1 - e^{\frac{-K}{m}t}\right) \cos\alpha - \frac{mg}{K} t \tag{4.10}$$

where,

x = Horizontal displacement (m)
y = Vertical displacement (m)
m = Particle mass (kg)
t = Time (s)
α = Conveyor angle (^{0})
K= Aerodynamic coefficient (kg/m)
g = Gravitational acceleration (9.81 m/s^2)

4.2.6. Main Crop Flow Simulation

The main crop flow simulation was used to optimize the cleaning system performance in terms of crop throughput and product quality. The general behavior of the biological materials (grapes, leaves, and petioles) was also observed. The validation for the simulation was done by comparing the leaf aspiration performance from the grape harvester test bench. The success rate of leaves being aspirated and the minimization of product damage were the evaluation parameters for determining the optimal conveyor configuration.

4.2.6.1. Experimental-Grape Harvester Test Bench

This testing phase replicated the exact cleaning system setup for production grape harvesters (CNH Industrial). As one of the project objectives, the conveyor angles (10°, 15°, and 20°) and speeds (350 rev/min (1.4 m/s), 420 rev/min (1.7 m/s), and 500 rev/min (2.0 m/s)) were tested to optimize the cleaning performance. These tests were also a means of validation for the DEM simulation.

4.2.6.1.1. Conventional Settings-Grape Harvester Cleaning System

In grape harvesters, the main conveyor is set at an angle of approximately 15^0 and at a speed of 400 to 440 rev/min (1.6 to 1.76 m/s). Based on the harvesting conditions, the aspirator is typically adjusted between 1600 and 1800 rev/min for an upward air velocity of approximately 10 m/s for a section of approximately 0.24 m^2. Crop material throughput, grape yield, and humidity levels influence the mechanical settings of the cleaning system. For instance, dry harvesting conditions require lower aspirator speeds as opposed to humid conditions. However, dry conditions increase the bursting susceptibility of grapes; grape juices are exposed and can be

aspirated, which results in product losses. These dry conditions also facilitate the elimination of leaves by the aspirator given the decreased mass. The challenge in correctly setting the cleaning system remains in minimizing both the presence of MOG and the product losses.

4.2.6.1.2. Testing Materials and Parameters

This grape harvester test bench consisted of three principle elements: feeding conveyor, main conveyor, and aspirator (Figure 4.38). All three elements were hydraulically driven and regulated using a tractor hydraulic system (2013 New Holland® T8050). Both the main conveyor and aspirator assemblies were taken from the existing grape harvester cleaning system. Four high-speed cameras (GoPro Hero3+ Black Edition®) were installed throughout the test bench in order to record the leaf behavior in the varying conveyor settings.

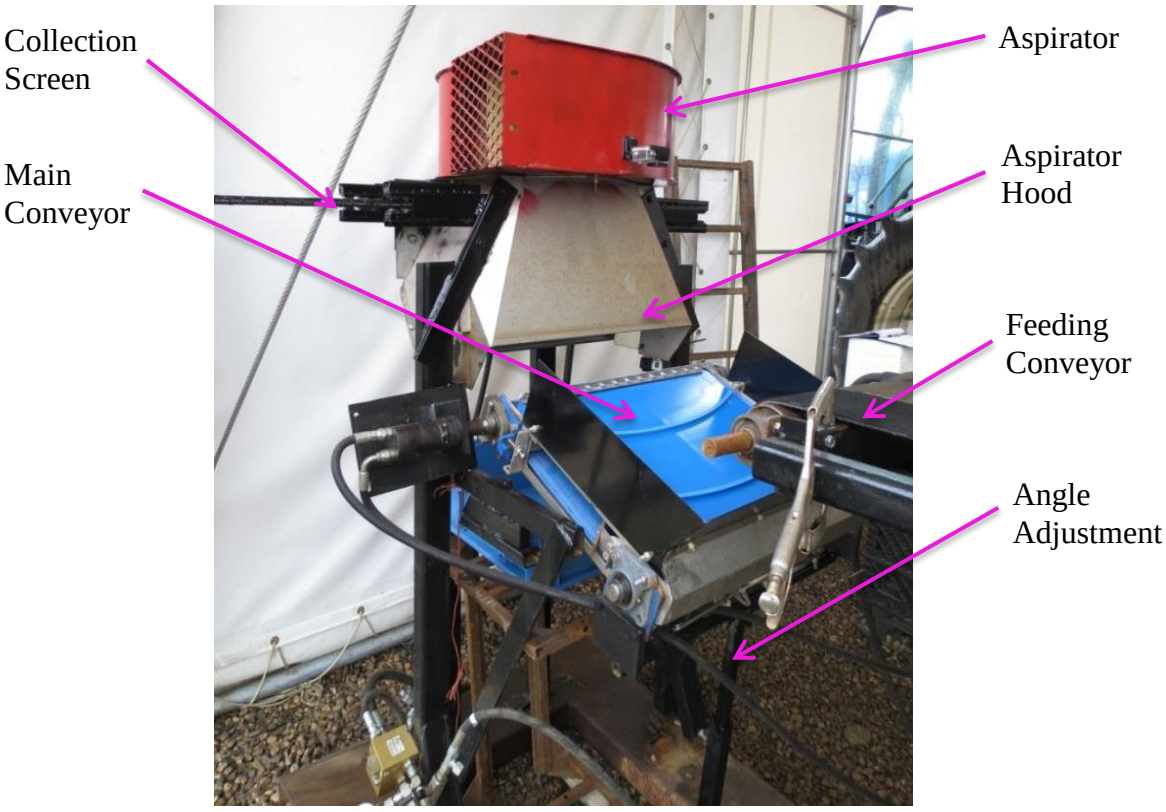

Figure 4.38. Grape harvester test bench with aspirator, adjustable main conveyor, and feeding conveyor.

Table 4.7 shows the main conveyor angles and speeds used during the tests. Each speed was configured for every angle resulting in nine different configurations. The speed was set using a digital tachometer (REED® ST-6236B, North Carolina, USA) directly on one of the conveyor rollers. The angle was adjusted using a digital inclinometer (Mastercraft® 57-4575-4, Ontario, Canada). The aspirator was kept at a constant speed of approximately 1600 rev/min to maintain an upward air velocity of 10 m/s given the relatively dry conditions. The air velocity was measured using a temperature compensated hot wire anemometer (Extech Instruments® SDL350, Massachusetts, USA) as per the ASTM D3464-96 standard (ASTM, 2014).

Table 4.7. Main conveyor settings for grape harvester test bench.

Angle	Rotational Speed (rev/min)	Linear Speed (m/s)
10^0	350	1.4
15^0	420	1.7
20^0	500	2.0

The feeding conveyor was used to uniformly and consistently introduce materials on the main conveyor (Figure 4.39). The length was approximately 4.5 m, which provided room to load materials and sufficient time to attain a constant linear velocity. The feeding conveyor was used for replicating the grape harvester bucket conveyor, which matches the harvester ground speed. With the objective of at least matching the same crop throughput, the feeding conveyor was configured to have a linear velocity of 5 km/h. This speed was adjusted in the same way as the main conveyor by using a digital tachometer (REED® ST-6236B).

Figure 4.39. Feeding conveyor with leaves and artificial grapes positioned in front of grape harvester test bench.

4.2.6.1.3. Biological Materials

The leaves used for these tests were also from the Vineland Research Innovation Centre (VRIC) in the province of Ontario, Canada. A collection screen within the aspirator hood was incorporated to reduce the amount of leaves required for testing. This screen was installed on sets of rollers to prevent the aspirator from plugging. As the leaves accumulated, the screen would move laterally and allow the leaves to fall to the side of the hood. This operation minimized the restriction at the aspirator inlet and maintained a relatively constant airflow. Only two trials were conducted for each configuration because of the fragile state of the leaves. Any additional leaf manipulation would have resulted in non-representative leaf behavior.

Replicating actual harvesting conditions was accomplished by incorporating artificial grape clusters (see section C.2 of APPENDIX C for physical characteristics) with the leaves from Ontario (Figure 4.40). These clusters are often used by the manufacturer to test the cleaning

system and minimize the use of actual grapes. The grape clusters were necessary in keeping the leaves on the feeding conveyor. Due to the rapid acceleration of the feeding conveyor, the leaves had a tendency of being completely thrown off. The leaf-to-grape ratio for the tests was 20 leaves per kg of grapes. This ratio was based on measurements of the materials going into the cleaning system by the grape harvester team in France in actual high yielding plots. To achieve the ratio, the equivalent of approximately 1 kg of artificial grape bunches was matched to 20 leaves being placed on the feeding conveyor.

Figure 4.40. Leaves and artificial grape bunches placed on the feeding conveyor.

4.2.6.2. DEM Simulation

The main crop flow simulation incorporated the aspirator, conveyor, and the three biological materials (grapes, leaves, and petioles). The airflow coupling was integrated within the cleaning system to accurately replicate the aspirator effects. The same nine conveyor configurations as the grape harvester test bench were recreated to validate the simulation while determining the optimal settings. The general behavior of the biological materials and the leaf aspiration performance were evaluated for all the configurations.

4.2.6.2.1. Aspirator and Conveyor Configurations

A computational fluid dynamics (CFD) analysis for the entire grape harvester aspirator assembly was conducted by CNH Industrial. The analysis was based on the same aspirator configuration as the grape harvester test bench and the typical setting used during dry harvesting conditions. The aspirator speed was set at 1600 rev/min, which corresponded to an upward air velocity of approximately 10 m/s within the aspirator hood. The velocity vector field was provided as a text file that could be incorporated within the aspirator using the particle body force coupling (Figure 4.41). This coupling uses the velocity mapping and the shape of the particles to assign a drag force that acts on the particles in all three directions (X, Y, and Z). This mapping uses the inverse distance weighting method to interpolate the particle forces with a pre-defined number of air velocity vectors. The measured terminal velocities and calculated drag coefficients from the testing phase in France were also used to adjust the velocity field. In particular, the drag coefficients were compared to the coupling parameters and adjusted accordingly.

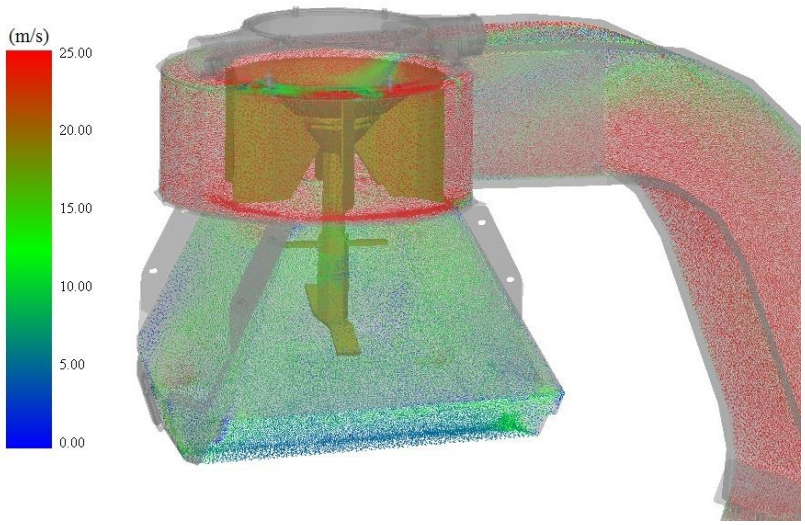

Figure 4.41. Air velocity vector field integrated within the aspirator in the DEM simulation (CNH Industrial).

The aspirator was placed in front and above the conveyor in the same location as production grape harvesters (CNH Industrial). The only modified parameters between simulations were the conveyor angles and speeds. When adjusting the angles, the conveyor was rotated about the conveyor front roller axis in order to maintain an identical distance to the aspirator. The simulation domain was limited partway through the aspirator hood to reduce the redundant calculations and increase the computational efficiency; a larger domain significantly increases the simulation time. The particle behaviour through the entire aspirator system was outside the scope of the project.

The generator that introduced particles into the simulation was configured identically to a grape harvester (Figure 4.42). This generator was placed in the in same location as the conveyor deflector, which helps distribute the biological material across the entire width of the conveyor (Figure 4.43). These new particles were also given an initial velocity (~0.753 m/s) and direction

that corresponded to the emptying characteristics observed in an actual grape harvester. These values were determined using the deflector CAD model and the material slow-motion footage. The generator created the particles at a specified rate while randomly positioning them within the box with the assigned velocity. The random positioning ensured that the particles were evenly dispersed across the conveyor width.

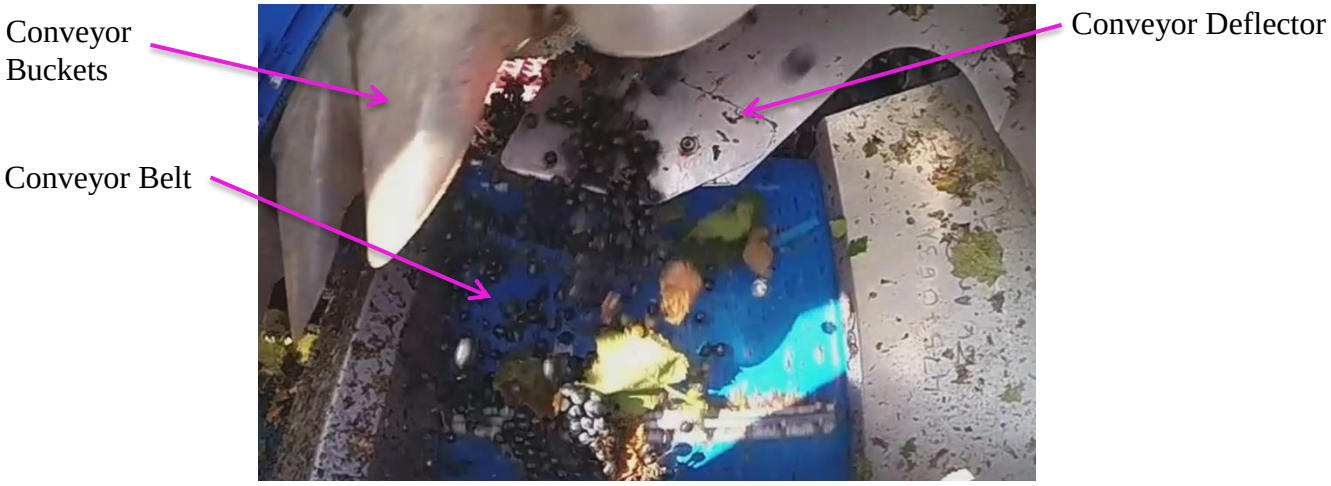

Figure 4.42. Material being propelled in airstream by main conveyor equipped with deflector.

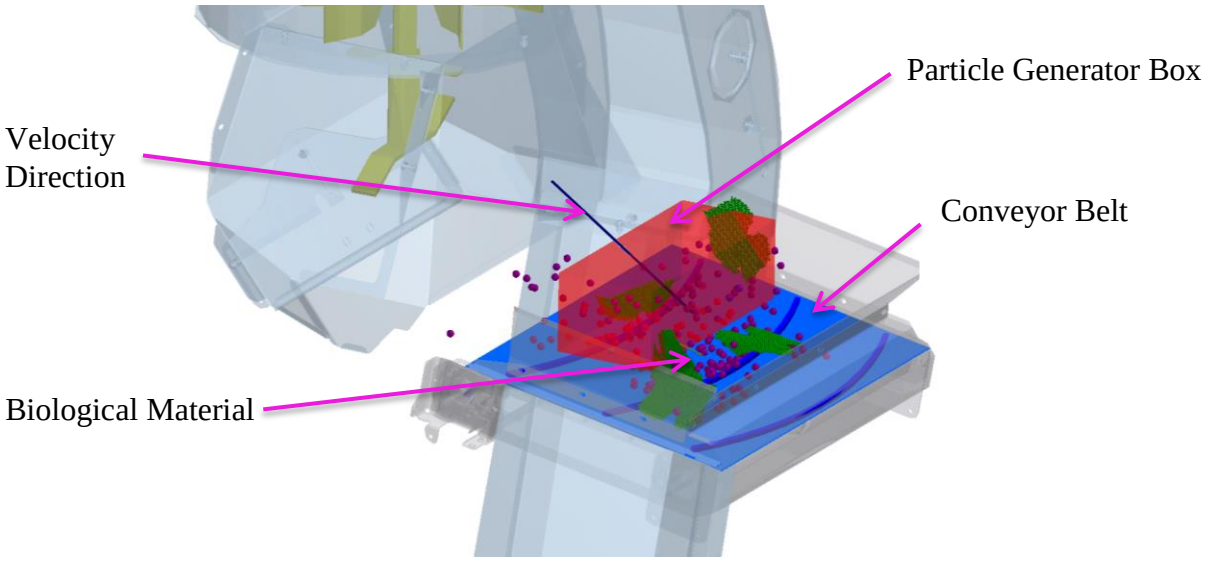

Figure 4.43. DEM simulation model of aspirator and conveyor with displayed particle generator and velocity direction assigned to particles.

4.2.6.2.2. DEM Biological Materials

As discussed, the three biological materials were limited to grapes, petioles, and leaves for the main crop flow simulations (Figure 4.44). Identical grape particles were used throughout these simulations given the small variability observed during the testing phase in France. Contrarily, two sets of petiole particles were used because of the large variability in the length and mass. Although the leaves were among the most variable materials in terms of size and shape, a single leaf was used for the main simulation (the same leaf from the multi-deflection test). This was done to increase the accuracy of the leaf behavior; it was deemed more appropriate to have a single accurate leaf than multiple less accurate leaves.

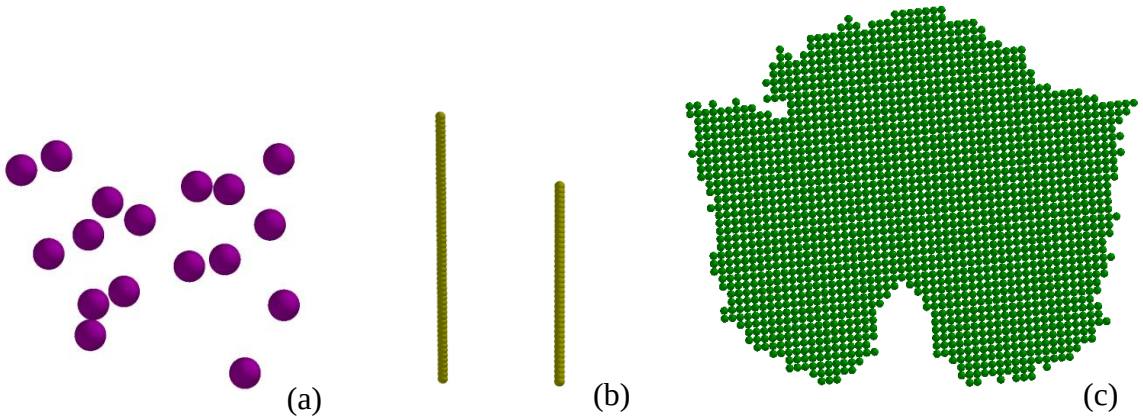

Figure 4.44. Biological materials recreated in DEM simulation. (a) Grapes. (b) Petioles. (c) Leaf.

The generation rates of three biological materials conformed to the grape harvester engineering team measurements (CNH Industrial) in high yielding conditions. Approximately 655 grapes/s, 18 leaves/s, and 10 petioles/s were dynamically created within the generator box at the initial velocity described above. These rates were applied for 2 seconds for all nine conveyor configurations.

5.0 RESULTS AND DISCUSSION

This section includes the statistical analysis for the population comparison, the summarized results for the DEM simulation inputs, the validation comparison between the experimental and simulated results, and the results from the main crop flow simulations. The population comparison included all five biological materials to maximize the samples space for the statistical analysis. The physical properties used in the DEM simulations included only the three biological materials (grapes, leaves, and petioles) and the two cleaning system materials (stainless steel and rubber). The results for the inclined plane, rebound surface, leaf deflections, and grape trajectory simulations are discussed and compared to the experimental tests for the validation process. The main crop flow simulation compares the leaf aspiration success rates to the experimental results from the grape harvester test bench. An optimal conveyor configuration is recommended based on the overall performance.

5.1. Physical Property Testing

This section includes the statistical analysis of the physical property results from the 2014 grape harvest season in France. For each measured property, all three populations (Aigues-Mortes, Pauillac, and Saint-Gervais) were compared with one another to see if they are significantly different. In addition, the actual values of the properties selected for the DEM simulations are presented in tables with the mean, standard deviation, coefficient of variation, and number of samples.

5.1.1. Statistical Analysis

Prior to conducting an ANOVA analysis, the population distribution patterns of the physical property results were analyzed to identify any potential discrepancies. In general, it could be assumed that the population datasets had a normal distribution, homogeneity of variance, and independence between the data points. Even with a skewed data set, an ANOVA test can be used since it is fairly robust with the violated assumption of a normal distribution. In addition, the Tukey HSD function is able to adjust for mildly unbalanced designs (Crawley, 2013). The most important outputs from the tests are the p-values. Anything below 0.05 (5% significance level) rejects the null hypothesis, thus indicating a significant difference between the two compared populations.

5.1.1.1. Population Comparison

The Tukey HSD tests were conducted for all the measurements of the biological materials. Given the time and resource constraints during the 2014 grape harvesting season, the measurements could not be taken at all three locations. For that matter, some comparison levels were not available during the Tukey tests. Despite this, the Tukey test still provided the same p-value as a two-way ANOVA test.

The following tables are the summarized results from the ANOVA and Tukey HSD tests for all the measurements; the p-values for each population comparison are displayed. The first row of the tables shows the three possible population interactions between the Aigues-Mortes (AIG_MRT), Saint-Gervais (ST_GEV), and Pauillac (PIC) locations. The p-values that are below 0.05 are accompanied with an asterisk symbol, which indicates that the two populations are significantly different from one another. Oppositely, the p-values that are above 0.05 indicate

that the two populations are not significantly different. The detailed information on the numerical results for the same analysis can be found in section C.1 of APPENDIX C. The unavailable measurements prevented a complete population comparison between the locations; unavailable data sets are indicated within the tables (Na).

Table 5.1 represents the ANOVA and Tukey tests for the physical characteristics of the biological materials. The grape stem material was not measured given its complex shape. The Aigues-Mortes and Saint-Gervais populations were all significantly different from each other. With the exception of the leaf mass, all the physical properties were significantly different for the Aigues-Mortes-Pauillac interaction. The Saint-Gervais-Pauillac interaction had an assortment of significantly and non-significantly different populations with respect to the biological materials and properties. These irregular results attest to the variability between the populations. The higher number of non-significantly different properties between the Saint-Gervais and Pauillac populations could be attributed to the close proximity of the two locations; similar terroir conditions may have been contributing factors.

Table 5.1. Analysis of variance (ANOVA and Tukey HSD tests) for the physical properties of biological materials.

Physical Characteristics	AIG_MRT-ST_GEV				AIG_MRT-PIC				ST_GEV-PIC			
Mass (g)	0*	2.00E-7*	Na		0*	0.383	Na		0.209	5.26E-5*	0.154	
Sphericity (%)	0*				4.50E-6*				0.426			
Average Diameter (mm)	0*		5.37E-4*	2.00E-7*	1.47E-5*		0.378	0*	0.009*		0.041*	0.984
True Density (kg WM/m^3)	8.70E-6*		Na	7.00E-7*	0*		Na	0*	1.00E-7*		7.57E-4*	0.019*
Length (mm)			0*				4.00E-7*				0.336	
Thickness (mm)		9.13E-4*				1.00E-7*				0.409		
Biological Materials	Grape	Leaf	Petiole	Vine Shoot	Grape	Leaf	Petiole	Vine Shoot	Grape	Leaf	Petiole	Vine Shoot

p-value<0.05: Significantly Different (*)
p-value>0.05: Not Significantly Different
Na: Data Not Available
Blank: Not Applicable

AIG_MRT: Aigues-Mortes
ST_GEV: Saint-Gervais
PIC: Pauillac

The ANOVA of the aerodynamic characteristics is summarized in Table 5.2. This series of tests was only conducted for the Aigues-Mortes and Pauillac locations. With the exception of the disc-shaped leaf material, the terminal velocities and drag coefficients were all significantly different between the locations. Given the small diameter of the vertical wind column, entire leaves could not be tested due to the inevitable contacts with the circular wall. For that reason, uniform leaf discs were tested instead. The uniformity of the samples would explain the non-significantly different properties between the two populations. The variability of the other biological materials can be explained by the significantly different geometrical shapes (i.e. diameter and length) and densities as seen in the previous table. These parameters directly influence both the terminal velocity and drag coefficient (consult equations in section 4.1.4).

Table 5.2. Analysis of variance (ANOVA and Tukey HSD tests) for the aerodynamic properties of biological materials.

Aerodynamic Characteristics	AIG_MRT-PIC			
Terminal Velocity (m/s)	0*	0.323	1.00E-7*	0*
Drag Coefficient (dimensionless)	0*	0.157	0*	0*
Biological Materials	Grape	Leaf (disc shape)	Petiole	Vine Shoot

p-value<0.05: Significantly Different (*)
p-value>0.05: Not Significantly Different
Na: Data Not Available

AIG_MRT: Aigues-Mortes
PIC: Pauillac

The coefficient of restitution values were compared instead of the bounce heights because of a varying experimental parameter. The drop heights for the samples were subject to change due to the inconsistent thicknesses of the bounce surfaces. Because the drop height directly influences the bounce height, the coefficient of restitution was deemed as the more representative comparison parameter between populations. Table 5.3 encompasses all the ANOVA tests for the coefficient of restitution tests. The notation of the interactions is organized by the first material as the object being dropped and the second material (following the "-") as being the bounce surface. A large portion of the Saint-Gervais measurements were not available for a direct comparison with the other Aigues-Mortes and Pauillac populations. From the available data, the interactions with the Saint-Gervais population were mostly significantly different. The Aigues-Mortes-Pauillac comparison had over double the amount of significantly different interactions as non-significantly different interactions. It is difficult to attribute a cause to the variations in the interactions. Having an entire data set for all three locations would have helped to identify any possible relationships.

Table 5.3. Analysis of variance (ANOVA and Tukey HSD tests) for the coefficient of restitution of biological materials.

Coefficient of Restitution			
Interactions	AIG_MRT-ST_GEV	AIG_MRT-PIC	ST_GEV-PIC
Grape-Grape	0*	0*	5.71E-5*
Grape-Stainless Steel	0.700	0.362	0.042*
Grape-Mesh	1.11E-4*	4.01E-5*	0.996
Grape-Bucket	1.30E-6*	1.00E-7*	0*
Grape-Conveyor	3.23E-4*	0.016*	0.601
Grape-Grape Stem	0.019*	Na	Na
Grape-Leaf	6.86E-4*	Na	Na
Grape Stem-Grape	Na	0.167	Na
Shoot-Grape	Na	0.097	Na
Petiole-Grape	Na	0.038*	Na
Grape Stem-Stainless Steel	Na	0.041*	Na
Shoot-Stainless Steel	Na	0.097	Na
Petiole-Stainless Steel	Na	8.62E-4*	Na
Grape Stem-Mesh	Na	6.63E-4*	Na
Shoot-Mesh	Na	0.018*	Na
Petiole-Mesh	Na	0.442	Na
Grape Stem-Bucket	Na	1.48E-4*	Na
Shoot-Bucket	Na	4.01E-5*	Na
Petiole-Bucket	Na	0.887	Na
Grape Stem-Conveyor	Na	0.019*	Na
Shoot-Conveyor	Na	0.0276*	Na
Petiole-Conveyor	Na	0.967	Na
Grape-Shoot	Na	Na	9.60E-3*
Grape-Petiole	Na	Na	0.005*

p-value<0.05: Significantly Different (*)
p-value>0.05: Not Significantly Different
Na: Data Not Available

AIG_MRT: Aigues-Mortes
ST_GEV: Saint-Gervais
PIC: Pauillac

The ANOVA for the angle of static friction is presented in Table 5.4. Similar to the results in Table 5.3, many measurements were not available for the Saint-Gervais location. A direct comparison between the populations was therefore not possible for every measurement. Contrary to the coefficient of restitution experiment, the experimental parameters for the coefficient of friction were constant throughout all the trials. For this reason, the corresponding friction angles were used to compare the different populations. From the available data, the angles between the Saint-Gervais and the other two locations were nearly all non-significantly different. Despite this, the majority of the interactions were not available; therefore a complete and representative comparison could not be completed. When comparing the Aigues-Mortes and Pauillac locations, one half of the interactions is significantly different while the other is not. These results still demonstrate the variability between the populations.

Table 5.4. Analysis of variance (ANOVA and Tukey HSD tests) for the angle of friction of biological materials.

Angle of Static Friction			
Interactions	AIG_MRT-ST_GEV	AIG_MRT-PIC	ST_GEV-PIC
Grape-Leaf	0.516	0.574	0.999
Grape-Petiole	0.090	0.015*	0.627
Grape-Steel	0*	0*	0.006*
Grape-Conveyor	0.887	0.196	0.361
Grape-Grape	0.722	Na	Na
Grape Stem-Grape	0.593	Na	Na
Grape-Vine Shoot	0.741	Na	Na
Grape-Mesh	0.299	Na	Na
Grape-Bucket	0.011*	Na	Na
Grape Stem-Leaf	Na	0.052	Na
Leaf-Leaf	Na	0.581	Na
Petiole-Leaf	Na	0.003*	Na
Grape Stem-Vine Shoot	Na	0.081	Na
Grape Stem-Petiole	Na	0.032*	Na
Vine Shoot-Petiole	Na	3.39E-5*	Na
Petiole-Petiole	Na	0*	Na
Grape Stem-Steel	Na	0.111	Na
Leaf-Steel	Na	0.147	Na
Vine Shoot-Steel	Na	1.01E-4*	Na
Petiole-Steel	Na	0*	Na
Grape Stem-Conveyor	Na	0.002*	Na
Leaf-Conveyor	Na	0.468	Na
Vine Shoot-Conveyor	Na	0.672	Na
Petiole-Conveyor	Na	0.422	Na
Vine Shoot-Leaf	Na	0.709	Na

p-value<0.05: Significantly Different (*)
p-value>0.05: Not Significantly Different
Na: Data Not Available

AIG_MRT: Aigues-Mortes
ST_GEV: Saint-Gervais
PIC: Pauillac

5.1.2. Physical Properties used for DEM Simulations

Based on the summarized results in the tables above, the analysis of variance between location populations was highly variable. For the most part, the interactions were significantly different between populations. The measured properties showed no particular trend or pattern when testing for significance between locations. Having a largely incomplete data set for the Saint-Gervais location also prevented a full comparison between the populations. In general, no two locations had prominent tendencies of being significantly different or not. Despite the close proximity of the Saint-Gervais and Pauillac location, a definitive relationship or non-relationship could not be established. For that reason, the population with the largest number or properties was used to create the DEM simulations: Aigues-Mortes. Missing physical properties were also taken from the Pauillac location (second largest number of properties) in order to have complete data set for the DEM simulations.

As previously mentioned, the simulations were limited to only three biological materials (grapes, petioles, leaves) and two cleaning system materials (conveyor rubber and stainless steel). The complete results for all three locations can be found in section C.1 of APPENDIX C. The remaining properties that were not measured during the 2014 grape harvest season in France were obtained from academic sources as described in section 4.2.1 of the 4.0 MATERIALS AND METHODS. These properties included the Poisson's ratio, shear modulus, and Young's modulus for both the biological and cleaning system materials (stainless steel and rubber); the density for the cleaning system material was also included.

The following tables are the selected physical properties for the DEM simulations, which combines both the Aigues-Mortes and Pauillac locations. They are categorically organized by property or by interaction for the respective materials. The mean, standard deviation, coefficient of variation, test location, and number of trials are indicated for all the properties. The variability in the biological material can be observed throughout the following tables with moderately high coefficients of variation. Despite having a reasonably large sample space, the average coefficient of variation was approximately 20%. This demonstrates the natural variability of the biological material that can be susceptible to its continuously changing environment (i.e. temperature, moisture content, maturity, etc.).

Table 5.5 shows the values of the physical characteristics of the biological materials. Only the petioles properties were taken from the Pauillac location as they were missing from the Aigues-Mortes location. With the exception of its mass, the grape material was the most consistent with lower coefficients of variation than the others. Given the shape and size of leaves, it is not surprising that the leaf mass had a higher coefficient of variation. Despite this, its thickness appears to be reasonably consistent. The lengths of the petioles had a large variation, which would explain the high coefficient of variation for the mass. Based on the location of the leaves, the petiole would often be sized to provide a direct line of sight between the sun and the leaves. The leaves were observed to have longer petioles when located in the centre of the grape vine canopy.

Table 5.5. Physical characteristics of biological materials used for the Discrete-Element Method simulations.

Grape	Mean	Std. Dev.	Coef. of Variation	Location	n
Mass (g)	1.25	0.31	24.5%	AIG_MRT	80
Sphericity (%)	98.0	1.26	1.2%	AIG_MRT	80
Average Diameter (mm)	12.57	0.99	7.9%	AIG_MRT	80
True Density (kg WM/m^3)	1177.9	91.0	7.7%	AIG_MRT	80
Leaf	**Mean**	**Std. Dev.**	**Coef. of Variation**	**Location**	**n**
Mass (g)	1.29	0.62	47.9%	AIG_MRT	60
Leaf Thickness (mm)	0.54	0.08	15.6%	AIG_MRT	60
True Density (kg WM/m^3)	558.4	165.5	29.6%	AIG_MRT	51
Leaf Area (mm^2)	4204.5	1924.8	45.8%	AIG_MRT	51
Leaf Perimeter (mm)	348.5	93.81	26.9%	AIG_MRT	51
Petiole	**Mean**	**Std. Dev.**	**Coef. of Variation**	**Location**	**n**
Mass (g)	0.36	0.26	70.4%	PIC	50
Average Diameter (mm)	2.29	0.60	26.3%	PIC	50
True Density (kg WM/m^3)	1222.3	121.4	9.9%	PIC	50
Length (mm)	64.11	17.22	26.9%	PIC	50

AIG_MRT: Aigues-Mortes
PIC: Pauillac

The results from coefficient of restitution tests can be found in Table 5.6. With the exception of the grape-petiole and petiole-petiole interactions, all interactions are from the Aigues-Mortes location. The interaction values range between 0.134 and 0.357 for the coefficient of restitution and between 10.2% and 30.7% for the coefficient of variation. The leaf surface material had the highest values with an average of 0.320. The leaf surface was created using multiple stacked leaves that were tightly secured together. That may have increased the leaf density and hardness causing for a larger bounce height; a harder material is less likely to dampen the impact of an object than a softer material. The conveyor rubber and stainless steel surfaces had similar average values of 0.292 and 0.284 respectively. The relative hardness of these materials can explain the similarity between them. An intermediate average value for the petiole surface was 0.256. This lower value can be attributed to the softer nature of the petioles

that are capable of absorbing the impact of dropped objects. The grape surface had the smallest average coefficient of restitution value of 0.172; being the softest and most flexible material can explain the low value in caparison to the other materials.

Table 5.6. Coefficient of restitution of biological materials used for the Discrete-Element Method simulations.

Interaction	Mean	Std. Dev.	Coef. of Variation	Location	n
Grape-Grape	0.134	0.017	12.4%	AIG_MRT	68
Petiole-Grape	0.210	0.057	27.0%	AIG_MRT	53
Grape-Leaf	0.357	0.036	10.2%	AIG_MRT	70
Petiole-Leaf	0.283	0.052	18.4%	AIG_MRT	51
Grape-Steel	0.329	0.043	13.0%	AIG_MRT	30
Petiole-Steel	0.239	0.046	19.2%	AIG_MRT	32
Grape-Conveyor	0.312	0.033	10.6%	AIG_MRT	34
Petiole-Conveyor	0.272	0.057	21.0%	AIG_MRT	42
Grape-Petiole	0.298	0.048	16.2%	PIC	45
Petiole-Petiole	0.213	0.066	30.7%	PIC	47

AIG_MRT: Aigues-Mortes
PIC: Pauillac

Table 5.7 displays the angle of static friction between the biological materials themselves and the cleaning system materials. Given its completeness, the entire data set was taken from the Aigues-Mortes location. The friction angle between the biological materials themselves ranged from 30.2° to 50.0°; the coefficients of variation were between 9.8% and 20.6%. The friction angle varied significantly from one interaction to another due to the differences between the materials. The friction angles between the biological and cleaning system materials were between 22.0° and 50.8° with coefficients of variations ranging from 14.7% to 20.8%. The average angle between the stainless steel and the biological material was 24.8°; this was the smallest in comparison to the other materials. The stainless steel used in grape harvesters is

subjected to a passivation treatment in order to meet food handling standards. The process provides a smooth non-adhesive finish, which would explain the small friction angle. The largest observed angle amongst the cleaning system material was with the conveyor rubber at 48.9°. The conveyor rubber can exhibit an adhesion effect between itself and the contacting material despite the relatively smooth surface. Overcoming the frictional forces becomes more difficult, therefore increasing the friction angle.

Table 5.7. Angle (°) of static friction of biological materials used for the Discrete-Element Method simulations.

Interaction	Mean	Std. Dev.	Coef. of Variation	Location	n
Grape-Grape	49.6	8.6	17.3%	AIG_MRT	60
Grape-Leaf	34.2	6.7	19.5%	AIG_MRT	39
Leaf-Leaf	48.0	9.9	20.6%	AIG_MRT	44
Petiole-Leaf	30.2	4.7	15.5%	AIG_MRT	38
Grape-Petiole	32.1	3.1	9.8%	AIG_MRT	30
Petiole-Petiole	50.0	9.3	18.6%	AIG_MRT	50
Grape-Steel	22.0	3.4	15.6%	AIG_MRT	36
Leaf-Steel	30.2	6.3	20.8%	AIG_MRT	36
Petiole-Steel	22.1	3.3	14.7%	AIG_MRT	31
Grape-Conveyor	47.5	9.6	20.1%	AIG_MRT	37
Leaf-Conveyor	48.4	9.0	18.6%	AIG_MRT	41
Petiole-Conveyor	50.8	10.5	20.8%	AIG_MRT	53

AIG_MRT: Aigues-Mortes

The measured terminal velocity and the calculated drag coefficient for the biological materials are shown in Table 5.8. The entire Aigues-Mortes dataset was used since it had the complete set of tests for each biological material. It appears that the order of the terminal velocities corresponds to the same order as the masses. The grapes had both the largest mass and terminal velocity at 1.25 g and 22.71 m/s respectively. The petiole samples had the second

largest mass, therefore corresponding to the second largest terminal velocity at 12.50 m/s. The leaf samples had the smallest terminal velocity at 1.88 m/s.

In a similar way as the terminal velocity, the order of the drag coefficients corresponded to the size of the material projected areas. The largest drag coefficient value was calculated at 1.909 for the leaf samples; it had the largest projected area perpendicular to the airflow. The grapes had the second largest value at 0.275 with a larger projected area than the petioles. The petioles had the smallest value of 0.074; the projected area was based on the small cylinder shape and vertical orientation (parallel to the airflow).

Table 5.8. Aerodynamic characteristics of grapes used for the Discrete-Element Method simulations.

Ter. Velocity (m/s)	Mean	Std. Dev.	Coef. of Variation	Location	n
Grape	22.71	0.96	4.2%	AIG_MRT	30
Leaf (disc cut out)	1.88	0.18	9.4%	AIG_MRT	30
Petiole	12.50	3.63	29.1%	AIG_MRT	42

Drag Coefficient (--)	Mean	Std. Dev.	Coef. of Variation	Location	n
Grape	0.275	0.046	16.7%	AIG_MRT	30
Leaf (disc cut out)	1.909	0.697	36.5%	AIG_MRT	30
Petiole	0.074	0.034	45.8%	AIG_MRT	42

AIG_MRT: Aigues-Mortes

5.2. Physical Property Simulation and Validation

5.2.1. Inclined Plane Simulation

Table 5.9 compares the actual test results to the DEM simulation results for the static friction angles. The test angles in the table below are the results from the complete population that were presented in the previous section. The standard deviation and coefficient of variation in this table describe the simulation results. These results correspond to an average of 100 samples that were tested on a single incline plane for each different interaction. Multiple iterations of each interaction simulation were conducted while adjusting the linear cohesion model. This was done until the average of each DEM angle was within 5% difference of the actual test angle; the percentage difference did not exceed 4.5%. Both the standard deviations and coefficients of variation are small in value because the simulation is able to produce repeatable results at a high precision. The adjustment of the linear cohesion model was accomplished by trial and error and by general observations of the material behavior.

Table 5.9. Static friction angle comparison between the actual tests and the Discrete-Element Method simulations.

Interaction	Test Angle (°)	DEM Angle (°)	Std. Dev.	Coef. of Variation	% Diff.
Grape-Steel	22.0	22.1	0.1	0.5%	0.5%
Grape-Conveyor	47.5	47.2	0.7	1.6%	0.6%
Petiole-Steel	22.1	23.0	0.2	0.7%	4.0%
Petiole-Conveyor	50.8	51.5	0.9	1.7%	1.4%
Grape-Grape	49.6	49.4	0.8	1.6%	0.4%
Leaf-Steel	30.2	30.8	0.2	0.8%	2.0%
Leaf-Conveyor	48.4	48.0	1.1	2.3%	0.8%
Grape-Petiole	32.1	33.2	0.4	1.2%	3.4%
Petiole-Leaf	30.2	31.6	0.5	1.5%	4.5%
Petiole-Petiole	50.0	51.0	1.1	2.1%	2.0%
Leaf-Leaf	48.0	47.5	1.0	2.1%	1.0%
Grape-Leaf	34.2	35.6	0.5	1.5%	4.0%

5.2.2. Rebound Surface Simulation

The comparison between the actual tests and the DEM simulation for the coefficients of restitution can be seen in Table 5.10. As previously mentioned, the leaves were excluded as a dropped material because the large surface area exhibited a lift force. This created a parachuting effect, which made its bounce height negligible. Its coefficient of restitution in the DEM simulations was therefore set to a very low value. Despite this, the leaves were still used as a surface material for the other particles. Similar to the friction test simulations, 100 samples were tested on each surface material while varying the coefficient of restitution parameter. This was done until the DEM simulation was within 5% difference of the actual test value.

As the table below demonstrates, the interactions where the grapes were dropped have standard deviations and coefficients of variation equal to 0. The 100 dropped samples had no variations between them given the repeatability and high precision of the simulations. For the grapes, it was possible to adjust the simulation parameters until the coefficient of restitution exactly matched the actual tests. As mentioned in section 4.2.3, the linear cohesion model varied the bounce heights depending on the orientation of the petioles. A larger amount of contacting spheres increased the cohesion force while reducing the bounce height. For that reason, simulations for both the horizontal and vertical orientations of the petioles were adjusted until they were within 5% of the actual value. The petiole interaction values displayed in the table below correspond to the averaged coefficient of restitution for the two simulations. In general, both simulations for each petiole interaction were within 1% of the actual value with a fairly low variation.

Table 5.10. Coefficient of restitution (COR) comparison between the actual tests and the Discrete-Element Method simulations.

Interaction	Test COR	DEM COR	Std. Dev.	Coef. of Variation	% Diff.
Grape-Steel	0.329	0.329	0	0.0%	0.0%
Petiole-Steel	0.239	0.238	1.41E-03	0.6%	0.4%
Grape-Conveyor	0.312	0.307	0	0.0%	1.6%
Petiole-Conveyor	0.272	0.271	1.41E-03	0.5%	0.4%
Grape-Grape	0.134	0.134	0	0.0%	0.0%
Grape-Petiole	0.298	0.298	0	0.0%	0.0%
Grape-Leaf	0.357	0.356	0	0.0%	0.3%
Petiole-Petiole	0.213	0.213	9.57E-04	0.5%	0.0%
Petiole-Grape	0.21	0.209	2.22E-03	1.1%	0.5%
Petiole-Leaf	0.283	0.283	2.06E-03	0.7%	0.0%

5.2.3. Simulation and Validation of Leaf Deflection

The following sections describe the results for the two deflection validation tests. Both the single and multi-deflection test results include a comparison between the actual and simulated leaf deflection shapes. The presented DEM leaf shapes are the optimized results following the adjustments of the bond properties in the particle body force.

5.2.3.1. Single Deflection for Cantilevered Leaf Sample

Figure 5.1 to Figure 5.5 shows the leaf sample deflection comparison between the DEM simulations and the actuals tests at different bolt heights. The deflection shape was plotted in 2-dimensions along the horizontal and vertical directions. The polynomial regressions of the graphs below display a goodness of fit value (R^2) that surpasses 0.99 for both the DEM and actual test deflections. These high R^2 values indicate that the regression lines accurately represent the deflection data points. An observational comparison of the deflections shows the largest difference between the simulation and actual test results at the 5 mm bolt height (Figure 5.1). A small deflection deviation can also be observed at the 22.5 mm bolt height (Figure 5.5). The remaining graphs indicate a fairly close match between the two compared deflections.

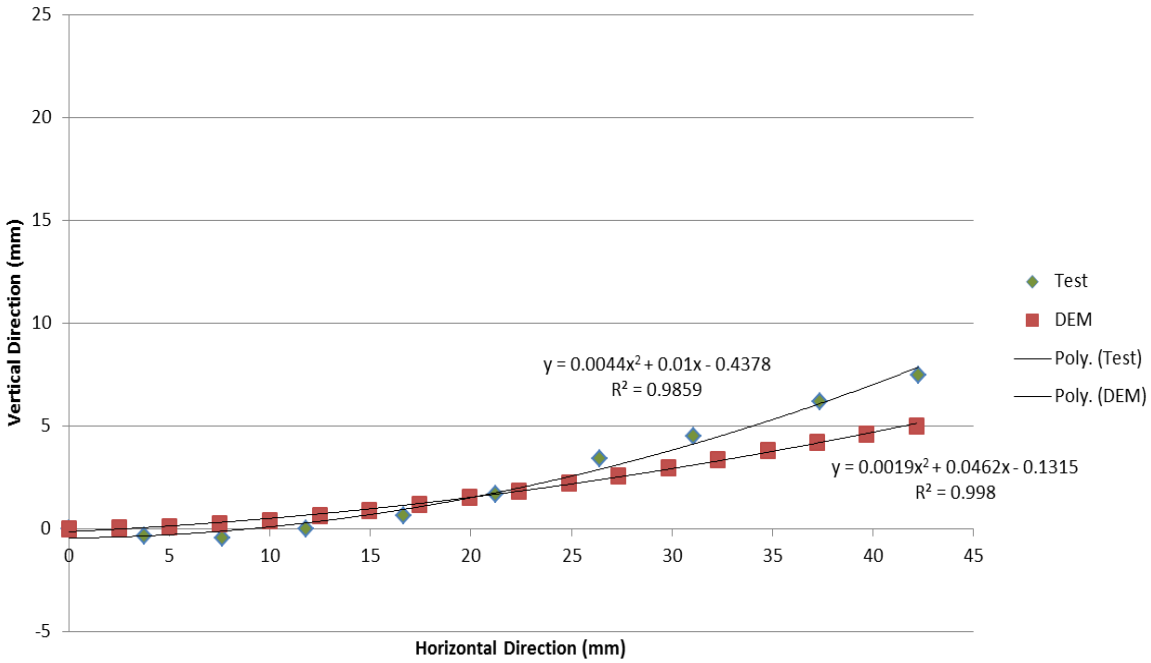

Figure 5.1. Graph of rectangular leaf sample deflection comparison between the Discrete-Element Method simulation and actual test at a 5 mm bolt height.

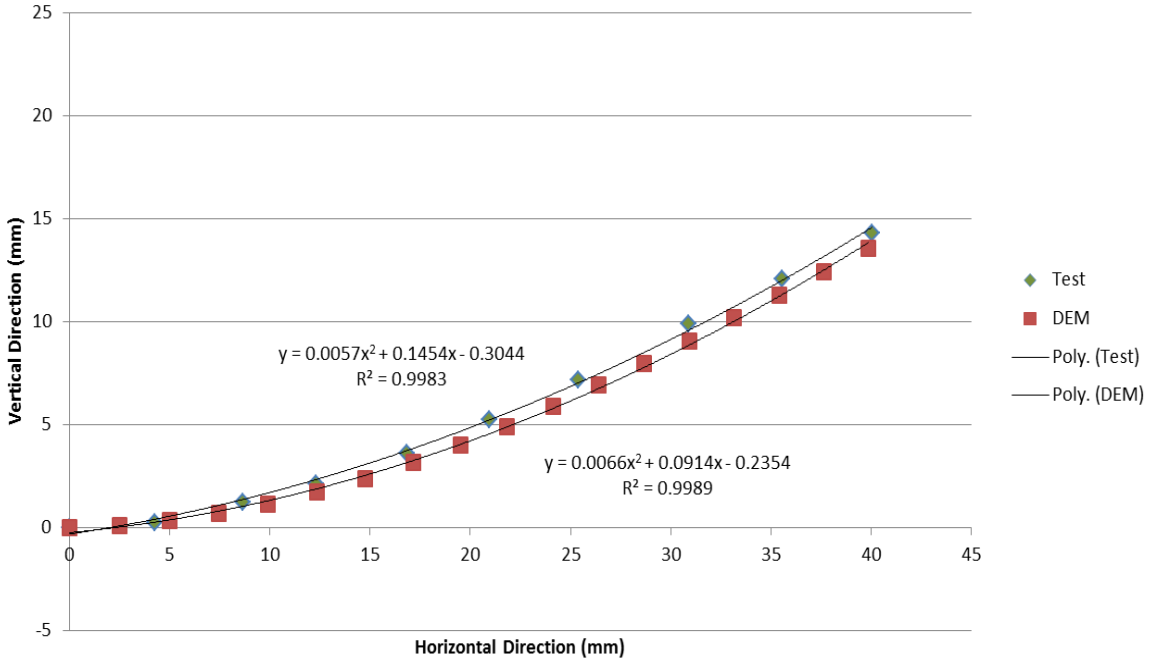

Figure 5.2. Graph of rectangular leaf sample deflection comparison between the Discrete-Element Method simulation and actual test at a 12 mm bolt height.

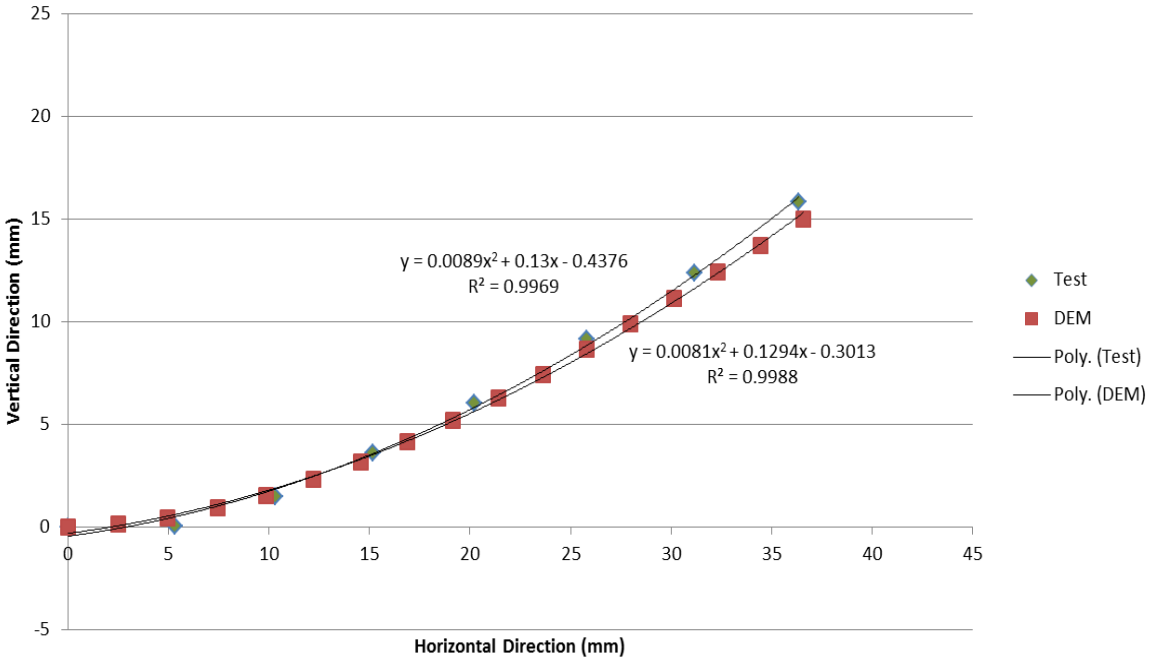

Figure 5.3. Graph of rectangular leaf sample deflection comparison between the Discrete-Element Method simulation and actual test at a 15 mm bolt height.

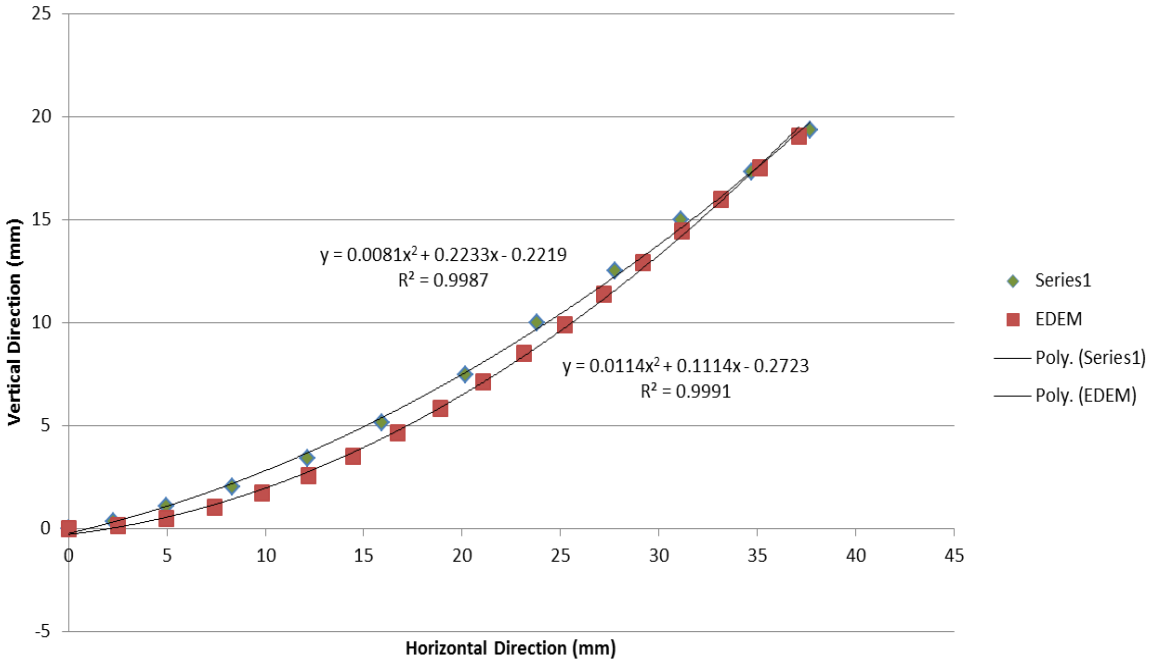

Figure 5.4. Graph of rectangular leaf sample deflection comparison between the Discrete-Element Method simulation and actual test at an 18 mm bolt height.

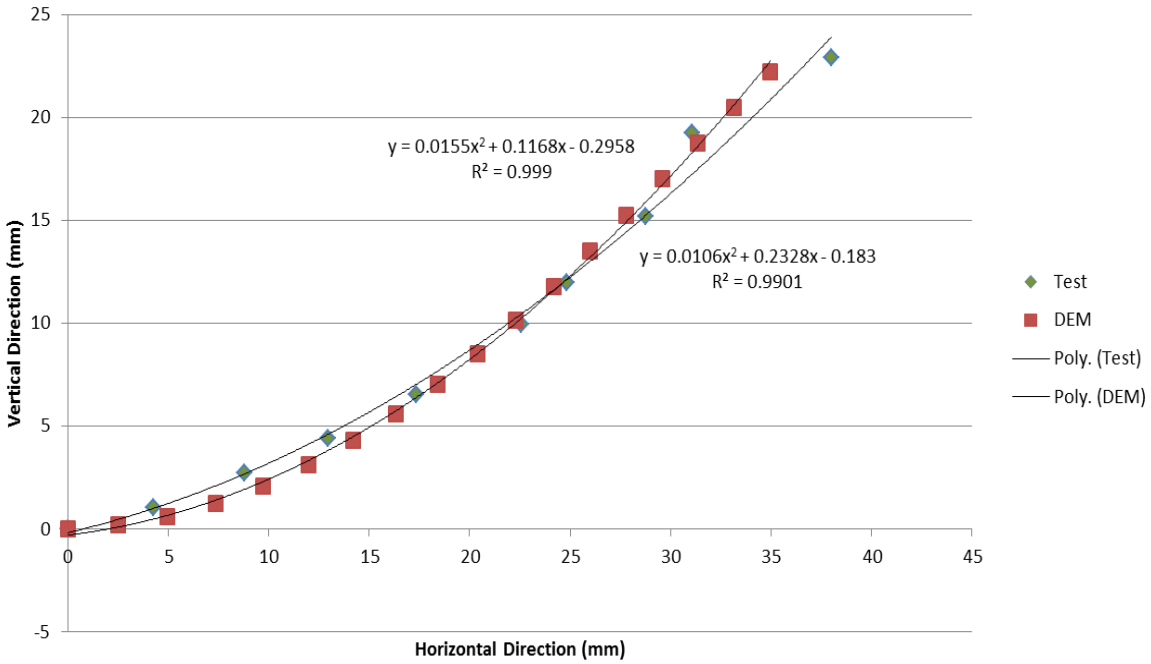

Figure 5.5. Graph of rectangular leaf sample deflection comparison between the Discrete-Element Method simulation and actual test at a 22.5 mm bolt height.

Table 5.11 compares the results for deflection and angle of deflection between the simulations and the actual tests (see section B.2 of APPENDIX B for sample calculation). As seen in Figure 5.1, the largest deviation between the simulated and actual tests was present at the 5 mm bolt height; the differences in deflection and angle of deflection were 40.0% and 59.9% respectively. The 12 mm and 15 mm bolt heights had the smallest differences below 3% for the angle of deflection. The 18 mm and 22.5 mm bolt heights had slightly higher deviations for the angle of deflection at 13.6% and 14.5% respectively. With the exception of the 5 mm bolt height, the deflection differences between the simulations and actual tests were all less than 6%. These discrepancies can be attributed to the positioning of the bolt with respect to the leaf sample particles. The bolt may have been positioned between or directly on the spherical particles. Samples could be slightly lower or higher depending on this positioning. In general, the DEM

simulation parameters were able to accurately replicate the deflection behavior of the rectangular leaf sample.

Table 5.11. Rectangular leaf sample deflection and angle of deflection comparison between the Discrete-Element Method simulation and actual tests.

	Deflection (mm)			Angle of Deflection (°)		
Bolt Height (mm)	Test	DEM	%Diff.	Test	DEM	%Diff.
5.0	7.5	5.0	40.0%	21.9	11.8	59.9%
12.0	14.3	13.5	5.8%	34.5	35.4	2.6%
15.0	15.8	16.3	3.1%	44.5	43.4	2.5%
18.0	19.3	19.1	1.0%	47.8	54.8	13.6%
22.5	22.9	22.2	3.1%	59.5	68.8	14.5%

5.2.3.2. Multi-Deflections of Leaves

As previously mentioned, a single leaf was analyzed for the five deflection configurations. Multiple iterations for each configuration was done while adjusting the bond properties of the leaf particles. In particular, the leaf rigidity was modified to try and capture the deflection shape of the actual leaf. In general, the simulated leaf was able to flex and move freely when subjected to the deflections. It was capable of replicating the general shape of the scanned leaf; however, significant discrepancies between the compared leaves were evident. Figure 5.6 shows the scans of the actual leaf without being subjected to any deflections. It can be seen that the leaf is naturally deformed and has distinct curves along its edges. The simulated leaf was created using a 2-dimensional grid based on the original leaf's contour. For that reason, the natural curves of the actual leaf could not be replicated without applying external forces. The deviations between the scanned and simulated leaves can be attributed to this discrepancy.

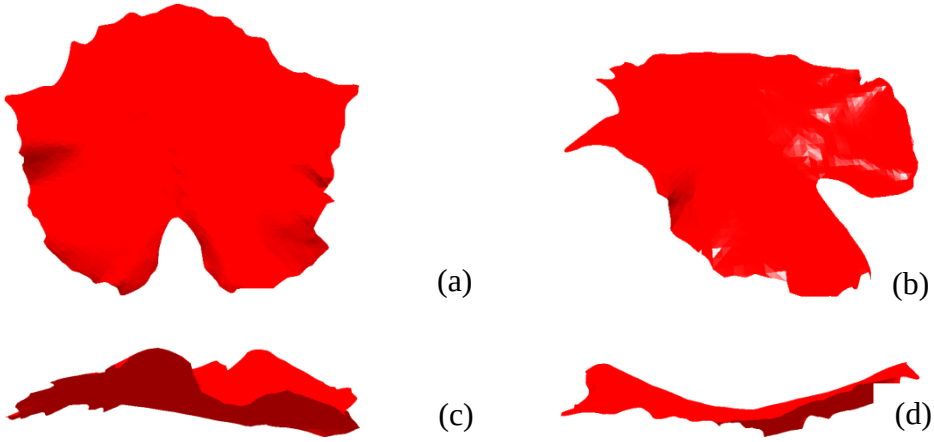

Figure 5.6. Scanned leaf without being subjected to a deflection. (a) Top view. (b) Orthogonal view. (c) Side view. (d) Front view.

Figure 5.7 is an example of the comparison between the simulated and scanned leaves from multiple views. Configuration 5 is displayed in this figure with the .STL file being overlaid on the simulated leaf into the DEM software. The comparisons of the other configurations can be found in section C.3 of APPENDIX C. For this particular configuration, the simulated leaf did follow the general deformation trends of the actual leaf. The small curves along the edges and the medium curves around the center region were not completely captured. The bottom and top regions of the leaf appeared to have been correctly aligned with the scanned leaf. Prior to adjusting the bond parameters, the leaf was not capable of maintaining a concave shape. It had a tendency of folding over itself and not remaining upright. By gradually adjusting the rigidity, the leaf was eventually able to form a realistic leaf shape.

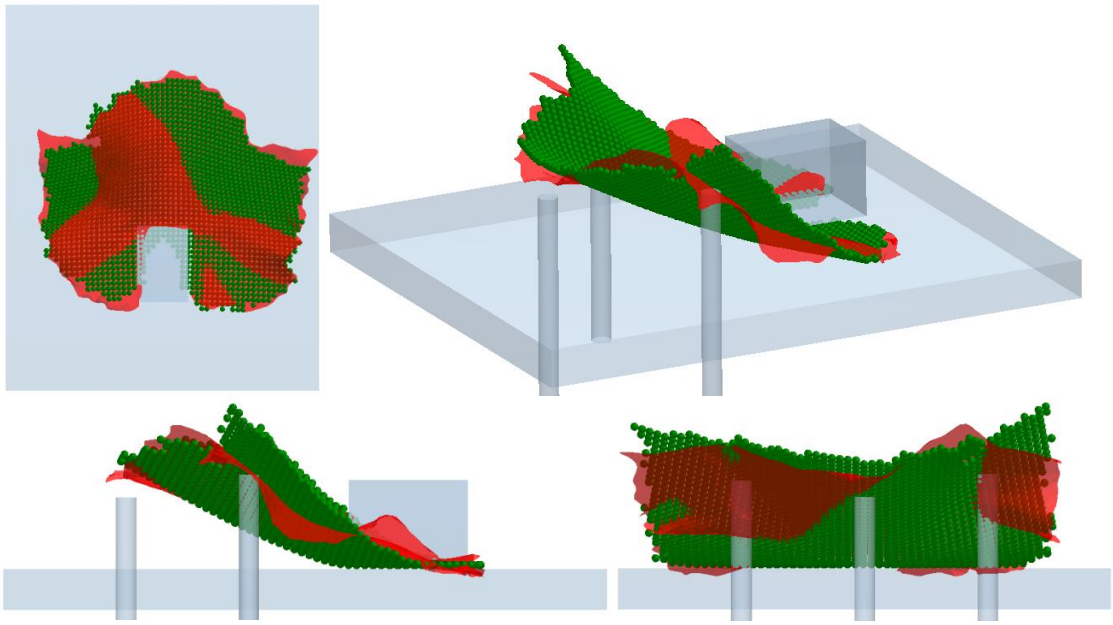

Figure 5.7. Multi-deflection test comparison -Configuration 5. (a) Top view. (b) Orthogonal view. (c) Side view. (d) Front view.

The other tested configurations displayed a similar behavior as described above for the configuration 5. The bond parameters continued to be adjusted until a reasonable equilibrium was found for all the configurations. Despite this, significant deviations were still identified in some areas of the leaf. The inability of the leaf to have a natural deformation and a varying rigidity in specific areas contributed to these deviations. The structure of the actual leaf included a midrib along its center with lateral veins branching out. The areas with these veins appeared to have a higher rigidity than the leaf blade area. The slight offset of the midrib and the non-uniform location of the lateral veins caused the leaf to deflect irregularly. The simulated leaf had a consistent bond strength and rigidity between its spheres; its deflections could not account for the varying proprieties across the leaf area. The simulated leaf would have to incorporate an increased rigidity in the vein areas to fully capture the behavior of the actual leaf. That being said, the leaf was adjusted to the best of its abilities using the 2-dimensional grid and bond parameters in the particle body force.

5.2.4. Grape Trajectory Simulation

The following figures (Figure 5.8 to Figure 5.10) show the conveyor trajectories for the three sets of results at alternate speeds (300 rev/min (1.2 m/s), 400 rev/min (1.6 m/s), and 500 rev/min (2.0 m/s)) and at a constant 15° angle. The analytical model (blue), the DEM simulation (red), and the experimental results (green) are plotted with respect to the vertical and horizontal distances from the end of the conveyor. The plotted trajectories are second order polynomial regression lines fitted to scattered data points. The R^2 for the experimental results were between 0.81 and 0.93; the analytical and DEM trajectories had R^2 values above 0.97. These high R^2 values indicate that the regression lines reasonably replicate the trajectories.

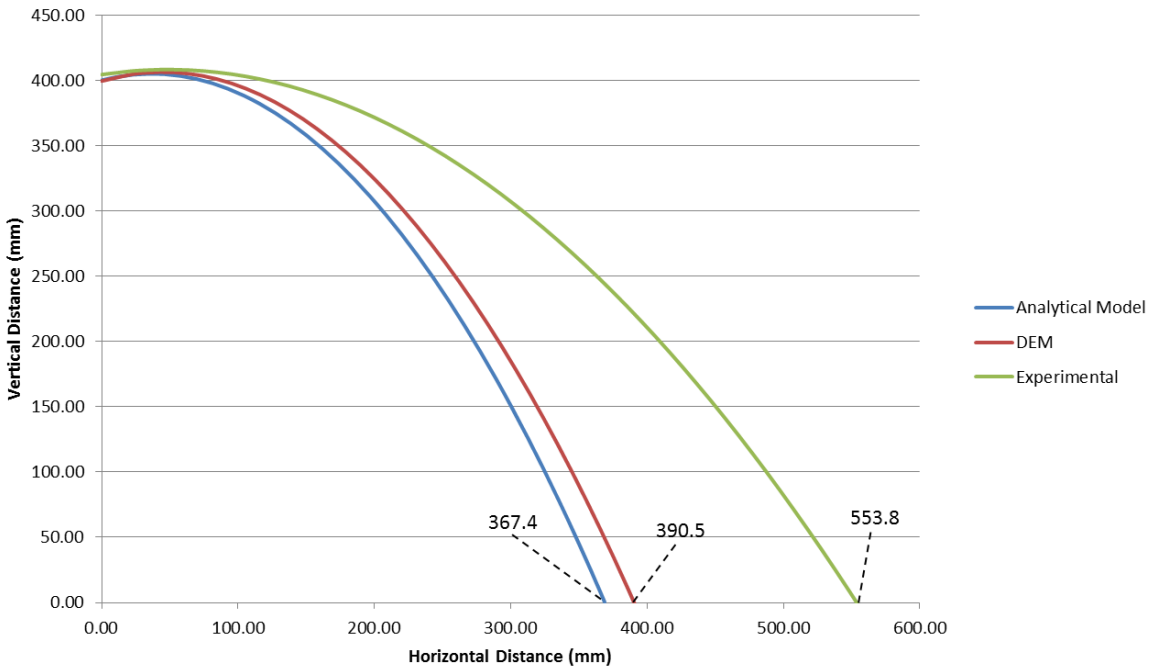

Figure 5.8. The conveyor (at 300 rev/s (1.2 m/s) and 15°) trajectory comparison between the analytical model, Discrete-Element Method simulation, and experimental results.

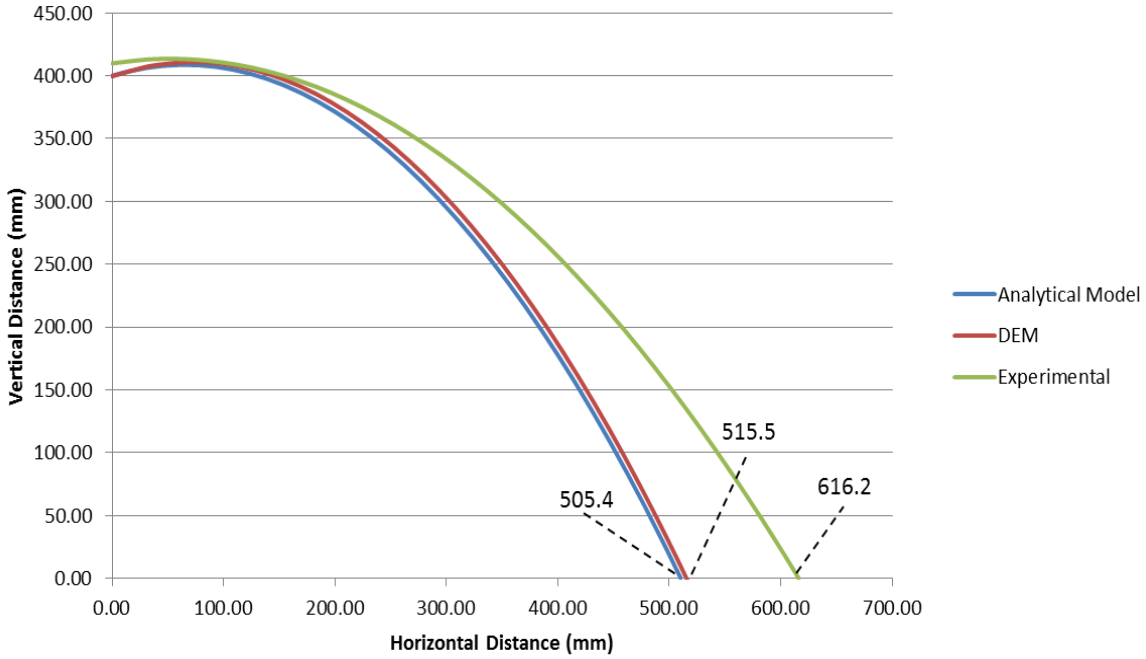

Figure 5.9. The conveyor (at 400 rev/s (1.6 m/s) and 15°) trajectory comparison between the analytical model, Discrete-Element Method simulation, and experimental results.

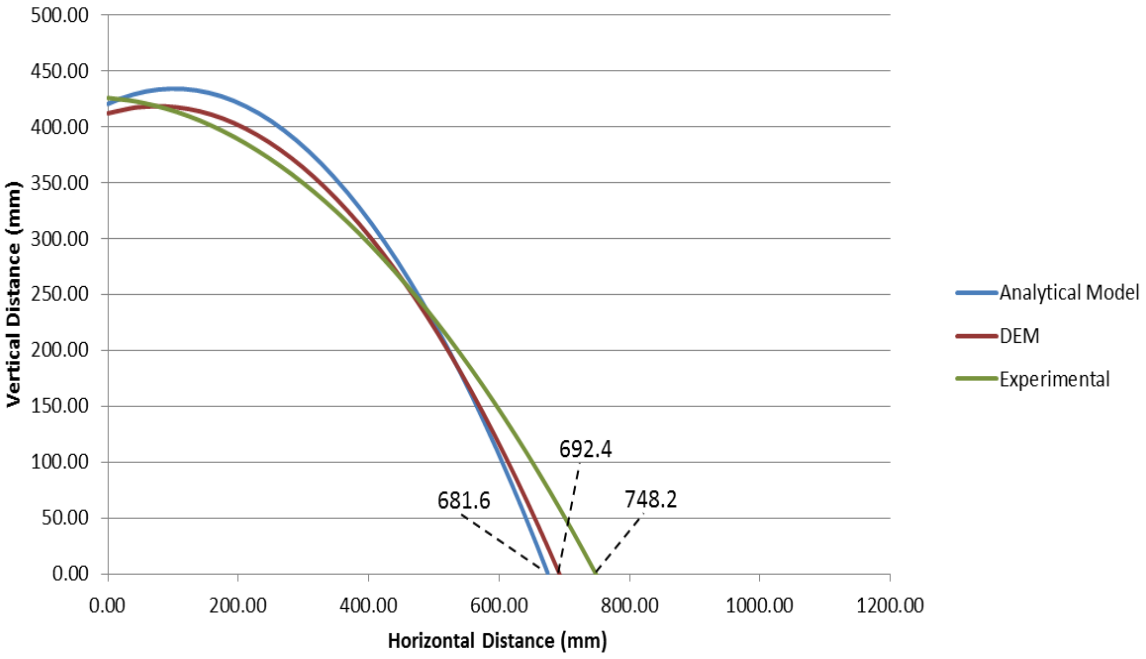

Figure 5.10. The conveyor (at 500 rev/s (2.0 m/s) and 15°) trajectory comparison between the analytical model, Discrete-Element Method simulation, and experimental results.

Table 5.12 outlines the percentage difference between each trajectory for the three conveyor speeds. In general, the trajectories appeared to have a greater horizontal distance as the conveyor speed was increased. The experimental results had the longest horizontal distance at all three speeds. The DEM simulation was the second furthest followed by the analytical model in third. As the speed increased, all three trajectories appeared to converge on themselves by having less of a difference between each other. The largest difference occurred between the experimental and analytical model; the differences at 300 rev/min (1.2 m/s), 400 rev/min (1.6 m/s), and 500 rev/min (2.0 m/s) were 40.5%, 19.8%, and 9.3% respectively. The experimental and DEM simulation results were closer in comparison (34.6%, 17.8%, and 7.7%) than the analytical model and experimental. The smallest difference in horizontal distance was between the DEM simulations and the analytical model (6.1%, 2.0%, and 1.6%). This can be explained by the use of similar displacement equations in both the DEM simulation and analytical model. The small differences can be attributed to the influence of the other applied contact models; the effect of friction and adhesion were incorporated in the simulations.

The discrepancies between the simulations and the experimental trajectories could be the result of the DEM limitations. This includes the inability to elastically or plastically deform the particles at the contacts. In the experimental trials, some grapes ruptured upon contact with the conveyor; the damaged grapes may have had different trajectories. The rolling friction parameter in the simulations was adjusted to try and minimize the differences, but no significant effect was observed. As a result, the particle adhesion effect with the moving conveyor belt was possibly not accounted for in the simulation. Another possible cause for the discrepancies may have been the increased effects of gravity and friction on the initial acceleration of the grapes as they were

propelled from the conveyor. Despite these differences, the DEM simulations still managed to reasonably replicate behavior of the grapes on the conveyor.

Table 5.12. Horizontal distance comparison between the analytical model, Discrete-Element Method simulation, and experimental trajectories.

300 rev/min (1.2 m/s)			Analytical Model	DEM	Experimental
	Horizontal Distance (mm)		367.4	390.5	553.8
	%Diff.	Analytical Model	--------		40.5%
		DEM	6.1%	--------	
		Experimental		34.6%	--------
400 rev/min (1.6 m/s)			Analytical Model	DEM	Experimental
	Horizontal Distance (mm)		505.4	515.5	616.2
	% Diff.	Analytical Model	--------		19.8%
		DEM	2.0%	--------	
		Experimental		17.8%	--------
500 rev/min (2.0 m/s)			Analytical Model	DEM	Experimental
	Horizontal Distance (mm)		681.6	692.4	748.2
	% Diff.	Analytical Model	--------		9.3%
		DEM	1.6%	--------	
		Experimental		7.7%	--------

5.2.5. Main Crop Flow Simulation

The experimental results of the leaf aspiration success rate are discussed and compared to the main crop flow simulation. The overall cleaning performance and observed biological material behavior are also explained with respect to the nine conveyor configurations.

5.2.5.1. Experimental-Grape Harvester Test Bench

The leaf aspiration success rate and the general behavior of the biological materials were observed in the grape harvester test bench trials. Table 5.13 shows the averaged success rate results for the two trials per configuration. The success rate is expressed as a percentage of leaves that were aspirated. The standard deviation and coefficient of variation are moderately high for some configurations (>10%). This was caused by the small amount of trials, which were limited by the availability of the leaves from Ontario. Although a collection screen was installed, a maximum of two uses could be done before the leaves were significantly damaged. Further testing with the same leaves may not have provided representative results. An increased number of trials with additional leaves would have increased the statistical power of the experiment.

In general, the best cleaning performance was observed at the 20° angle followed by the 15° and 10° angles. The best performing speed was at 420 rev/min (1.7 m/s) followed by the 500 rev/min (2. m/s) and 350 rev/min (1.4 m/s) speeds. The best combined cleaning configuration was at a speed of 420 rev/min (1.7 m/s) for both the 15° and 20° angles with a success rate of 85.0%. The 20° angle configuration at speeds of 350 rev/min (1.4 m/s) and 500 rev/min (2.0 m/s) had the next best performances with success rates of 80.0% and 77.5%, respectively. The worst performances were at a speed of 350 rev/min (1.4 m/s) for the angles of 10° and 15°; the success

rates were 55.0% and 62.5%, respectively. An intermediate success rate of approximately 70.0% was observed in the remaining three configurations: 420 rev/min (1.7 m/s)-10°, 500 rev/min (2.0 m/s)-10°, and 500 rev/min (2.0 m/s)-15°.

Table 5.13. Results of leaf aspiration success rate for the grape harvester test bench trials.

	10°			15°			20°		
Speed	Mean	STDEV	COV	Mean	STDEV	COV	Mean	STDEV	COV
350 rev/min (1.4 m/s)	55.0%	7.1%	12.9%	62.5%	17.7%	28.3%	80.0%	7.1%	8.8%
420 rev/min (1.7 m/s)	74.5%	6.3%	8.5%	85.0%	7.1%	8.3%	85.0%	0.0%	0.0%
500 rev/min (2.0 m/s)	67.5%	10.6%	15.7%	72.5%	17.7%	24.4%	77.5%	10.6%	13.7%

STDEV: Standard Deviation
COV: Coefficient of Variation

5.2.5.1.1. Statistical Analysis

The tests followed a factorial experimental design with the conveyor angle and speed as the explanatory variables and the aspiration success rate as the response variable. A combination of three angles and three speeds were tested. A general linear model (GLM) with these variables was fitted. Given the experimental design, the explanatory variables were coded as factors instead of continuous variables. An ANOVA analysis of the GLM model provided p-values to determine the significant effects; a p-value below 0.05 indicates a significant effect.

```
model1<-glm(S_RATE~factor(ANGLE)*factor(SPEED),data=Data_2)
anova(model1,test="F")
```

Table 5.14 displays the ANOVA results from the GLM model. The p-values from this analysis were all above 0.05 (95% confidence level), which indicated that the conveyor speed and angle had no significant effect on the success rate. The results also indicated that the speed

and angle were independent of each other. Despite this, the p-values for the speed (0.08887) and angle (0.10104) variables were not overly high. In essence, these results could also be interpreted as inconclusive given the small sample space of the experiment. Unfortunately, the available time and resources were very limited for this testing phase of the project. A higher number of trials (~5-10 per configuration) with more leaves would have increased the statistical power and provided more conclusive results.

Table 5.14. Analysis of variance results for experimental-grape harvester test bench.

	Df	Deviance Resid.	Df	Redis. Dev	F	Pr(>F)
NULL			17	0.26870		
ANGLE	2	0.069087	15	0.19962	2.9892	0.10104
SPEED	2	0.074096	13	0.12552	3.2059	0.08887
ANGLE:SPEED	4	0.021516	9	0.10401	0.4655	0.76002

A quantile (Q-Q) plot was done for this model to verify the normal distribution assumption for a GLM. Figure 5.11 displays the QQ plot for the model and confirms a fairly normal distribution.

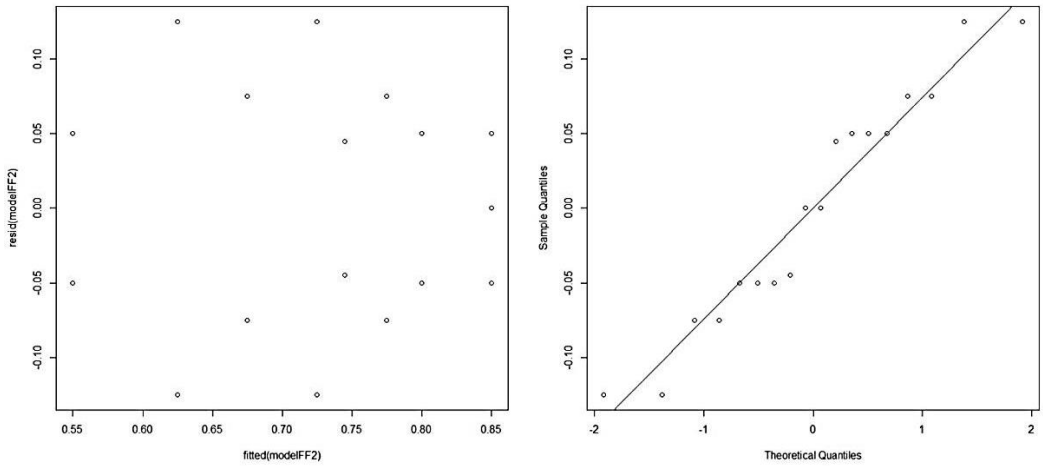

Figure 5.11. Quantile-quantile (Q-Q) plot for fitted GLM model of experimental-grape harvester test bench results.

Although the results from Table 5.13 indicated certain performance trends with respect to the conveyor settings, the statistical results showed that they were not statistically significant. Observationally, an increasing angle and speed did appear to change the behavior of the biological materials. Figure 5.12 shows a testing example of the grape harvester test bench. The highest success rate at the 20° angle was the result of a mixing effect and higher trajectory path. During the tests, it was observed that the steeper angle created a mixing effect that allowed the biological materials to turn over. Leaves that would normally become trapped underneath other materials could be freed before entering the aspirator airstream. Otherwise, the leaves would be weighed down by other materials and prevented from being aspirated. This steeper angle also propelled the biological materials with a more direct path into the aspirator hood where the air velocity was higher. The higher location in the aspirator hood provided a longer period of time for the MOG materials to be aspirated. A slipping effect between the biological materials and the conveyor was also observed at higher conveyor speeds. Table 5.13 did show a reduction in the success rate at the 500 rev/min (2.0 m/s) speed in comparison to the 420 rev/min (1.7 m/s) speed for all three angles. The 500 rev/min (2.0 m/s) speed appeared too fast to carefully handle the biological materials; they had a tendency of being thrown in the opposite direction of the conveyor travel. Grape damage would be inevitable at this high transport speed.

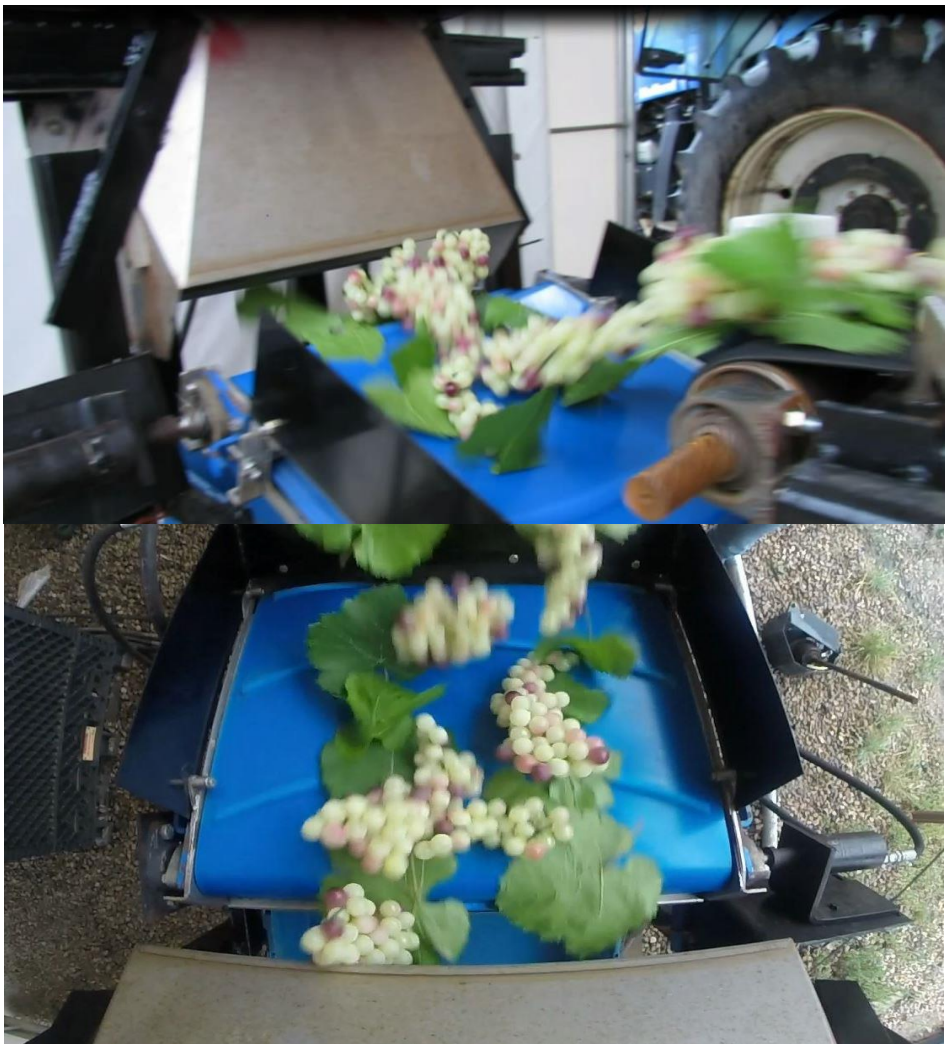

(a)

(b)

Figure 5.12. Testing example of grape harvester test bench with 350 rev/min (1.4 m/s) and 20° conveyor settings. (a) Orthogonal view. (b) Top view.

Ultimately, the randomized placement of the leaves will determine the probability of being aspirated. The more materials that cover the leaves, the less likely they are of being aspirated. In actual grape harvesters, the mesh conveyor is positioned directly below the aspirator. This provides an additional opportunity for missed leaves to be aspirated. Materials landing on the moving mesh conveyor are also subject to a mixing effect; leaves can be freed and then aspirated.

5.2.5.2. Crop Flow DEM Simulation

The nine conveyor configurations were implemented in nine separate DEM simulations; the aspiration success rate and the general cleaning performance were determined. The parameters for the introduction of the biological materials were kept constant throughout all the configurations. Figure 5.13 displays an example of a main crop flow simulation; this particular one is with the 420 rev/min (1.7 m/s) and 15° conveyor settings. All three biological materials are being propelled from the conveyor into the aspirator upward airstream.

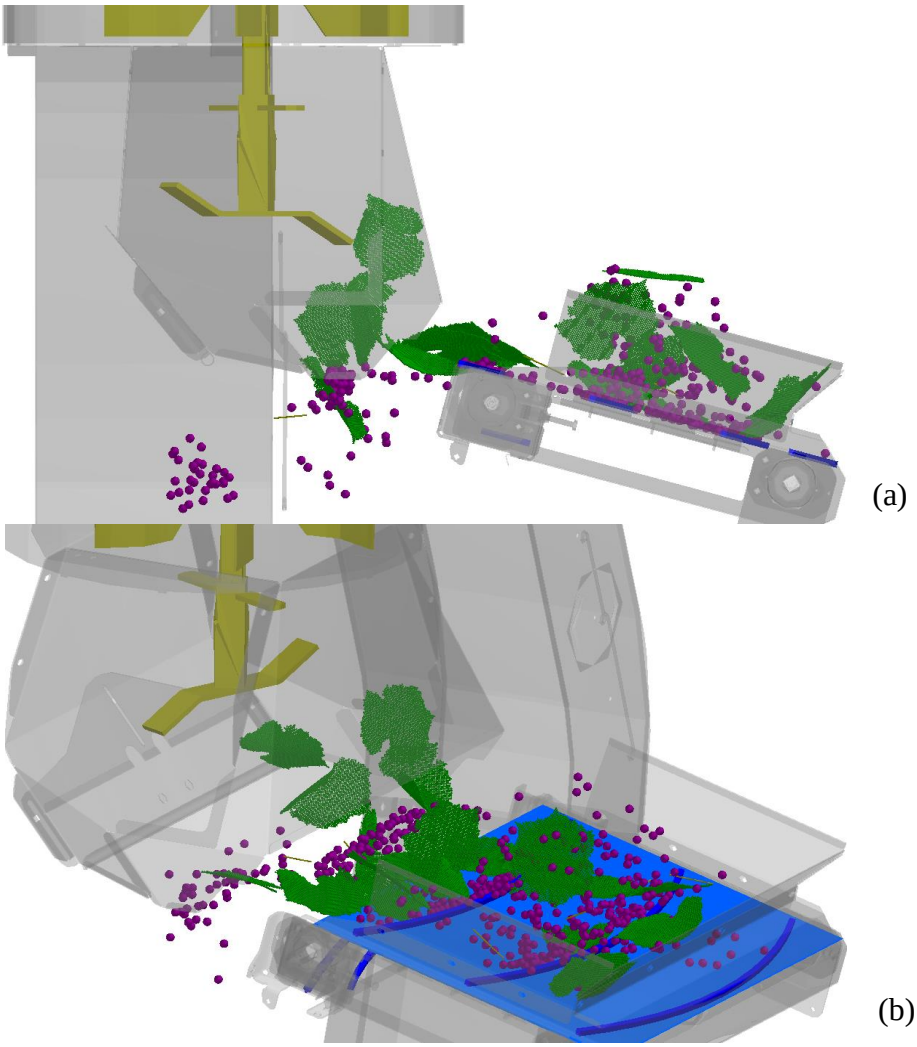

Figure 5.13. Example of main crop flow model with 420 rev/min (1.7 m/s) and 15° conveyor settings. (a) Side view. (b) Orthogonal view.

The leaves used in the experimental tests had petioles still attached. Having the petioles attached to the leaves in the simulations was beyond the scope of the project. Including individual petioles in the simulations may not have been imperative since their elimination was not a parameter of the validation process. As a precaution, they were included within the main crop flow simulations to account for any possible effect they may have had in the experimental tests. Although attached to the leaves, the petioles still interacted with other materials and the conveyor belt; for that reason it was deemed prudent to include them in the simulations.

In actual grape harvesters, petioles that are still attached to the leaves typical get aspirated with the leaves. This occurs since the leaves have a larger drag coefficient and a lower density than petioles. As observed during the terminal velocity tests, the petioles had a tendency of behaving sporadically in an airstream. A petiole drag coefficient is dependent on its orientation to the airflow direction; a perpendicular (horizontal) orientation has more lift than a parallel (vertical) orientation. From the aerodynamics testing, the grape, leaf, and petiole samples had average terminal velocities of 22.71 m/s, 1.88 m/s, and 12.50 m/s respectively (Table 5.8). Currently, the harvester aspirators are configured to have an airflow velocity of approximately 10 m/s near the entrance of the aspiration hood; the velocity increases further in the hood as the particles get closer to the impeller. To successfully aspirate individual petioles, they would have to be subjected to a higher air velocity. In the DEM simulations, no petioles were successfully aspirated in any of the nine conveyor configurations. Similarly to actual grape harvesters, individual petioles are rarely aspirated when separated from leaves. Increasing the air velocity at the hood inlet, could increase the success rate for both the leaves and petioles. However, the

expelled juice from the grapes would become susceptible to aspiration. This would cause an undesirable product loss.

Table 5.15 outlines the leaf aspiration success rate for the nine conveyor settings. The success rate is expressed as a percentage of leaves that were aspirated. The percentage difference in comparison to the benchmark configuration (420 rev/min (1.7 m/s)-15°) is presented in the brackets. In general, the cleaning performance increased with both the angle and speed. With the exception of the 10° angle, the success rate did increase with the conveyor speed. The 10° angle configurations had difficulties creating a mixing effect, which made the success rates completely dependent on the randomized placement of the materials rather than the conveyor settings. As observed in the experimental results, the steeper angles in the simulations had a tendency of propelling the materials with a more direct path into the aspirator. This subjected the materials to a greater air velocity (>10 m/s), thus increasing the success rate. The steeper angles also created a mixing effect, which helped separate the leaves from the other materials. Contrary to the experimental results, the 500 rev/min (2.0 m/s) speed had a higher success rate than the 420 rev/min (1.7 m/s) speed in the simulations. Like the grape trajectory simulations, the horizontal distances of the material appeared to be slightly scaled down compared to the experimental tests. The material acceleration from the conveyor may have also been affected by the increased effects of gravity and friction.

Table 5.15. Results of leaf aspiration success rate for the main crop flow simulation.

Speed	10°	15°	20°
350 rev/min (1.4 m/s)	86.1% (0.0%)	80.6% (-6.4%)	83.3% (-3.3%)
420 rev/min (1.7 m/s)	80.6% (-6.4%)	**86.1%**	94.4% (+9.6%)
500 rev/min (2.0 m/s)	88.9% (+3.3%)	94.4% (+9.6%)	97.2% (+12.9%)

When compared to the conventional conveyor settings (420 rev/min (1.7 m/s)-15°) the 420 rev/min (1.7 m/s)-20° and 500 rev/min (2.0 m/s)-20° configurations had increased performances of 9.6% and 12.9% respectively. Although a greater success rate was present with the 500 rev/min (2.0 m/s) speed, some materials were thrown in the opposite direction of the conveyor travel like in the experimental trials. The grapes also behaved sporadically by being propelled on the top of the aspirator hood. This would ultimately lead to more grape damage throughout the cleaning process. Considering product damage and the aspiration success rate, it is recommended to implement the 20° angle with the 420 rev/min (1.7 m/s) speed for an optimized configuration. A greater mixing effect was observed at this angle, which increased the chances of leaves being aspirated. The speed also provided the optimal trajectory for an increased success rate, while reducing product damage.

6.0 SUMMARY AND CONCLUSIONS

The principle objective of the project was to optimize the cleaning system of grape harvesters by developing a main crop flow simulation based on the Discrete-Element Method (DEM). This optimization included reducing the presence of foreign materials (petioles and leaves) for the same crop throughput. Individual simulations were validated using the physical characteristics and properties of biological materials (grape, petioles, and leaves) from the Cabernet Sauvignon grape variety. The parameters from these simulations were then applied in the main crop flow simulation, which included the cleaning system conveyor and aspirator. The leaf aspiration success rate was optimized by testing nine conveyor configurations that included three speeds (350 rev/min (1.4 m/s), 420 rev/min (1.7 m/s), 500 rev/min (2.0 m/s)) and three angles (10°, 15°, and 20°). The aspirator performance was validated with the experimental trials from the grape harvester test bench. Based on the project results, the following conclusions were drawn:

1. The individual crop flow simulations were able to replicate the physical characteristics and properties of the biological materials (grapes, leaves, and petioles).
    a. The inclined plane and rebound surface simulations were very accurate and could be adjusted within 5% of the actual tests.
    b. The single deflection tests for the leaf sample were fairly accurate when compared to the simulations. Some discrepancies could be attributed to the bolt positioning with respect to the leaf sample particles.
    c. The simulated leaf in the multi-deflection tests was able to replicate the general behavior of the actual leaf. Deviations near the edges and centre were identified. These

were caused by the inability of the simulated leaf to maintain a natural deflection without the application of external forces.

d. At lower speeds, the conveyor trajectory simulations had moderate differences with the experimental tests. The grape acceleration in the simulations was possibly affected by the increased effects of conveyor friction/adhesion and gravity acting on the grapes.

2. The optimized parameters from the individual simulations were integrated within the main crop flow simulation. The leaf aspiration success rate was compared between the simulations and the experimental trials.

   a. A statistical analysis for the experimental trials revealed that both the speed and angle variables did not have a significant effect on the success rate despite the low p-values. The small number of trials due the limited amount of available leaves contributed to the non-significance. Despite this, a mixing effect was observed at greater angles, which contributed to an increased success rate.

   b. The simulations did behave similarly to the experimental trials with respect to the conveyor angle. In general, the simulations showed that the cleaning performance increased with both the conveyor angle and speed. The 420 rev/min (1.7 m/s)-20° and 500 rev/min (2.0 m/s)-20° configurations had increased performances of 9.6% and 12.9% respectively when compared to the conventional conveyor settings (420 rev/min (1.7 m/s)-15°). Although the 500 rev/min (2.0 m/s) speed had a better success rate, it also showed signs of greater product damage. It was recommended that the 20° angle with the 420 rev/min (1.7 m/s) speed be implemented for the optimal cleaning configuration. These particular settings minimized product damage and met the targeted performance increase.

7.0 RECOMMENDATIONS

For future developments based on this project, the following recommendations should be considered:

1. A particle generation method that accounts for the natural deflection of leaves is required to improve the simulated behaviour of leaves.
2. A bonding method of attaching the petioles to the leaves to increase the accuracy of the simulations.
3. Incorporating complete bunches of grapes with stems to replicate more realistic conditions. Ideally, the grapes should be able to separate from the stem when subjected to excess forces.
4. A dynamics coupling in DEM software that allows the ribs to elastically deform instead of maintaining a rigid form when rotating about the roller axis.
5. Additional testing for the physical characteristics and biological properties to obtain a consist number of trials for each experiment and location.
6. Increase the number of experimental conveyor and aspirator trials to validate the DEM simulations.
7. Develop and compare other crop flow simulations from different grape varieties.

8.0 REFERENCES

Alsina, M. M., F. De Herralde, X. Aranda, R. Save, and C. Biel. 2007. Water relations and vulnerability to embolism are not related : Experiments with eight grapevine cultivars. *Vitis* 46(1): 1-6.

Aoki, T. 2014. Large-scale granular and fluid (DEM/SPH) simulations using particles. Tokyo Institute of Technology. *In SC14 NVIDIA Booth Talk*, New Orleans.

ASTM International. 2013. G115-10-Standard guide for measuring and reporting friction coefficient.

ASTM International. 2014. D3464-96-Standard test method for average velocity in a duct using a thermal anemometer.

Bartowsky, E.J. 2008. Bacterial spoilage of wine and approaches to minimize it. *Journal of Applied Microbiology* 48 (2): 149-156.

Berthet, J.-P. 2010. Separator device and cleaning system for a stream harvested by a fruit harvesting machine. U.S. Patent No. 2010/0132326.

Bisson, L.F., A.L. Waterhouse, S.E. Ebeler, M.A. Walker, and J.T. Lapsley. 2002. The present and future of the international wine industry. *Nature* 418: 696-699.

Boerner, M. 2011. Discrete Element Method (DEM). NaWiTec, Institute of Process Engineering. Otto-von-Guericke University Magdeburg. Available at: http://www.ovgu.de/ivt/tvt/media/6a3a9decbbafe2b/dem_skript_englisch.pdf Accessed October 2015.

Caliaro, M., F. Schmich, T. Speck, and O. Speck. 2013. Effect of drought stress on bending stiffness in petioles of Caladium Bicolor (Araceae). *American Journal of Botany* 100 (11): 2141-2148.

Chaudhuri, B., F.J. Muzzio, and M.S. Tomassone. 2006. Modeling of heat transfer in granular flow in rotating vessels. *Chemical Engineering Science* (61): 6348-6360

Christensen, L.P., A.N. Kasimatis, J.J. Kissler, F. Jensen, and D.A. Luvisi. 1973. Mechanical harvesting of grapes for the winery. Agricultural Extension: University of California.

CIVC. 2012. Comité interprofessionel du vin de Champagne. Chaque vendange est unique. Available at: http://www.champagne.fr/ Accessed 3 February 2015.

Cleary, P., M. Prakash, M.D. Sinnott, M. Rudman, and R. Das. 2011. Large scale simulation of industrial, engineering and geophysical flows using particle methods.

Cleary, P. W. 2004. Large scale industrial DEM modelling. *Engineering Computations* 22: 169-204

Cleary, P.W. 2009. Industrial particle flow modelling using DEM. *Engineering Computations* 26: 698-743.

Coetzee, J. C. and S. G. Lombard. 2013. The destemming of grapes: experiments and discrete element modelling. *Biosystems Engineering* 114 (2013): 232-248.

Crane Company. 1988. Flow of fluids through valves, fittings, and pipe. Technical Paper No. 410 (TP 410)

Crawley, M. J. 2013. *The R Book.* 2nd ed. Chichester, United Kingdom: John Wiley and Sons, Ltd.

Creaform®. 2015. Technical Specifications: HandysSCAN 3D Handheld 3D Scanner. http://www.creaform3d.com/en/metrology-solutions/products/portable-3d-scanner/technical-specifications-handyscan-3d Accessed August 27th 2015.

Cundall, P. A. and O. D. L. Strack. 1979. A Discrete Numerical Model for Granular Assemblies. Géotechnique. 29(1): 47-65.

DEM Solutions®. 2014. EDEM® Software Theory Reference Guide. Version 2.6. Edinburgh, UK: DEM Solutions®

DEM Solutions®. 2015. EDEM® Software User Guide. Version 2.7. Edinburgh, UK: DEM Solutions®

Duncan, A. and D. Greenaway. 2008. The economics of wine: introduction. *The Economic Journal 118* (529): 137-141.

Faisal, T. R., E.M. Khalil Abad, N. Hristozov, and D. Pasini. 2010. The impact of tissue morphology, cross-section and turgor pressure on the mechanical properties of the leaf petiole in plants. *Journal of Bionic Engineering* 7: 11-23.

Farinas, M. D., D. Dancho-Knapik, J.J. Peguero-Pina, E. Gil-Pelegrin, and T. E. Gomez Alvarez-Arenas. 2013. Shear waves in vegetal tissues at ultrasonic frequencies. *Applied Physics Letters* 102 (103702): 1-5.

Ferrandex, J. 1999. Machine for stemming grapes before making wine. E.U. Patent No. 1002467.

Gaviglio, C. and E. Vinsonneau. 2007. Machine à vendanger: bonne pratique de récolte. Institut Français de la Vigne et du Vin. Available at : http://www.vignevin.com/fileadmin/users/ifv/publications/A_telecharger/Itin15_MachVendanger_BD.pdf Accessed 3 February 2015.

Gialis, J., and R. Pellenc. 2009. Linear stalk separator with alternating oscillating movements. U.S. Patent No. 2009/0056297.

Gialis, J., and R. Pellenc. 2012. Sorting table featuring grading rolls with modifiable and adjustable gaps, and machines and installations making use thereof. U.S. Patent No. 2012/0131894.

Gokbayrak, Z., and G. Soylemezoglu. 2010. Grapevine throughout the history of Anatolia. *International Journal of Botany* 6: 465-472.

Goode, J. 2014. Whole bunches and stems in winemaking. Wineanorak. Available at: http://www.wineanorak.com/wholebunch.htm Accessed 2 February 2015.

Gregoire. 2014. Same Deutz-Fahr. Wine Growing Products: Harvesters. Available at: https://www.gregoiregroup.com/index_uk.html Accessed May 2014 and January 2015.

Grima, A. and P. W. Wypych. 2011. Development and validation of calibration methods for discrete element modelling. *Granular Matter* (13): 127-132.

Henderson , S. M. 1952. A basic concept of equilibrium moisture. *Agricultural Engineering* 33(1): 29-33

Humboldt Mfg. Co. 2015. Soil-LAB: Pneumatic Direct/Residual Shear Apparatus. Available at: http://www.humboldtmfg.com/pneumatic_directresidual_shear_apparatus.html Accessed January 2015.

IEEE CSS. 2005. Deflections and slopes of beams. IEEE Control System Society Technical Committee on Computer-Aided Control System Design. Available at: http://virtual.cvut.cz/beams/. Accessed 9 November 2015.

Insel, B. 2008. The U.S. wine industry. *Business Economics* 43(1): 68-73.

Itasca Consulting Group (ICG), Inc. 1999. PFC^{3D} (Particle Flow Code) Version 2.0 Theory and Background Manual. Minneapolis, Minnesota.

Johnson, H. 1989. *Vintage: The Story of Wine.* Mitchell Beazley, London.

Johnson, K., K. Kendall, and A. Roberts. 1971. Surface energy and the contact of elastic solids. In Proc. Royal Society of London- Series A, *Mathematical and Physical*, (324) 301–313.

Johnson, S. 1977. Mechanical harvesting of wine grapes. U.S. Department of Agriculture. Agricultural Economic Report No. 385.

Jones, G.V., M.A. White, O.R. Cooper, and K. Storchmann. 2005. Climate change and global wine quality: climate change. (in press)

Jones, G.V. 2006. Climate and terroir: impacts of climate variability and change on wine. *In Fine Wine and Terroir: The Geoscience Perspective, Geological Association of Canada.* 247 pages.

Lapple, C. E. 1956. *Fluid and Particle Mechanics.* University of Delaware, Newark.

Le Nevé, D., G. Bossard, and J.-P. Berthet. 1997. Conveyor means for use in a fruit harvester. E.U. Patent No. 0893049.

Le Nevé, D. and V. Rico. 2014. Method and system for eliminating residue from a flow of harvest. U.S. Patent No. 2014/0221060.

Mackenzie, D.E., and A.G. Christy. 2005. The role of soil chemistry in wine grape quality and sustainable soil management in vineyards. *Water Science and Technology* 51(1): 27-37.

Maury, C., E. Madieta, M. Le Moigne, E. Mehinagic, R. Siret, and F. Jorjon. 2009. Development of a mechanical texture test to evaluate the ripening process of Cabernet Franc grapes. *Journal of Texture Studies* 40: 511-535.

McKyes, E. 1985. *Soil Cutting and Tillage.* Amsterdam, The Netherlands: Elsevier Science Publishers B.V.

Mérant, J.-C. 2002. Cleaning arrangement for a fruit harvesting machine. E.U. Patent No. 1336333.

Mindlin, R.D. and H. Deresiewicz. 1953. Elastic spheres in contact under varying oblique forces. PhD Dissertation. Columbia University, Engineering.

Mohsenin, N. N. 1984. *Physical Properties of Plant and Animal Materials.* New York, N.Y.: Gordon and Breach Science Publishers.

Morris, J.R. 1983. Effects of mechanical harvesting on the quality of small fruits and grapes. *American Society of Agriculture Engineers* 5(84): 332-348.

Mullins, M.G., A. Bouquet, and L.E. Williams. 1992. *Biology of the Grapevine.* Great Britain: Cambridge University Press.

Munjiza, A., T. Carney, E. Knight, R.P. Swift, D. Greening, and D. Steedman. 2008. The Roots of possible chaotic behaviour in modelling and simulation of discontinua. In Proc. of 6th International Conference on Computation of Shell and Spatial Structures. Cornell University, Ithaca, NY, USA.

Nakas, C. and C. Dufurne. 2009. Method for eliminating leaf stalks from a harvested stream. E.U. Patent No. 2348808.

New Holland-Braud. 2014. CNH Industrial: New Holland Agriculture Division. Available at: http://agriculture.newholland.com/france/fr/Products/Grape/Pages/products_selector.aspx Accessed May 2014 and January 2015.

Niero, R. and R. Pellenc. 2011. Machine de tri sélectif de récolte, et chaine de tri comprenant une telle machine. E.U. Patent No. 2188067.

Olmo, H.P. 1961. *Wines and Vines* 41:27-28.

Oxbo-Korvan. 2014. Oxbo International Corporation: Vineyard Product Line-Wine, Juice and Raisin Harvesters. Available at: http://www.oxbocorp.com/Products/Vineyard/GrapeHarvesters.aspx Accessed May 2014 and January 2015.

Pellenc. 2014. Pellenc Group: Agriculture Division. Available at: http://www.pellenc.com/agriculture/en/ Accessed May 2014 and January 2015.

Pellenc, R. 2009. Table de tri à rouleaux trieurs, pour l'élimination des corps étrangers restant mêlés aux produits de la récolte de petits fruits. E.U. Patent No. 2030498.

Pezzi, F., C. Caprara, and F. Bordini. 2008. Transmission of impacts during mechanical grape harvesting and transportation. *Journal of Agricultural Engineering* 3: 43-48.

Potyondy, D.O. and P.A. Cundall. 2004. A bonded-particle for rock. *International Journal of Rock Mechanics and Mining Science* (41): 1329-1364.

Prescott, J.A. 1965. The climatology of the vine (*Vitis vinifera L.*) the cool limits of cultivation. Royal Society of Southern Australia: Transcripts 89: 5-23.

Sakaguchi, E., E. Ozaki, and T. Igarashi. 1993. Plugging of the flow of granular materials during the discharge from a silo. *International Journal of Modern Physics.* B7: 1946-1963.

Sallis, P., Jarur, M., and Trujillo, M. 2009. Frost Prediction Characteristics and Classification using Computational Neural Networks. *Australian Journal of Intelligent Information Processing Systems* 10 (1): 50-58.

Schiller, L. 1932. *Handbunch der Experiemental-Physik.* Vol. IV, Part 2, pp. 337-387. Akademische Verlagsgesellschaft, Leipzig.

Seguin, G. 1988. Ecosystems of the great red wines produced in the maritime climate of Bordeaux. In Proc. *Symposium on Maritime Climate Winegrowing*. Geneva, NY: Department of Horticultural Sciences, Cornell University.

Simion, A. I., P.E. Dobrovici, L. Rusu, and L. Gavrila. 2011. Modeling of the thermo-physical properties of grapes juice III. Viscosity and Heat Capacity. In International Conference of Applied Sciences, Chemistry and Chemistry Engineering, 409-420. Bacau, Romania: University of Bacau.

Sitkei, G. 1986. *Mechanics of Agricultural Materials.* 1st ed., chapter 14. New York. Elsevier Science.

Srivastava, A.K., C.E. Goering, R.P. Rohrbach, and D.R. Buckmaster. 2006. Engineering of agricultural machines. 2nd ed. St. Joseph, MI.: ASAE Publication 801M0206.

Stroshine, R. 1998. *Physical Properties of Agricultural Materials and Food Products*. West Lafayette, Indiana: Richard Stroshine.

Studer, H.E. 2000. *Raisin Harvest Mechanization: A Bit of History. Raisin Production Manual*. University of California. Agricultural and Natural Resources Publication 3393. Chapter 32: 245-251.

Studer, H.E. and H.P. Olmo. 1969. *Mechanical Harvesting of Grapes in California: Cultural Practices and Machines*. In Cargill and Rossmiller. pp. 611.

ThirtyFifty. 2014. Map: Wine producing regions of the world. Climate Change and Wine Overview. Available at: http://www.thirtyfifty.co.uk/spotlight-climate-change.asp Accessed May 2014.

Tsuji, Y., T. Tanaka, and T. Ishida. 1992. Lagrangian numerical simulation of plug flow of cohesionless particles in a horizontal pipe. *Powder Technology* (71): 239-250.

Urhausen, S., S. Brienen, A. Kapala, and C. Simmer. 2011. Climatic conditions and their impact on viticulture in the upper Moselle region. *Climatic Changes* 109: 349-373.

Van Leeuwen, C., P. Friant, X. Choné, O. Tregoat, S. Koundouras, and D. Dubourdieu. 2004. Influence of climate, soil, and cultivar on terroir. *American Journal of Enology and Viticulture* 55(3): 207-217.

Van Leeuwen, C., P. Friant, J.P. Soyer, C. Molot, X. Choné, and D. Dubourdieu. 2000. L'Intérêt du dosage de l'azote total et l'azote assimilable dans le moût comme indicateur de la nutrition azotée de la vigne. *Journal International des Sciences de la Vigne et du Vin* 34(1): 75-82.

Van Leeuwen, C., and G. Seguin. 2006. The concept of terroir in viticulture. *Journal of Wine Research* 17(1): 1-10.

Walton, O. 2006. Elastic-plastic contact model. Company Report, DEM Solutions®.

Weast, R. C. 1984. *Chemical Rubber Company (CRC) Handbook of Chemistry and Physics.* 65th ed. CRC Press, Inc. Boca Raton, Florida. USA

Wildenradt, H.L. and A. Jr. Caputi. 1974. Identification of grape leaf compounds in grape must and wine. Annual Meeting: American Society of Enologists. Coronado, California.

Zhou, Y.C., B.H. Xu, A.B. Yu, and P. Zulli. 2002. An experimental and numerical study of the angle of repose of coarse spheres. *Power Technology* 125: 45-54

APPENDIX A

A.1 Physical Property Equations

Sphericity Equation

$$S = \frac{(abc)^{1/3}}{a} \tag{A.1}$$

where,

S = Sphericity index (dimensionless)
a = major diameter (mm)
b = intermediate diameter (mm)
c = minor diameter (mm)

Average Diameter Equation

$$D_{ave} = [abc]^{1/3} \tag{A.2}$$

where,

D_{ave} = Average diameter (mm)

Coefficient of Static Friction Equation

$$\mu_{static} = \tan\theta \tag{A.3}$$

where,

μ_{static} = Static coefficient of friction (dimensionless)
θ = Slope of friction angle (degrees)

Coefficient of Restitution Equation

$$C_R = \sqrt{\frac{h}{H}} \tag{A.4}$$

where,

C_R = Coefficient of restitution (dimensionless)
h = Bounce height (mm)
H = Drop height (mm)

General Equation for Drag Coefficient (Mohsenin, 1984)

$$C = \frac{2W(\rho_p - \rho_f)}{V_t^2 A_p \rho_p \rho_f} \tag{A.5}$$

where,

C = Drag coefficient (dimensionless)
ρ_p = Particle density (kg/m^3)
ρ_f = Fluid density (kg/m^3)
A_p = Projected area normal to direction of motion (m^2)
W = Mass of particle (kg)
V_t = Terminal velocity (m/s)

Surface Area of Sphere Equation

$$A_{sphere} = 4\pi r^2 \tag{A.6}$$

where,

A_{sphere} = Surface area (mm^2)
r = Mean radius (mm)

Surface Area of Cylinder

$$A_{cylinder} = 2\pi rh + 2\pi r^2 \tag{A.7}$$

where,

$A_{cylinder}$ = Surface area (mm^2)
r = Mean radius (mm)
h = Height (mm)

Porosity

$$\emptyset = 1 - \frac{\rho_{bulk}}{\rho_{particle}} = \frac{V_V}{V_T} \tag{A.8}$$

where,

ϕ = Porosity (dimensionless)
ρ_{bulk} = Bulk density (kg/m^3)
$\rho_{particle}$ = Particle density (kg/m^3)
V_V = Void volume
V_T = Total/bulk volume

Bulk Density Equation

$$\rho_{bulk} = \frac{m_{total}}{V_{total}} \tag{A.9}$$

where,

ρ_{bulk} = Bulk density (kg/m^3)
m_{total} = Total bulk mass (kg)
V_{total} = Total bulk volume (m^3)

Particle Density Equation

$$\rho_{particle} = \frac{m_{particle}}{V_{calculated}} \quad \text{(A.10)}$$

where,

$\rho_{particle}$ = Particle density (kg/m^3)
m_{total} = Mass of individual particle (kg)
V_{total} = Calculated volume of particle (m^3)

Shear Cell Based Equations (McKyes, 1985)

$$\tau = c + \sigma_n \tan \emptyset \quad \text{(A.11)}$$

where,

τ = Shear strength (Pa)
c = Cohesion (Pa)
σ_n = Normal pressure on internal shear surface (Pa)
ϕ = Angle of internal friction (rad)

$$\mu_i = \tan \emptyset \quad \text{(A.12)}$$

where,

μ_i = Coefficient of internal friction (dimensionless)
ϕ = Angle of internal friction (rad)

Dynamic Viscosity of Grape Juice (Simion *et al.*, 2011)

$$\mu = \mu_{water} \cdot exp\left[\frac{\left(-0.24 + \left({}^{1821.45}/_{T}\right)^{\circ}Bx\right)}{100 - \left((0.86 + 0.000441T)^{\circ}Bx\right)}\right] \quad \text{(A.13)}$$

where,

μ: Dynamic viscosity (Pa·s)
T: Absolute temperature (K)
◦Bx: Degress brix (g of sugar/100 g solution)

A.2 Parallax Compensation

Coefficient of Restitution

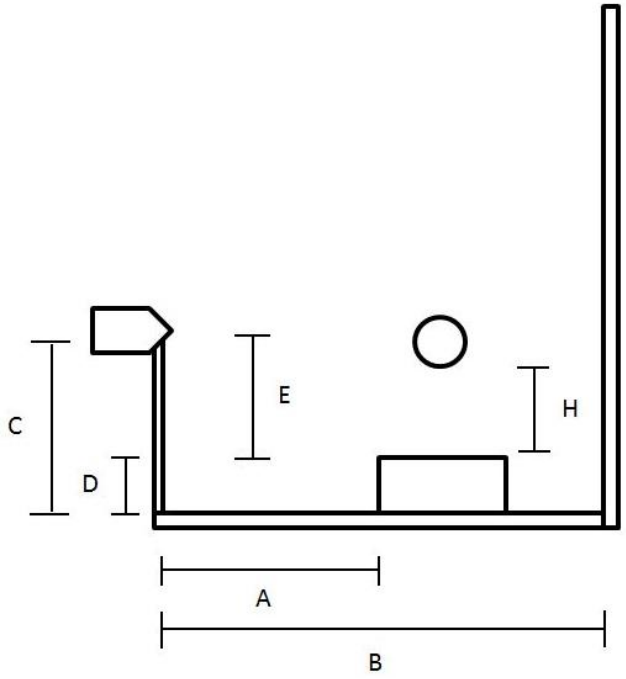

Figure A.1. Configuration schematic of coefficient of restitution platform.

When H>=E:

$$H_{adjusted} = E + \left[\left(abs(E - H)\right) \times \frac{A}{B}\right] \quad \text{(A.14)}$$

When H<E:

$$H_{adjusted} = E - \left[\left(abs(E - H)\right) \times \frac{A}{B}\right] \quad \text{(A.15)}$$

where,

A = 145mm
B = 210mm
C = 52mm
D = Varies with surface setup
E = C-D
H = Bounce height

Conveyor

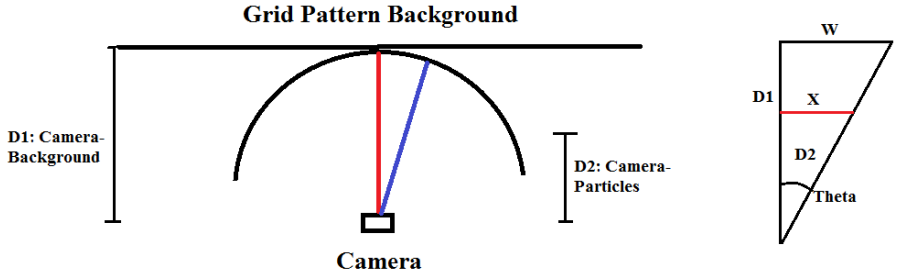

Figure A.2. Configuration schematic of conveyor grid pattern.

$$\frac{X}{D2} = \tan\theta \tag{A.16}$$

$$\frac{W}{D1} = \tan\theta \tag{A.17}$$

$$X = \frac{D2 \cdot W}{D1} \tag{A.18}$$

where,

W = Grid distance (seen)
X = Actual grid distance
D1 = Distance between camera and grid background
D2 = Distance between camera and projected particles
θ = Working angle between D1 and line of sight

A.3 Terminal Velocity Determination

Conical Wind Column Compensation

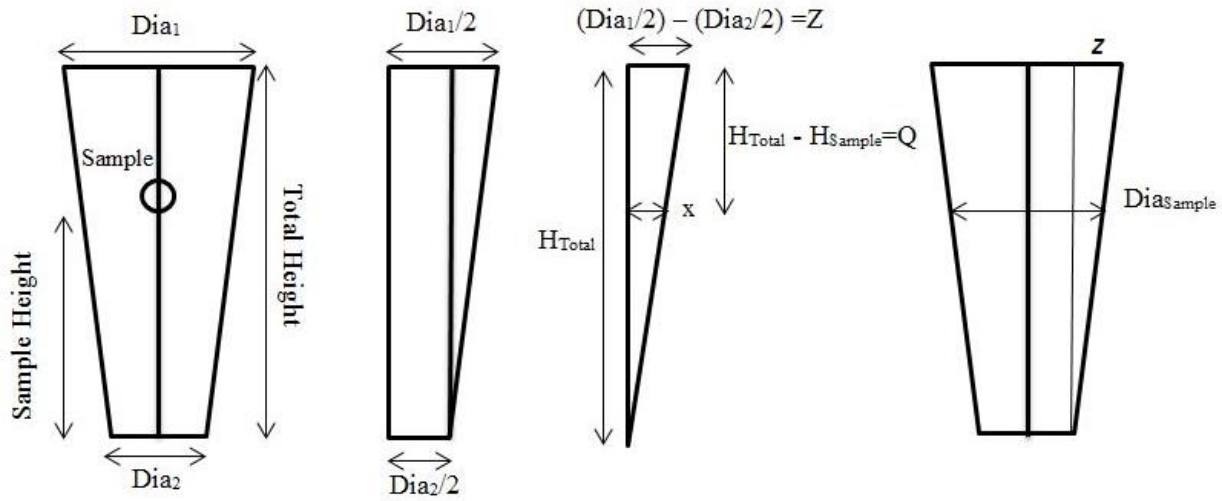

Figure A.3. Calculation schematic for terminal velocity calculation.

By using similar triangles: the diameter of the cross sectional area at the height of the sample:

$$\frac{x}{Q} = \frac{Z}{H_{Total}} \tag{A.19}$$

$$x = \frac{ZQ}{H_{Total}} \tag{A.20}$$

$$Dia_{Sample} = \left(\frac{Dia_1}{2} - x\right) \times 2 \tag{A.21}$$

Using the ratio of diameter 2 and the diameter at the sample height

$$Terminal\ Velocity = V_o \times \left(\frac{Dia_2}{Dia_{Sample}}\right) \tag{A.22}$$

where,

V_o = Inlet velocity at the bottom of the conical wind column (point with greatest velocity)

Calculating Aerodynamic Properties

The general equations for the Reynolds number (N_R), the drag coefficient (C), and terminal velocity (V_t) are as follows:

$$N_R = \frac{\rho_f V_t D}{\eta} \tag{A.23}$$

$$C = \left[\frac{2W(\rho_p - \rho_f)}{V_t^2 \rho_p \rho_f A_p}\right] \tag{A.24}$$

$$V_t = \left[\frac{2W(\rho_p - \rho_f)}{\rho_p \rho_f A_p C}\right]^{1/2} \tag{A.25}$$

where,

N_R = Reynolds number (N kg m/s^2)
C = Drag coefficient (dimensionless)
V_t = Terminal velocity (m/s)
D = Effective dimension (m)
η = Dynamic viscosity or absolute viscosity (kg/m·s or Pa·s)
W = Particle mass (kg)
A_p = Particle projected area (m^2)
d_p = Particle diameter (m)
ρ_f = Fluid density (kg/m^3)
ρ_p= Particle density (kg/m^3)
g = Gravitational acceleration (9.81 m/s^2)

Table A.1 shows the general equations modified with respect to the flow direction and geometrical shapes of the particles.

Table A.1. Equations of motion of spheres, disks, and circular cylinders (Adopted from Lapple, 1956).

	Sphere (any direction[1])	Thin disk (normal to face[1])	Thin disk (parallel to face[1])	Infinite circular cylinder (normal to axis[1])
Reynolds No. equ.	$d_p V \rho_f / \eta$	$d_p V \rho_f / \eta$	$2LV\rho_f/\eta$	$d_p V \rho_f / \eta$
Frontal area A_p	$(\pi/4)d_p^2$	$(\pi/4)d_p^2$	$(d_p)L$	$(d_p)K$
Mass m_p	$\rho_p(\pi/6)d_p^3$	$\rho_p(\pi/4)d_p^2L$	$\rho_p(\pi/4)d_p^2L$	$\rho_p(\pi/4)d_p^2L$
Drag relationships				
streamline flow				
$N_R<0.2, F_D=$	$3\pi\eta V d_p$	$8\eta V d_p$	$(16/3)\eta V d_p$	$(4\pi/K)\eta VL$
$C_D N_R=$	24	$64/\pi$	64/3	$8\pi/K$
turbulent flow				
C_D (average)	0.44	1.12	—	1.2
N_R (range)	$1\times10^3-2\times10^5$	>1000	—	$1\times10^2-2\times10^5$
Terminal velocity V_t^2	$\frac{4gd_p(\rho_p-\rho_f)}{3C\rho_f}$	$\frac{2gL(\rho_p-\rho_f)}{C\rho_f}$	$\frac{gd_p(\rho_p-\rho_f)}{2C\rho_f}$	$\frac{gd_p(\rho_p-\rho_f)}{2C\rho_f}$

[1] Direction of flow or motion.
L = Thickness of disk, length of rod or cylinder, length of flat plate along direction of flow or motion
$K = 2.002 \ln N_R$

The effective dimension (D) and the projected area (A_p) terms in the equations are dependent on the particle physical shape with respect to the air stream. When theoretically determining the terminal velocity, both the Reynolds number (N_R) and drag coefficient (C) include a terminal velocity (V_t) term, which requires a trial and error approach (Mohsenin, 1984). By using the CN^2_R or C/N_R graphs, the Reynolds number can be found and then used for a better approximation of both the terminal velocity and drag coefficient (Mohsenin, 1984). This particular method is preferable as it also applies to irregularly shaped particles. The explanatory variables (CN^2_R or C/N_R) on the graphs can be calculated as follows:

$$C N_R^2 = \frac{2 g \rho_f d_p^3 (\rho_p - \rho_f)}{3 \eta^2} \quad \text{(A.26)}$$

$$C/N_r = \frac{4 g \eta (\rho_p - \rho_f)}{3 \rho d_f^2 V_t^3} \quad \text{(A.27)}$$

$$C N_R^2 = \frac{8 W \rho_f (\rho_p - \rho_f)}{\pi \eta^2 \rho_p} \quad \text{(A.28)}$$

Equations A.26 and A.27 apply to only spherical particles and equation A.28 to any form of particle (sphere, plate, cube, rounded body, and round plate). Figure A.4 to Figure A.6 are used to determine the Reynolds number for particles that may be spherical, rounded, cubic, plated, or round plated. Figure A.7 is then used to find the drag coefficient, which can also be applied to equation 1 for the terminal velocity.

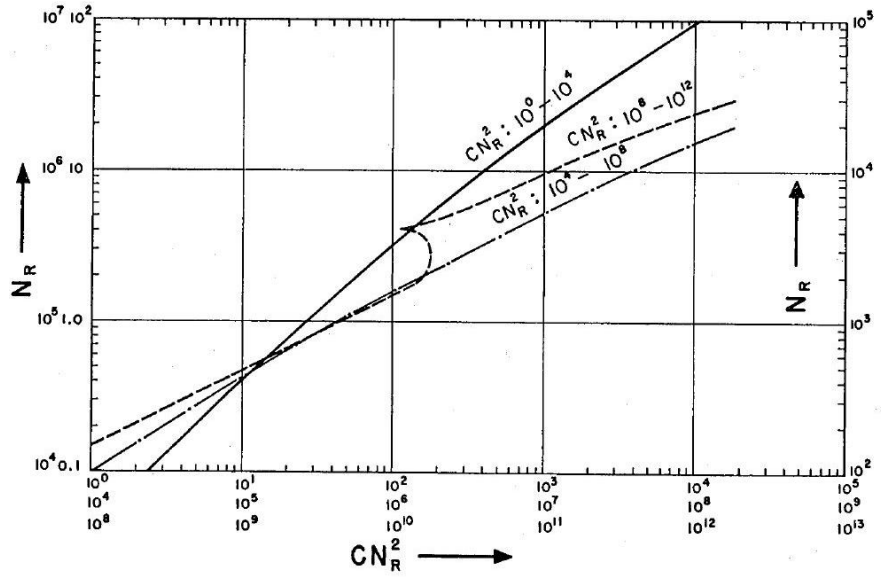

Figure A.4. Graphical relationship between Reynolds number (N_R) and CN_R^2 for spherical particles (Schiller, 1932).

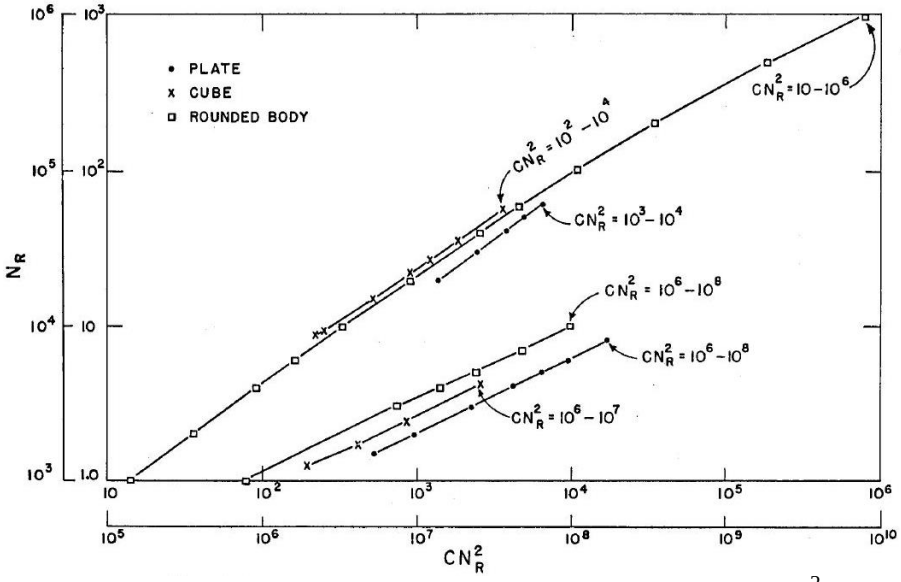

Figure A.5. Graphical relationship between Reynolds number (N_R) and CN_R^2 for plates, cubes, and rounded particles (Lapple, 1956; Henderson and Perry, 1952).

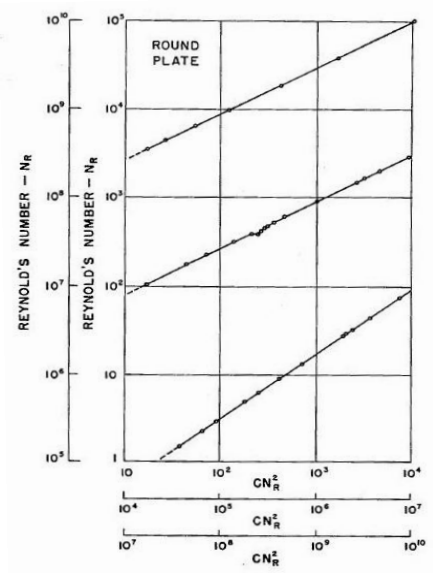

Figure A.6. Graphical relationship between Reynolds number (N_R) and CN_R^2 for round plates (Schiller, 1932).

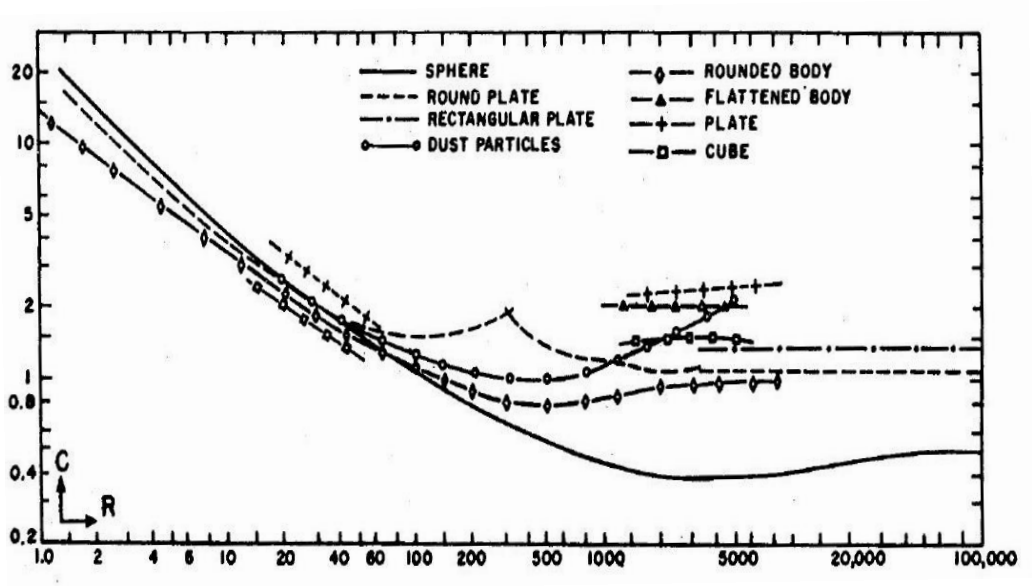

Figure A.7. Graphical relationship between Reynolds number (N_R) and drag coefficient for plates (Schiller, 1932).

Dynamic Viscosity of Air (Crane, 1988 and Weast, 1984)

$$\mu = \mu_o \frac{a}{b}\left(\frac{T}{T_o}\right)^{3/2} \tag{A.29}$$

$$a = 0.555T_o + C \tag{A.30}$$

$$b = 0.555T + C \tag{A.31}$$

where,

μ = Dynamic (absolute) viscosity (Pa·s)
μ_o = Reference viscosity (Pa·s)
T = Input temperature (◦R)
T_o = 524.07 – Reference temperature (◦R)
C = 120 – Sutherland's constant (dimensionless)

Density of Air

$$\rho_{air} = \frac{\left(\frac{P}{R_a \cdot T}\right)(1 + SH)}{\left(\frac{1 + SH \cdot R_w}{R_a}\right)} \tag{A.32}$$

where,

ρ_{air} = Moist air density (kg/m^3)
SH = Specific humidity of air vapor mixture (kg/kg)
P = Atmospheric pressure (Pa)
T = Input temperature (K)
R_a = 286.9 – Individual gas constant of air (J/kg·K)
R_w = 461.5 – Individual gas constant of water vapor (J/kg·K)

A.4 Derivation of Analytical Model Trajectory

The following derivation is based on the Sitkei (1986) conveying by throwing equations for fertilizer particles:

The initial velocity of the particles is simplified in the respective horizontal and vertical components:

$$v = \sqrt{\dot{x}^2 + \dot{y}^2} \tag{A.33}$$

where,

v = Initial velocity (m/s)
$\dot{x}$ = Velocity horizontal component (m/s)
$\dot{y}$ = Velocity vertical component (m/s)

The following equation accounts for the drag force of a given object:

$$W = \frac{c_w A_p v^2 \rho_a}{2} \tag{A.34}$$

where,

W = Object drag force (N)
c_w = Drag coefficient (dimensionless)
A_p = Particle projected area (m^2)
v = Initial velocity (m/s)
ρ_a = Air density (kg/m^3)

The drag force is simplified in both its horizontal and vertical components:

$$W_x = W \cos \alpha \tag{A.35}$$

$$W_y = W \sin \alpha \tag{A.36}$$

where,

W = Object drag force (N)
W_x = Object drag force horizontal component (N)
W_y = Object drag force vertical component (N)
α = Conveyor angle (^{0})

Further simplification of the horizontal and vertical components:

$$\cos\alpha = \frac{\dot{x}}{v} \tag{A.37}$$

$$\sin\alpha = \frac{\dot{y}}{v} \tag{A.38}$$

The second law of Newton is used for the force balance for the horizontal component, which excludes the effect of gravity.

$$m\ddot{x} = -W_x = \frac{-Kv^2\dot{x}}{v} \tag{A.39}$$

$$m\ddot{x} = -K\dot{x}\sqrt{\dot{x}^2 + \dot{y}^2} \tag{A.40}$$

where,

ẍ = Acceleration horizontal component (m/s^2)

where,

$$K = \frac{c_w A_p \rho_a}{2} \tag{A.41}$$

A similar force balance for the vertical component includes the effect of gravity.

$$m\ddot{y} = -K\dot{y}\sqrt{\dot{x}^2 + \dot{y}^2} - mg \tag{A.42}$$

where,

ÿ = Acceleration vertical component (m/s^2)
g = Gravitational acceleration (9.81 m/s^2)

Equations A and B are simplified into the following equations:

$$\ddot{x} = -\frac{K}{m}\dot{x}\sqrt{\dot{x}^2 + \dot{y}^2} \tag{A.43}$$

$$\ddot{y} = -\frac{K}{m}\dot{y}\sqrt{\dot{x}^2 + \dot{y}^2} - g \tag{A.44}$$

The double integration of the previous equations results in the following horizontal and vertical positioning equations:

$$x(t) = \frac{m}{K}v\left(1 - e^{\frac{-K}{m}t}\right)\cos\alpha \tag{A.45}$$

$$y(t) = \frac{m}{K}\left(\frac{mg}{K} + v\sin\alpha\right)\left(1 - e^{\frac{-K}{m}t}\right)\cos\alpha - \frac{mg}{K}t \tag{A.46}$$

where,

x = Horizontal displacement (m)
y = Vertical displacement (m)

APPENDIX B

B.1 Additional Physical Property Testing

Porosity Measurements

The porosity of the biological materials was determined using a 200 ml glass beaker. Each material was placed into the beaker until the 200 ml level was attained. The material mass was then recorded by the digital scale (KERN CKE 2000-2) as seen in Figure B.1. Water was introduced into the glass beaker to fill the void spaces of the 200 ml volume. The new mass was recorded and used to calculate to total void space. These measurements provided the necessary information to calculate the porosity of each material (eq. A.8).

Figure B.1. Measuring grape porosity using a glass beaker.

Separation Force

To characterize the bond strength between the biological materials, the axial force (N) required to separate two elements was determined. A digital force gauge (SAUTER Model FK 100, Balingen, Germany) was used to measure the separation force. Four bond strengths were evaluated between the biological materials: grape-grape stem, grape stem (large segment)-grape stem (small segment), leaf-petiole, and vine shoot-petiole. The samples were secured using a steel wire, which could be wrapped around the biological material and attached to the force gauge hook (Figure B.2). Once the sample was installed, a tension force was applied by hand until the two materials separated.

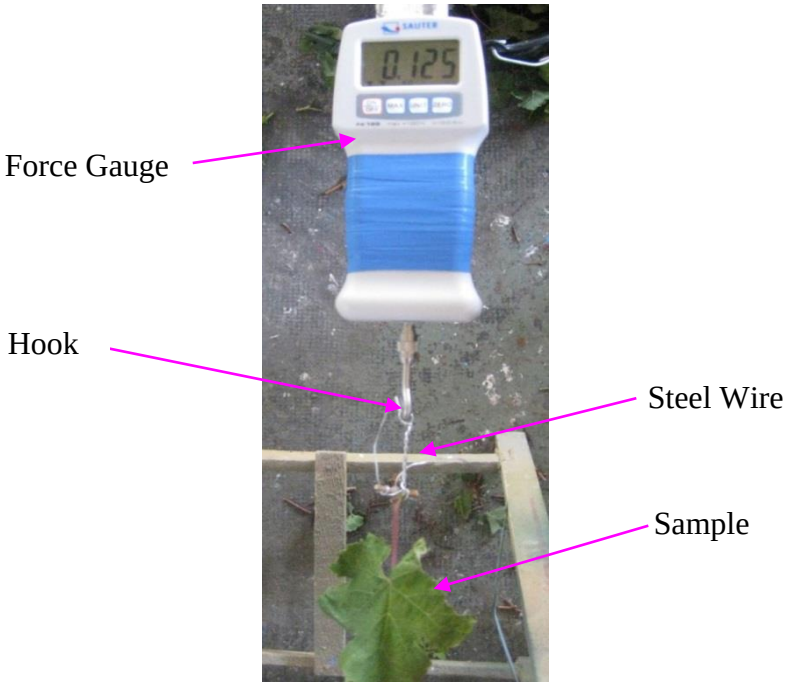

Figure B.2. Experimental apparatus used in measuring the separation between the vine shoot and petiole.

Static Angle of Repose

The static angle of repose provided information on the biological materials in bulk quantities. The testing apparatus consists of a rectangular plexiglass box equipped with a removable side panel. The container width was designed to be approximately 20 times the average diameter of the grapes. This design was based on a similar experimental procedure for the angle of repose conducted by Zhou *et al*. (2002). The large width was to prevent frictional effects between the side walls of the container and the material.

For each trial run, the container would be filled uniformly until completely level. The side panel could then be removed slowly to allow the material to cascade down and create a natural angle of repose. The angle was obtained by using two rulers to measure the opposite and adjacent sides of the right triangle formed by the material. The angle was calculated by taking the inverse tangent of the opposite-adjacent side ratio.

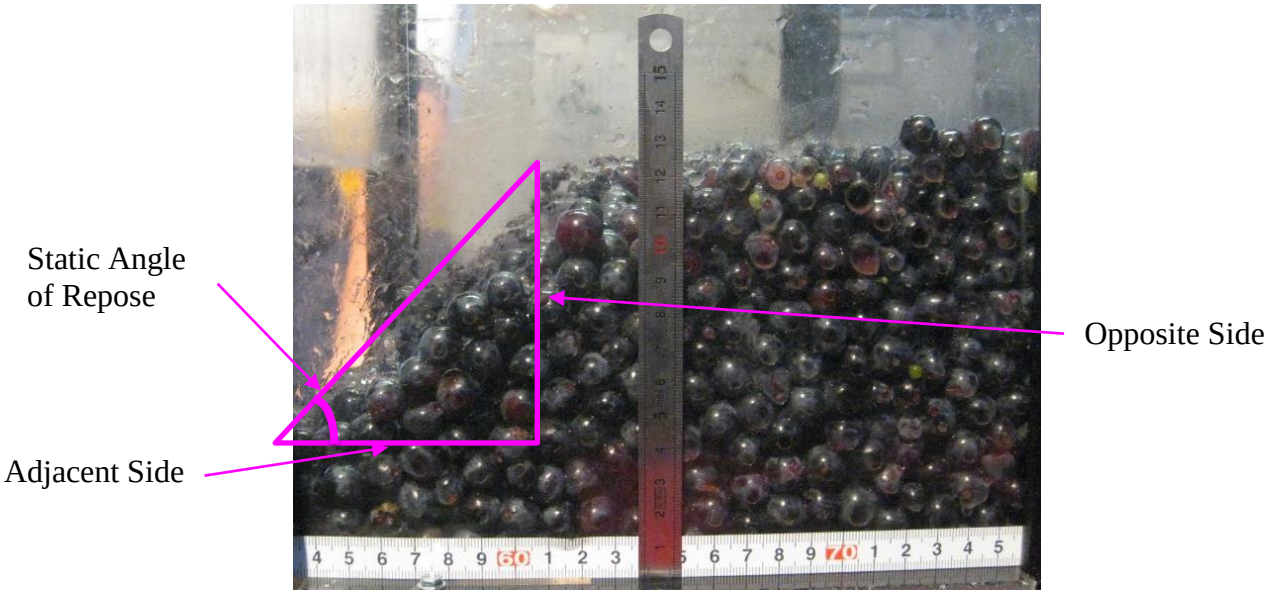

Figure B.3. Grape static angle of repose formed after removing the container side panel.

B.2 Sample Calculation for Single Leaf Deflection

Angle of Deflection (5 mm Cylinder Height)

Test:

Outermost point (42.24, 7.47)

$$0.0044x^2 + 0.01x - 0.4378 \tag{B.1}$$

Angle of Deflection (First Derivation)

$$0.0088x + 0.01 \tag{B.2}$$

$$0.0088(42.24) + 0.01 = 0.38radians = 21.87^{\circ} \tag{B.3}$$

DEM:

Outermost point (42.15, 5.00)

$$0.0019x^2 + 0.0462x - 0.1315 \tag{B.4}$$

Angle of Deflection (First Derivation)

$$0.0038x + 0.0462 \tag{B.5}$$

$$0.0038(42.15) + 0.0462 = 0.21radians = 11.82^{\circ} \tag{B.6}$$

APPENDIX C

C.1 Physical Property Testing Results

Summary Results for the Three Locations

Table C.1. Physical characteristics of biological materials for the Aigues-Mortes location.

Grape	Mean	Std. Dev.	Coef. of Variation	Count	80
Mass (g)	1.25	0.31	24.5%		
Sphericity (%)	98.0	1.26	1.3%		
Average Diameter (mm)	12.57	0.99	7.9%		
True Density (kg WM/m^3)	1177.9	91.0	7.7%		

Leaves	Mean	Std. Dev.	Coef. of Variation	Count
Mass (g)	1.29	0.62	47.9%	60
Leaf Thickness (mm)	0.54	0.08	15.6%	60
True Density (kg WM/m^3)	558.4	165.5	29.6%	51
Leaf Area (mm^2)	4204.5	1924.8	45.8%	51
Leaf Perimeter (mm)	348.5	93.81	26.9%	51

Petioles	Mean	Std. Dev.	Coef. of Variation	Count	50
Mass (g)	0.36	0.26	70.4%		
Average Diameter (mm)	2.29	0.60	26.3%		
True Density (kg WM/m m^3)	1222.3	121.4	9.9%		
Length (mm)	64.11	17.22	26.9%		

Vine Shoot	Mean	Std. Dev	Coef. of Variation	Count	32
Average Diameter (mm)	5.40	0.76	14.1%		
True Density (kg WM/ m^3)	882.6	149.7	17.0%		

Table C.2. Coefficient of restitution of biological materials for the Aigues-Mortes location.

Interaction	Mean	Std. Dev.	Coef. of Variation	n
Grape_on_Grape	0.134	0.017	12.4%	68
Gstem_on_Grape	0.209	0.040	19.3%	54
Shoot_on_Grape	0.157	0.021	13.5%	62
Petiole_on_Grape	0.210	0.057	27.0%	53
Grape_on_Gstem	0.232	0.043	18.7%	51
Gstem_on_Gstem	0.228	0.018	7.9%	27
Shoot_on_Gstem	0.221	0.067	30.1%	37
Petiole_on_Gstem	0.163	0.026	15.9%	25
Grape_on_Leaf	0.357	0.036	10.2%	70
Gstem_on_Leaf	0.293	0.033	11.2%	53
Shoot_on_Leaf	0.315	0.034	10.9%	53
Petiole_on_Leaf	0.283	0.052	18.4%	51
Grape_on_Steel	0.329	0.043	13.0%	30
Gstem_on_Steel	0.244	0.033	13.4%	47
Shoot_on_Steel	0.327	0.046	14.1%	51
Petiole_on_Steel	0.239	0.046	19.2%	32
Grape_on_Mesh	0.259	0.028	10.8%	31
Gstem_on_Mesh	0.251	0.031	12.2%	50
Shoot_on_Mesh	0.227	0.037	16.1%	62
Petiole_on_Mesh	0.263	0.041	15.6%	40
Grape_on_Bucket	0.274	0.030	11.1%	34
Gstem_on_Bucket	0.270	0.034	12.4%	52
Shoot_on_Bucket	0.268	0.050	18.5%	57
Petiole_on_Bucket	0.268	0.068	25.2%	44
Grape_on_Conveyor	0.312	0.033	10.6%	34
Gstem_on_Conveyor	0.266	0.042	15.7%	33
Shoot_on_Conveyor	0.307	0.040	13.1%	58
Petiole_on_Conveyor	0.272	0.057	21.0%	42

Table C.3. Angle of static friction of biological materials for the Aigues-Mortes location.

Interaction	Mean	Std. Dev.	Coef. of Variation	n
Grape-Grape	49.6	8.6	17.3%	60
Gstem-Grape	48.1	7.5	15.6%	60
Gstem-Gstem	43.4	8.7	20.%	52
Grape-Leaf	34.2	6.7	19.5%	39
Gstem-Leaf	42.1	7.7	18.2%	51
Leaf-Leaf	48.0	9.9	20.6%	44
Shoot-Leaf	40.1	10.5	26.1%	49
Petiole-Leaf	30.2	4.7	15.5%	38
Grape-Shoot	28.8	3.9	13.5%	40
Gstem-Shoot	42.5	5.9	13.8%	42
Shoot-Shoot	41.0	8.5	20.7%	50
Grape-Petiole	32.1	3.1	9.8%	30
Gstem-Petiole	46.5	6.9	14.8%	47
Shoot-Petiole	38.4	8.1	21.2%	45
Petiole-Petiole	50.0	9.3	18.6%	50
Grape-Steel	22.0	3.4	15.6%	36
Gstem-Steel	41.0	6.8	16.5%	37
Leaf-Steel	30.2	6.3	20.8%	36
Shoot-Steel	34.4	6.5	18.8%	45
Petiole-Steel	22.1	3.3	14.7%	31
Grape-Mesh	23.0	2.3	10.2%	44
Gstem-Mesh	39.8	9.2	23.0%	46
Leaf-Mesh	41.2	8.9	21.7%	39
Shoot-Mesh	28.2	5.5	19.6%	48
Petiole-Mesh	36.4	6.1	16.6%	48
Grape-Conveyor	47.5	9.6	20.1%	37
Gstem-Conveyor	44.9	8.4	18.6%	43
Leaf-Conveyor	48.4	9.0	18.6%	41
Shoot-Conveyor	42.0	6.9	16.4%	45
Petiole-Conveyor	50.8	10.5	20.8%	53
Grape-Bucket	36.5	6.8	18.5%	40
Gstem-Bucket	48.4	9.8	20.2%	54
Leaf-Bucket	28.2	7.1	25.1%	41
Shoot-Bucket	48.6	9.2	18.9%	58
Petiole-Bucket	47.3	9.1	19.1%	44

Table C.4. Separation force (N) of biological materials for the Aigues-Mortes location.

Interaction	Mean	Std. Dev.	Coef. of Variation	n
Grape-Gstem	2.14	0.88	41.1%	100
Gstem-Gstem	13.63	8.38	61.5%	103
Leaf-Petiole	15.18	6.05	39.8%	103
Shoot-Petiole	21.61	9.53	44.1%	103

Table C.5. Static angle of repose (◦) of grapes for the Aigues-Mortes location.

Material	Mean	Std. Dev.	Coef. of Variation	n
Grape	46.3	5.3	11.5%	15

Table C.6. Aerodynamic characteristics of grapes for the Aigues-Mortes location.

Drag Coefficient (--)	Mean	Std. Dev.	Coef. of Variation	n
Grape	0.275	0.046	16.7%	30
Leaf (disc cut out)	1.909	0.697	36.5%	30
Petiole	0.074	0.034	45.8%	42
Vine Shoot	0.130	0.030	23.5%	44

Terminal Velocity (m/s)	Mean	Std. Dev.	Coef. of Variation	n
Grape	22.71	0.96	4.2%	30
Leaf (disc cut out)	1.88	0.18	9.4%	30
Petiole	12.50	3.63	29.1%	42
Vine Shoot	14.64	1.41	9.6%	44

Table C.7. Physical characteristics of biological materials for the Saint-Gervais location.

Grape	Mean	Std. Dev.	Coef. of Variation	n
Mass (g)	1.64	0.31	18.9%	90
Sphericity (%)	96.3	2.31	2.4%	90
Average Diameter (mm)	13.63	0.83	6.1%	90
True Density (kg WM/m^3)	1223.0	39.6	3.2%	90
Leaf	**Mean**	**Std. Dev.**	**Coef. of Variation**	**n**
Mass (g)	2.46	1.44	58.4%	30
Leaf Thickness (mm)	0.48	0.08	16.6%	30
Petiole	**Mean**	**Std. Dev.**	**Coef. of Variation**	**n**
Mass (g)	0.45	0.30	66.8%	30
Average Diameter (mm)	2.57	0.60	23.4%	30
True Density (kg WM/m^3)	1127.5	109.4	9.7%	30
Length (mm)	69.35	17.05	24.6%	30
Vine Shoot	**Mean**	**Std. Dev.**	**Coef. of Variation**	**n**
Average Diameter (mm)	6.84	0.84	12.3%	30
True Density (kg WM/m^3)	1009.0	35.4	3.5%	30

Table C.8. Bulk characteristics of biological materials for the Saint-Gervais location.

True Density (kg WM/m^3)	Mean	Std. Dev.	Coef. of Variation	n
Grape	1140.5	53.7	4.7%	20
Grape Stem	845.4	75.1	8.9%	3
Porosity	**Mean**	**Std. Dev.**	**Coef. of Variation**	**n**
Grape	0.30	0.03	9.9%	20
Grape Stem	0.87	0.01	1.3%	3

Table C.9. Coefficient of restitution of biological materials for the Saint-Gervais location.

Interaction	Mean	Std. Dev.	Coef. of Variation	n
Grape_on_Grape	0.184	0.016	8.9%	55
Grape_on_Gstem	0.208	0.043	20.8%	31
Grape_on_Leaf	0.334	0.037	11.0%	50
Grape_on_Steel	0.321	0.053	16.4%	57
Grape_on_Mesh	0.303	0.053	17.6%	38
Grape_on_Bucket	0.311	0.034	11.0%	49
Grape_on_Conveyor	0.348	0.049	14.1%	56

Table C.10. Angle of static friction of biological materials for the Saint-Gervais location.

Interaction	Mean	Std. Dev.	Coef. of Variation	n
Grape-Grape	50.2	7.4	14.7%	50
Gstem-Grape	48.9	8.5	17.4%	50
Grape-Leaf	35.5	5.2	14.7%	50
Grape-Shoot	29.1	3.4	11.8%	50
Grape-Petiole	30.4	3.6	11.9%	50
Grape-Steel	31.3	7.5	23.8%	50
Grape-Mesh	22.1	5.0	22.4%	50
Grape-Conveyor	46.8	6.2	13.2%	50
Grape-Bucket	40.6	8.1	20.0%	50

Table C.11. Physical characteristics of biological materials for the Pauillac location.

Grape	Mean	Std. Dev.	Coef. of Variation	n
Mass (g)	1.56	0.30	19.1%	90
Sphericity (%)	96.7	1.7	1.7%	90
Average Diameter (mm)	13.23	0.94	7.1%	90
True Density (kg WM/m^3)	1275.5	44.5	3.5%	90

Leaf	Mean	Std. Dev.	Coef. of Variation	n
Mass (g)	1.5226	0.81	53.5%	50
Leaf Thickness (mm)	0.46	0.06	13.4%	50

Petiole	Mean	Std. Dev.	Coef. of Variation	n
Mass (g)	0.36	0.26	70.4%	50
Average Diameter (mm)	2.29	0.60	26.3%	50
True Density (kg WM/m^3)	1222.3	121.4	9.9%	50
Length (mm)	64.11	17.22	26.9%	50

Vine Shoot	Mean	Std. Dev.	Coef. of Variation	n
Average Diameter (mm)	6.80	1.14	16.8%	50
True Density (kg WM/m^3)	1066.2	55.4	5.2%	50

Table C.12. Physical characteristics of biological materials for the Pauillac location (continued).

True Density (kg WM/m^3)	Mean	Std. Dev.	Coef. of Variation	Location	n
Grape	1077.2	8.8	0.8%	PIC	12
Grape Stem	727.1	128.4	17.7%	PIC	4
Leaf	684.6	29.4	4.3%	PIC	10
Petiole	1016.7	0.3	0.0%	PIC	2
Vine Shoot	1079.3	7.0	0.6%	PIC	4

Porosity	Mean	Std. Dev.	Coef. of Variation	Location	n
Grape	0.41	0.02	4.7%	PIC	12
Grape Stem	0.90	0.04	4.2%	PIC	4
Leaf	0.78	0.04	4.8%	PIC	10
Petiole	0.68	0.04	6.6%	PIC	2
Vine Shoot	0.56	0.07	11.8%	PIC	4

Table C.13. Coefficient of restitution of biological materials for the Pauillac location.

Interaction	Mean	Std. Dev.	Coef. of Variation	n
Grape_on_Grape	0.202	0.028	13.8%	44
Gstem_on_Grape	0.197	0.038	19.4%	34
Shoot_on_Grape	0.167	0.032	19.0%	27
Petiole_on_Grape	0.237	0.058	24.4%	31
Grape_on_Steel	0.345	0.036	10.5%	36
Gstem_on_Steel	0.261	0.040	15.4%	34
Shoot_on_Steel	0.310	0.050	16.2%	40
Petiole_on_Steel	0.280	0.057	20.3%	50
Grape_on_Mesh	0.304	0.040	13.1%	46
Gstem_on_Mesh	0.229	0.034	14.9%	50
Shoot_on_Mesh	0.208	0.036	17.2%	30
Petiole_on_Mesh	0.272	0.061	22.6%	31
Grape_on_Bucket	0.230	0.028	12.2%	40
Gstem_on_Bucket	0.241	0.042	17.5%	50
Shoot_on_Bucket	0.226	0.036	15.9%	35
Petiole_on_Bucket	0.266	0.054	20.2%	36
Grape_on_Conveyor	0.340	0.040	11.6%	37
Gstem_on_Conveyor	0.243	0.045	18.5%	56
Shoot_on_Conveyor	0.285	0.051	17.7%	33
Petiole_on_Conveyor	0.271	0.073	26.9%	41
Grape_on_Shoot	0.267	0.063	23.6%	38
Grape_on_Petiole	0.298	0.048	16.2%	45
Gstem_on_Shoot	0.221	0.041	18.5%	36
Shoot_on_Shoot	0.182	0.032	17.8%	26
Petiole_on_Shoot	0.269	0.074	27.6%	40
Gstem_on_Petiole	0.225	0.045	20.2%	41
Shoot_on_Petiole	0.215	0.052	24.3%	39
Petiole_on_Petiole	0.213	0.065	30.4%	47

Table C.14. Angle of static friction of biological materials for the Pauillac location.

Interaction	Mean	Std. Dev.	Coef. of Variation	n
Grape-Leaf	35.4	4.6	13.0%	40
Gstem-Leaf	45.5	8.4	18.4%	40
Leaf-Leaf	49.2	10.5	21.3%	40
Shoot-Leaf	39.3	8.6	21.9%	38
Petiole-Leaf	34.6	7.5	21.6%	40
Gstem-Shoot	44.7	5.2	11.6%	40
Grape-Petiole	29.8	3.5	11.7%	40
Gstem-Petiole	43.3	6.5	14.9%	40
Shoot-Petiole	32.2	4.1	12.8%	40
Petiole-Petiole	38.2	5.4	14.1%	40
Grape-Steel	34.9	5.8	16.50%	60
Gstem-Steel	43.2	6.4	14.9%	59
Leaf-Steel	31.9	4.7	14.8%	60
Shoot-Steel	30.3	3.7	12.3%	60
Petiole-Steel	30.6	4.4	14.3%	60
Grape-Conveyor	44.8	7.4	16.5%	59
Gstem-Conveyor	40.6	5.6	13.7%	60
Leaf-Conveyor	47.1	8.5	18.1%	60
Shoot-Conveyor	41.4	6.6	15.9%	60
Petiole-Conveyor	49.3	9.0	18.2%	60

Table C.15. Aerodynamic characteristics of grapes for the Aigues-Mortes location.

Drag Coefficient (--)	Mean	Std. Dev.	Coef. of Variation	n
Grape	0.467	0.033	7.0%	30
Leaf (disc cut out)	2.156	0.634	29.4%	30
Petiole	0.163	0.030	18.5%	30
Vine Shoot	0.239	0.051	21.2%	30

Terminal Velocity (m/s)	Mean	Std. Dev.	Coef. of Variation	n
Grape	19.45	0.78	4.0%	30
Leaf (disc cut out)	1.83	0.21	11.4%	30
Petiole	8.46	0.83	9.8%	30
Vine Shoot	11.55	1.24	10.7%	30

ANOVA Results for Physical Properties between the Three Locations

This analysis was conducted using a post-hoc ANOVA test. The Tukey HSD test was employed given the three levels of comparison (three locations). The comparisons with only two available levels were analyzed using an ANOVA test. Below is an example for the code used in the R® software. The tables that follow are the results from the post-hoc ANOVA tests for all the measured physical properties.

```
##Grape Material
model1<-with(subset(Data_1,MATERIAL=="GRAPE"),aov(MASS~LOCATION))
summary(model1)
tuk1<- TukeyHSD(model1)
tuk1
```

Table C.16. Analysis of variance (Tukey HSD Test) results for the mass of biological materials.

Mass (g)					
Grape		diff	lwr	upr	p adj
	PIC-AIG_MRT	0.312556	0.20233	0.422781	0*
	ST_GEV-AIG_MRT	0.389444	0.279219	0.49967	0*
	ST_GEV-PIC	0.076889	-0.03005	0.183824	0.209044
Leaf		diff	lwr	upr	p adj
	PIC-AIG_MRT	0.2326	-0.18337	0.648567	0.383805
	ST_GEV-AIG_MRT	1.174333	0.688588	1.660078	2E-07*
	ST_GEV-PIC	0.941733	0.440058	1.443409	5.26E-05*
Petiole		diff	lwr	upr	p adj
	PIC-AIG_MRT				
	ST_GEV-AIG_MRT				
	ST_GEV-PIC	0.090933	-0.03497	0.216837	0.154467

Table C.17. Analysis of variance (Tukey HSD Test) for the sphericity of grapes.

Sphericity (%)					
Grape		diff	lwr	upr	p adj
	PIC-AIG_MRT	-1.36886	-2.02431	-0.71342	4.5E-06*
	ST_GEV-AIG_MRT	-1.70564	-2.36108	-1.05019	0*
	ST_GEV-PIC	-0.33678	-0.97265	0.299097	0.425789

Table C.18. Analysis of variance (Tukey HSD Test) results for the average diameter of biological materials.

Average Diameter (mm)					
Grape		diff	lwr	upr	p adj
	PIC-AIG_MRT	0.653667	0.323493	0.98384	1.47E-05*
	ST_GEV-AIG_MRT	1.059	0.728827	1.389173	0*
	ST_GEV-PIC	0.405333	0.085018	0.725649	0.008755*
Petiole		diff	lwr	upr	p adj
	PIC-AIG_MRT	0.1152	-0.08873	0.319131	0.377617
	ST_GEV-AIG_MRT	0.3962	0.151106	0.641294	0.000537*
	ST_GEV-PIC	0.281	0.009092	0.552908	0.041018*
Vine Shoot		diff	lwr	upr	p adj
	PIC-AIG_MRT	1.3988	0.878332	1.919268	0*
	ST_GEV-AIG_MRT	1.437	0.852738	2.021262	2E-07*
	ST_GEV-PIC	0.0382	-0.49274	0.569142	0.984019

Table C.19. Analysis of variance (Tukey HSD Test) results for the density of biological materials.

True Density (kg WM/m^3)					
Grape		diff	lwr	upr	p adj
	PIC-AIG_MRT	97.62014	75.36498	119.8753	0*
	ST_GEV-AIG_MRT	45.13858	22.88343	67.39374	8.70E-06*
	ST_GEV-PIC	-52.4816	-74.0722	-30.8909	1.00E-07*
Petiole		diff	lwr	upr	p adj
	PIC-AIG_MRT				
	ST_GEV-AIG_MRT				
	ST_GEV-PIC	-94.8051	-148.634	-40.9766	0.000757*
Vine Shoot		diff	lwr	upr	p adj
	PIC-AIG_MRT	183.619	135.256	231.982	0*
	ST_GEV-AIG_MRT	126.3978	72.10701	180.6886	7E-07*
	ST_GEV-PIC	-57.2212	-106.557	-7.88503	0.018672*

Table C.20. Analysis of variance (Tukey HSD Test) results for the length of petioles.

Length (mm)					
Petiole		diff	lwr	upr	p adj
	PIC-AIG_MRT	15.3089	8.730765	21.88703	4E-07*
	ST_GEV-AIG_MRT	20.55243	12.6465	28.45837	0*
	ST_GEV-PIC	5.243533	-3.52731	14.01438	0.336358

Table C.21. Analysis of variance (Tukey HSD Test) results for leaf thickness.

Thickness (mm)					
Leaf		diff	lwr	upr	p adj
	PIC-AIG_MRT	-0.08553	-0.12011	-0.05096	1E-07*
	ST_GEV-AIG_MRT	-0.063	-0.10338	-0.02262	0.000913*
	ST_GEV-PIC	0.022533	-0.01917	0.064236	0.408692

Table C.22. Analysis of variance (Tukey HSD Test) results for the porosity of biological materials.

Porosity					
Grape		diff	lwr	upr	p adj
	PIC-AIG_MRT				
	ST_GEV-AIG_MRT				
	ST_GEV-PIC	-0.1085	-0.12819	-0.08881	0*
Grape Stem		diff	lwr	upr	p adj
	PIC-AIG_MRT				
	ST_GEV-AIG_MRT				
	ST_GEV-PIC	-0.035	-0.09519	0.025194	0.195235

Table C.23. Analysis of variance (Tukey HSD Test) results for the density of biological materials.

True Density (kg WM/m^3)					
Grape		diff	lwr	upr	p adj
	PIC-AIG_MRT				
	ST_GEV-AIG_MRT				
	ST_GEV-PIC	63.2705	31.15056	95.39044	0.000359*
Grape Stem		diff	lwr	upr	p adj
	PIC-AIG_MRT				
	ST_GEV-AIG_MRT				
	ST_GEV-PIC	118.275	-98.1191	334.6691	0.218998

Table C.24. Analysis of variance (Tukey HSD Test) results for the terminal velocity of biological materials.

Terminal Velocity (m/s)					
Grape		diff	lwr	upr	p adj
	PIC-AIG_MRT	-3.25833	-3.71079	-2.80588	0*
	ST_GEV-AIG_MRT				
	ST_GEV-PIC				
Leaf		diff	lwr	upr	p adj
	PIC-AIG_MRT	-0.04967	-0.14943	0.050102	0.323149
	ST_GEV-AIG_MRT				
	ST_GEV-PIC				
Petiole		diff	lwr	upr	p adj
	PIC-AIG_MRT	-4.03795	-5.38761	-2.68829	1.00E-07*
	ST_GEV-AIG_MRT				
	ST_GEV-PIC				
Vine Shoot		diff	lwr	upr	p adj
	PIC-AIG_MRT	-3.08459	-3.71938	-2.4498	0*
	ST_GEV-AIG_MRT				
	ST_GEV-PIC				

Table C.25. Analysis of variance (Tukey HSD Test) results for the drag coefficient of biological materials.

Drag Coefficient					
Grape		diff	lwr	upr	p adj
	PIC-AIG_MRT	0.192467	0.171903	0.21303	0*
	ST_GEV-AIG_MRT				
	ST_GEV-PIC				
Leaf		diff	lwr	upr	p adj
	PIC-AIG_MRT	0.246633	-0.09766	0.590927	0.156964
	ST_GEV-AIG_MRT				
	ST_GEV-PIC				
Petiole		diff	lwr	upr	p adj
	PIC-AIG_MRT	0.088367	0.072929	0.103804	0*
	ST_GEV-AIG_MRT				
	ST_GEV-PIC				
Vine Shoot		diff	lwr	upr	p adj
	PIC-AIG_MRT	0.10895	0.090162	0.127738	0*
	ST_GEV-AIG_MRT				
	ST_GEV-PIC				

Table C.26. Analysis of variance (Tukey HSD Test) results for the coefficient of restitution of biological materials.

Coefficient of Restitution					
Grape-Grape		diff	lwr	upr	p adj
	PIC-AIG_MRT	0.067844	0.058594	0.077093	0*
	ST_GEV-AIG_MRT	0.049848	0.041178	0.058518	0*
	ST_GEV-PIC	-0.018	-0.02767	-0.00833	5.71E-05*
Grape-Steel		diff	lwr	upr	p adj
	PIC-AIG_MRT	0.015556	-0.01148	0.042586	0.36215
	ST_GEV-AIG_MRT	-0.00838	-0.03304	0.016286	0.700011
	ST_GEV-PIC	-0.02393	-0.04721	-0.00065	0.042405*
Grape-Mesh		diff	lwr	upr	p adj
	PIC-AIG_MRT	0.044608	0.021334	0.067882	4.01E-05*
	ST_GEV-AIG_MRT	0.043801	0.019562	0.068041	0.000111*
	ST_GEV-PIC	-0.00081	-0.02276	0.021149	0.99581
Grape-Bucket		diff	lwr	upr	p adj
	PIC-AIG_MRT	-0.04393	-0.06127	-0.02658	1.00E-07*
	ST_GEV-AIG_MRT	0.037369	0.020771	0.053966	1.30E-06*
	ST_GEV-PIC	0.081298	0.065452	0.097144	0*
Grape-Conveyor		diff	lwr	upr	p adj
	PIC-AIG_MRT	0.028259	0.004291	0.052227	0.016371*
	ST_GEV-AIG_MRT	0.03694	0.015006	0.058875	0.000323*
	ST_GEV-PIC	0.008681	-0.01269	0.030055	0.601289

Table C.27. Analysis of variance (Tukey HSD Test) results for the coefficient of restitution of biological materials (continued).

Coefficient of Restitution					
Grape-Grape Stem		diff	lwr	upr	p adj
	PIC-AIG_MRT				
	ST_GEV-AIG_MRT	-0.02375	-0.04341	-0.00408	0.018569*
	ST_GEV-PIC				
Grape-Leaf		diff	lwr	upr	p adj
	PIC-AIG_MRT				
	ST_GEV-AIG_MRT	-0.02357	-0.03696	-0.01019	0.000686*
	ST_GEV-PIC				
Grape Stem-Grape		diff	lwr	upr	p adj
	PIC-AIG_MRT	-0.01208	-0.02932	0.005156	0.167099
	ST_GEV-AIG_MRT				
	ST_GEV-PIC				
Vine Shoot-Grape		diff	lwr	upr	p adj
	PIC-AIG_MRT	0.00956	-0.00178	0.020901	0.097456
	ST_GEV-AIG_MRT				
	ST_GEV-PIC				
Petiole-Grape		diff	lwr	upr	p adj
	PIC-AIG_MRT	0.027183	0.001483	0.052883	0.038429*
	ST_GEV-AIG_MRT				
	ST_GEV-PIC				
Grape Stem-Steel		diff	lwr	upr	p adj
	PIC-AIG_MRT	0.016874	0.000709	0.033038	0.040977*
	ST_GEV-AIG_MRT				
	ST_GEV-PIC				
Vine Shoot-Steel		diff	lwr	upr	p adj
	PIC-AIG_MRT	-0.01697	-0.03709	0.00315	0.097281
	ST_GEV-AIG_MRT				
	ST_GEV-PIC				
Petiole-Steel		diff	lwr	upr	p adj
	PIC-AIG_MRT	0.04144	0.017622	0.065258	0.000862*
	ST_GEV-AIG_MRT				
	ST_GEV-PIC				

Table C.28. Analysis of variance (Tukey HSD Test) results for the coefficient of restitution of biological materials (continued 2).

Coefficient of Restitution					
Grape Stem-Mesh		diff	lwr	upr	p adj
	PIC-AIG_MRT	-0.0228	-0.03566	-0.00994	0.000663*
	ST_GEV-AIG_MRT				
	ST_GEV-PIC				
Vine Shoot-Mesh		diff	lwr	upr	p adj
	PIC-AIG_MRT	-0.01934	-0.03535	-0.00333	0.018472*
	ST_GEV-AIG_MRT				
	ST_GEV-PIC				
Petiole-Mesh		diff	lwr	upr	p adj
	PIC-AIG_MRT	0.009437	-0.01492	0.03379	0.442124
	ST_GEV-AIG_MRT				
	ST_GEV-PIC				
Grape Stem-Bucket		diff	lwr	upr	p adj
	PIC-AIG_MRT	-0.02965	-0.04456	-0.01474	0.000148*
	ST_GEV-AIG_MRT				
	ST_GEV-PIC				
Vine Shoot-Bucket		diff	lwr	upr	p adj
	PIC-AIG_MRT	-0.04157	-0.06068	-0.02245	4.01E-05*
	ST_GEV-AIG_MRT				
	ST_GEV-PIC				
Petiole-Bucket		diff	lwr	upr	p adj
	PIC-AIG_MRT	-0.00197	-0.02962	0.025675	0.887431
	ST_GEV-AIG_MRT				
	ST_GEV-PIC				
Grape Stem-Conveyor		diff	lwr	upr	p adj
	PIC-AIG_MRT	-0.02304	-0.04214	-0.00395	0.018604*
	ST_GEV-AIG_MRT				
	ST_GEV-PIC				
Vine Shoot-Conveyor		diff	lwr	upr	p adj
	PIC-AIG_MRT	-0.02156	-0.04068	-0.00243	0.027588*
	ST_GEV-AIG_MRT				
	ST_GEV-PIC				

Table C.29. Analysis of variance (Tukey HSD Test) results for the coefficient of restitution of biological materials (continue 3).

Coefficient of Restitution					
Petiole-Conveyor		diff	lwr	upr	p adj
	PIC-AIG_MRT	-0.00059	-0.02912	0.02795	0.967449
	ST_GEV-AIG_MRT				
	ST_GEV-PIC				
Grape-Vine Shoot		diff	lwr	upr	p adj
	PIC-AIG_MRT				
	ST_GEV-AIG_MRT				
	ST_GEV-PIC	0.030473	0.007593	0.053353	0.009603*
Grape-Petiole		diff	lwr	upr	p adj
	PIC-AIG_MRT				
	ST_GEV-AIG_MRT				
	ST_GEV-PIC	0.028245	0.008543	0.047947	0.005466*

Table C.30. Analysis of variance (Tukey HSD Test) results for the friction angle of biological materials.

Friction Angle (◦)					
Grape-Leaf		diff	lwr	upr	p adj
	PIC-AIG_MRT	1.252821	-1.69642	4.202065	0.573514
	ST_GEV-AIG_MRT	1.298821	-1.50105	4.098686	0.515722
	ST_GEV-PIC	0.046	-2.73413	2.826134	0.999151
Grape-Petiole		diff	lwr	upr	p adj
	PIC-AIG_MRT	-2.36917	-4.3508	-0.38753	0.014689*
	ST_GEV-AIG_MRT	-1.69267	-3.58747	0.202138	0.090038
	ST_GEV-PIC	0.6765	-1.06399	2.416989	0.627081
Grape-Steel		diff	lwr	upr	p adj
	PIC-AIG_MRT	12.93889	9.95831	15.91947	0*
	ST_GEV-AIG_MRT	9.375222	6.284892	12.46555	0*
	ST_GEV-PIC	-3.56367	-6.27091	-0.85642	0.006207*
Grape-Conveyor		diff	lwr	upr	p adj
	PIC-AIG_MRT	-2.77783	-6.56879	1.013132	0.195615
	ST_GEV-AIG_MRT	-0.77254	-4.6928	3.147714	0.886975
	ST_GEV-PIC	2.005288	-1.46962	5.480191	0.361099
Grape-Grape		diff	lwr	upr	p adj
	PIC-AIG_MRT				
	ST_GEV-AIG_MRT	0.550333	-2.51435	3.615018	0.722577
	ST_GEV-PIC				
Grape Stem-Grape		diff	lwr	upr	p adj
	PIC-AIG_MRT				
	ST_GEV-AIG_MRT	0.817	-2.20406	3.83806	0.593027
	ST_GEV-PIC				
Grape-Vine Shoot		diff	lwr	upr	p adj
	PIC-AIG_MRT				
	ST_GEV-AIG_MRT	0.2565	-1.27793	1.790929	0.740527
	ST_GEV-PIC				
Grape-Mesh		diff	lwr	upr	p adj
	PIC-AIG_MRT				
	ST_GEV-AIG_MRT	-0.85418	-2.48012	0.771758	0.299505
	ST_GEV-PIC				

Table C.31. Analysis of variance (Tukey HSD Test) results for the friction angle of biological materials (continued).

Friction Angle (◦)					
Grape-Bucket		diff	lwr	upr	p adj
	PIC-AIG_MRT				
	ST_GEV-AIG_MRT	4.172	0.984881	7.359119	0.010891*
	ST_GEV-PIC				
Grape Stem-Leaf		diff	lwr	upr	p adj
	PIC-AIG_MRT	3.318088	-0.03239	6.668565	0.052208
	ST_GEV-AIG_MRT				
	ST_GEV-PIC				
Leaf-Leaf		diff	lwr	upr	p adj
	PIC-AIG_MRT	1.229773	-3.19122	5.650762	0.581521
	ST_GEV-AIG_MRT				
	ST_GEV-PIC				
Petiole-Leaf		diff	lwr	upr	p adj
	PIC-AIG_MRT	4.356053	1.52388	7.188226	0.003028*
	ST_GEV-AIG_MRT				
	ST_GEV-PIC				
Grape Stem-Vine Shoot		diff	lwr	upr	p adj
	PIC-AIG_MRT	2.165	-0.27429	4.604289	0.081162
	ST_GEV-AIG_MRT				
	ST_GEV-PIC				
Grape Stem-Petiole		diff	lwr	upr	p adj
	PIC-AIG_MRT	-3.1441	-6.00327	-0.28492	0.031535*
	ST_GEV-AIG_MRT				
	ST_GEV-PIC				
Vine Shoot-Petiole		diff	lwr	upr	p adj
	PIC-AIG_MRT	-6.25	-9.08548	-3.41452	3.39E-05*
	ST_GEV-AIG_MRT				
	ST_GEV-PIC				
Petiole-Petiole		diff	lwr	upr	p adj
	PIC-AIG_MRT	-11.8065	-15.102	-8.51097	0*
	ST_GEV-AIG_MRT				
	ST_GEV-PIC				

Table C.32. Analysis of variance (Tukey HSD Test) results for the friction angle of biological materials (continued 2).

Friction Angle (◦)					
Grape Stem-Steel		diff	lwr	upr	p adj
	PIC-AIG_MRT	2.208933	-0.52058	4.938446	0.111444
	ST_GEV-AIG_MRT				
	ST_GEV-PIC				
Leaf-Steel		diff	lwr	upr	p adj
	PIC-AIG_MRT	1.65	-0.59065	3.890649	0.147042
	ST_GEV-AIG_MRT				
	ST_GEV-PIC				
Vine Shoot-Steel		diff	lwr	upr	p adj
	PIC-AIG_MRT	-4.05	-6.03466	-2.06534	0.000101*
	ST_GEV-AIG_MRT				
	ST_GEV-PIC				
Petiole-Steel		diff	lwr	upr	p adj
	PIC-AIG_MRT	8.45	6.678947	10.22105	0*
	ST_GEV-AIG_MRT				
	ST_GEV-PIC				
Grape Stem-Conveyor		diff	lwr	upr	p adj
	PIC-AIG_MRT	-4.26713	-6.98677	-1.54749	0.002413*
	ST_GEV-AIG_MRT				
	ST_GEV-PIC				
Leaf-Conveyor		diff	lwr	upr	p adj
	PIC-AIG_MRT	-1.28732	-4.79299	2.21836	0.467953
	ST_GEV-AIG_MRT				
	ST_GEV-PIC				
Vine Shoot-Conveyor		diff	lwr	upr	p adj
	PIC-AIG_MRT	-0.56111	-3.18355	2.061331	0.672196
	ST_GEV-AIG_MRT				
	ST_GEV-PIC				
Petiole-Conveyor		diff	lwr	upr	p adj
	PIC-AIG_MRT	-1.4805	-5.11677	2.155767	0.421511
	ST_GEV-AIG_MRT				
	ST_GEV-PIC				
Vine Shoot-Leaf		diff	lwr	upr	p adj
	PIC-AIG_MRT	-0.79667	-5.02128	3.427937	0.708636
	ST_GEV-AIG_MRT				
	ST_GEV-PIC				

C.2 Physical Characteristics of Artificial Grape

Table C.33. Physical characteristics of artificial grapes.

Artificial Grapes	Mean	St. Dev.	Coef. of Variation
Mass (g)	1.9	0.19	10.1%
Sphericity (%)	97.7	1.2	1.2%
Average Diameter (mm)	19.73	0.74	3.7%
True Density (kg WM/m^3)	467.9	26.6	5.7%

C.3 Multi-Deflection Tests for Complete Leaf

The following figures show the comparison between the scanned and simulated leaf for the five deflection configurations. Multiple views of the comparison are displayed for each configuration.

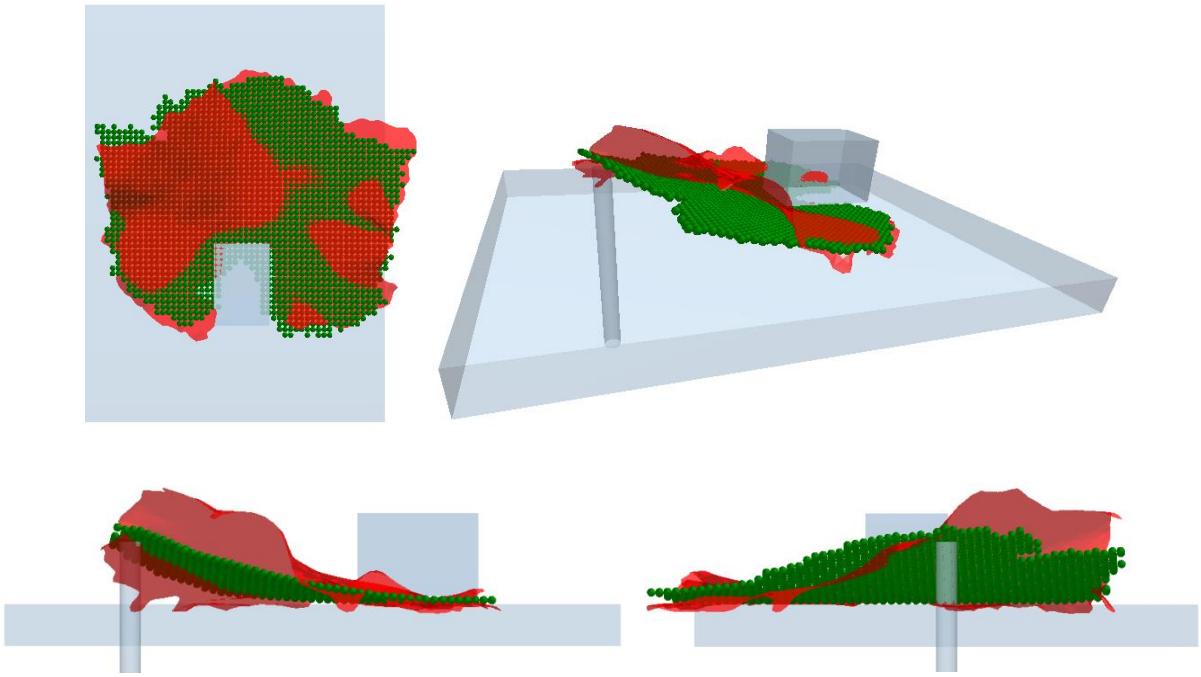

Figure C.1. Multi-deflection test comparison-Configuration 1. (a) Top view. (b) Orthogonal view. (c) Side view. (d) Front view.

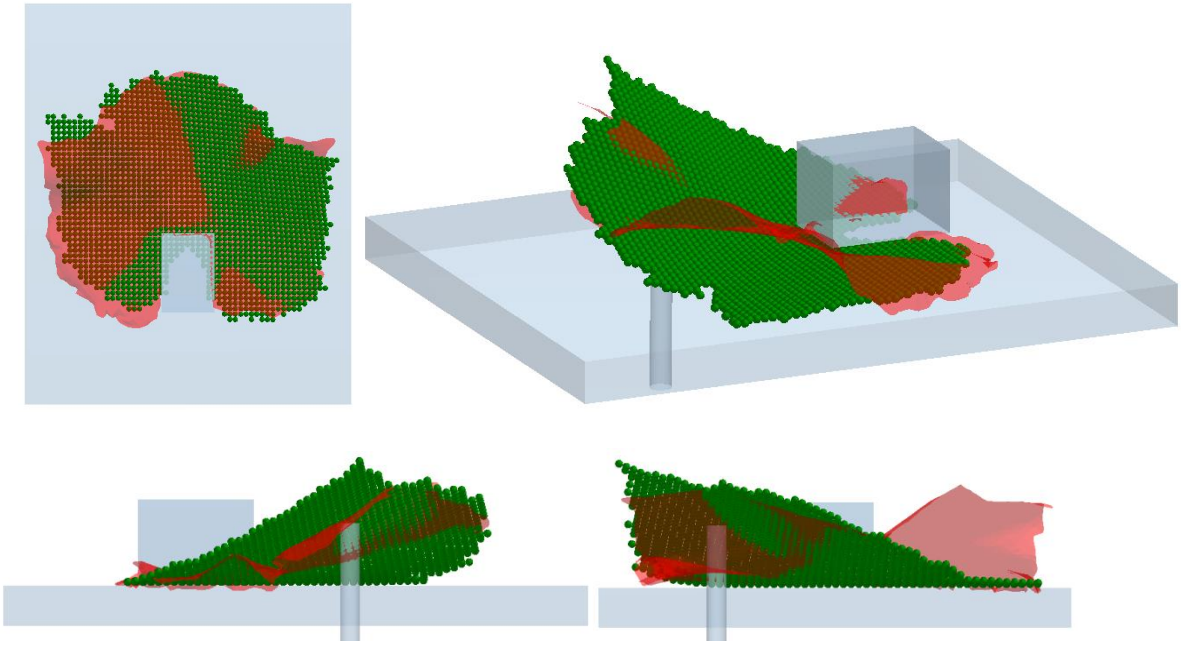

Figure C.2. Multi-deflection test comparison-Configuration 2. (a) Top view. (b) Orthogonal view. (c) Side view. (d) Front view.

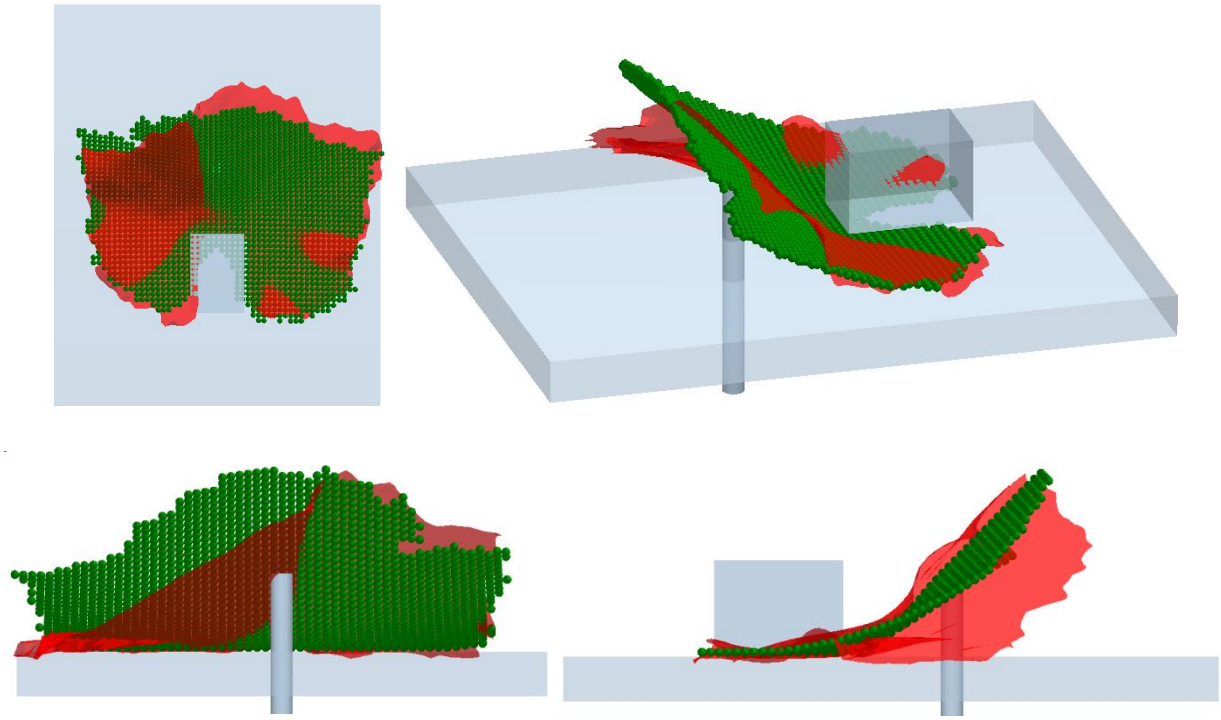

Figure C.3. Multi-deflection test comparison-Configuration 3. (a) Top view. (b) Orthogonal view. (c) Side view. (d) Front view.

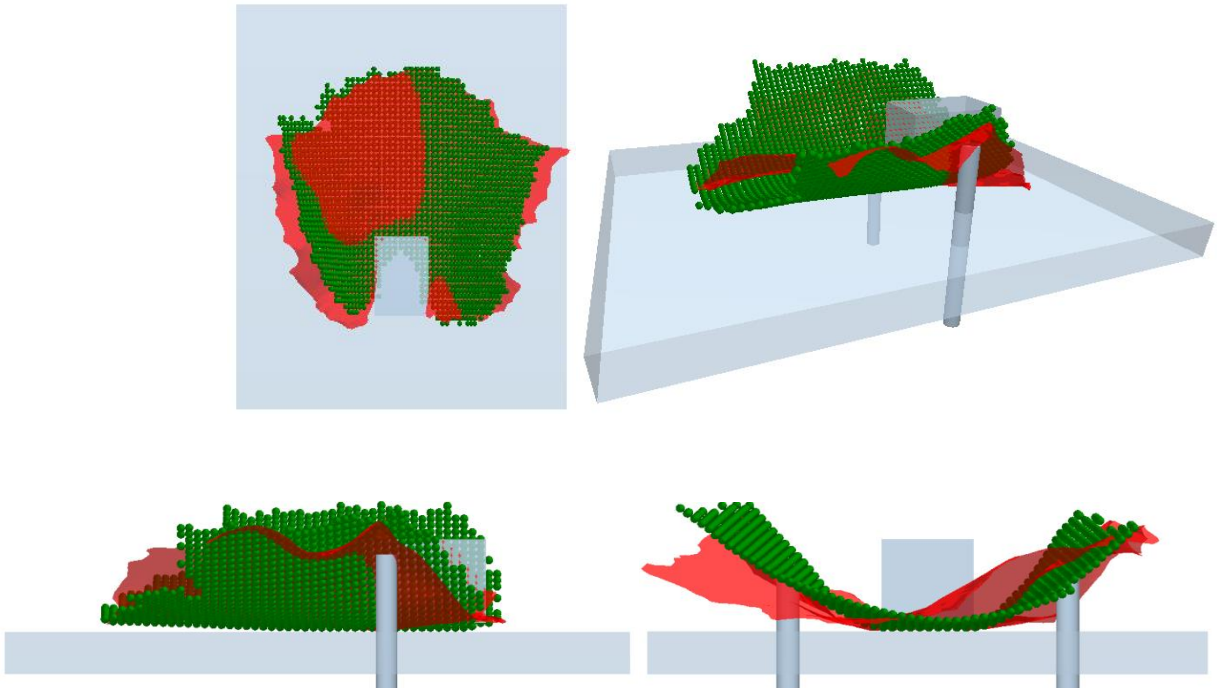

Figure C.4. Multi-deflection test comparison -Configuration 4. (a) Top view. (b) Orthogonal view. (c) Side view. (d) Front view.

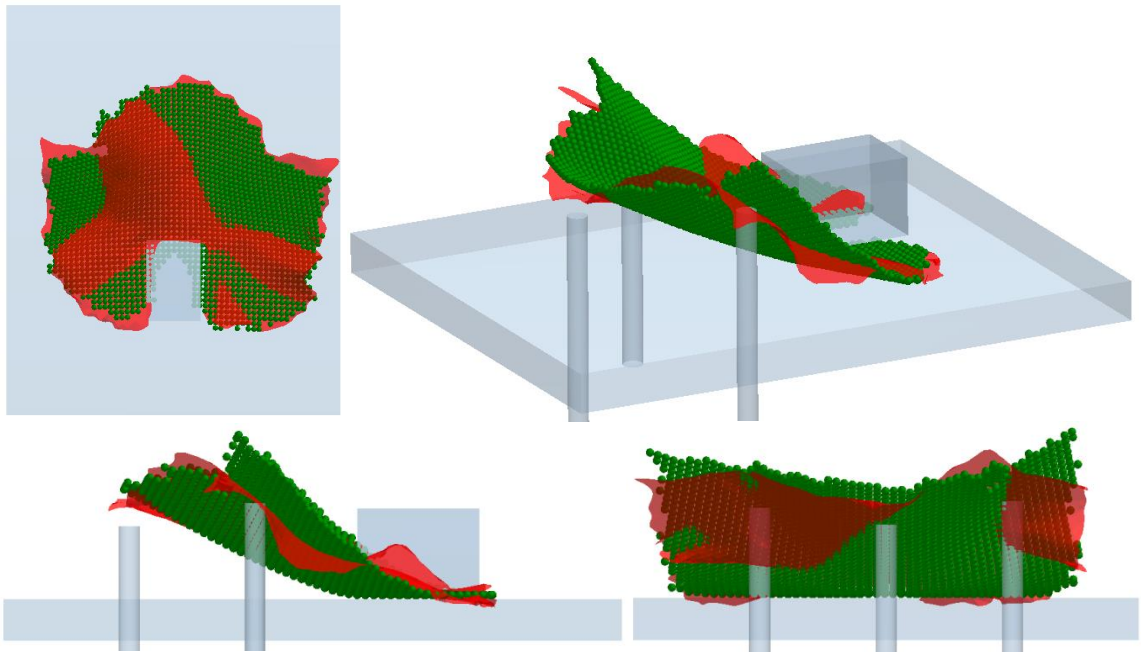

Figure C.5. Multi-deflection test comparison -Configuration 5. (a) Top view. (b) Orthogonal view. (c) Side view. (d) Front view.

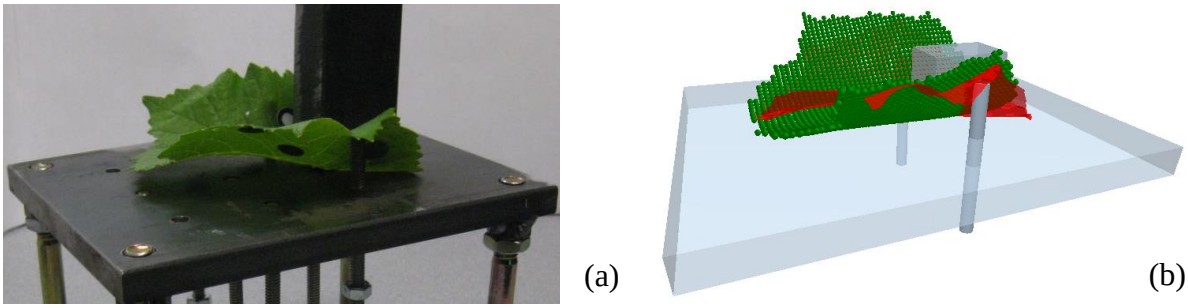

(a) (b)

Figure C.6. Leaf on multi-deflection plate-configuration 4. (a) Actual leaf that was scanned for the configuration 4. (b) Comparison between scanned (STL file) and simulated leaf.